Modeling Polarized Radiative Transfer for Improved Atmospheric Aerosol Retrieval with OSIRIS Limb Scattered Spectra

A Thesis
Submitted to the Faculty of Graduate Studies and Research
in Partial Fulfillment of the Requirements
for the Degree of
Master of Science
in the Department of Physics and Engineering Physics by

Anthony F. Bathgate
Saskatoon, Saskatchewan

December, 2010

In presenting this thesis in partial fulfillment of the requirements for a Postgraduate degree from the University of Saskatchewan, the author agrees that the Libraries of this University may make it freely available for inspection. The author further agrees that permission for copying of this thesis in any manner, in whole or in part, for scholarly purposes may be granted by the professor who supervised this thesis work or, in his absence, by the Head of the Department or the Dean of the College in which this thesis work was done. It is understood that any copying or publication or use of this thesis or parts thereof for financial gain shall not be allowed without written approval from the author. It is also understood that due recognition shall be given to the author and to the University of Saskatchewan in any scholarly use which may be made of any material in this thesis.

Requests for permission to copy or to make other use of material in this thesis in whole or in part should be addressed to:

Head of the Department of Physics and Engineering Physics
116 Science Place
University of Saskatchewan
Saskatoon, Saskatchewan
Canada
S7N 5E2

to my wife

Abstract

Retrievals of atmospheric information from satellite observations permit the investigation of otherwise inaccessible atmospheric phenomena. The recovery of this information from optical instrumentation located in orbit requires both an inversion algorithm like the Saskatchewan Multiplicative Algebraic Reconstruction Technique and a forward model like the SASKTRAN radiative transfer model. These are used together at the University of Saskatchewan to retrieve sulphate aerosol extinction profiles from the radiance measurements made by the Canadian built OSIRIS instrument. Although these retrievals are highly successful the process currently does not consider the polarization of light or OSIRIS's polarization sensitivities because SASKTRAN is a scalar model. In this work the development of a vector version of SASKTRAN that can perform polarized radiative transfer calculations is presented.

The vector SASKTRAN's results compare favorably with vector SCIATRAN, another polarized model that is in development at the University of Bremen. Comparisons of the stratospheric aerosol retrieval vectors generated from the scalar and vector SASKTRAN results indicate that the polarized calculations are an important factor in future work to improve the aerosol retrievals and to recover particle size or composition information.

Acknowledgements

I must express my thanks for the many opportunities I have had throughout the years to work as a member of the Institute of Space and Atmospheric Studies at the University of Saskatchewan. The funding and support I have received from both of these organizations made it possible for me to pursue my goals.

I wish to also thank Dr. Patricia Leibing of the Institute of Environmental Physics and the Institute of Remote Sensing at the University of Bremen. Her initiative to share results and compare the vector version of the SCIATRAN radiative transfer model with the vector version of SASKTRAN and other models in development was truly helpful to my work and greatly appreciated.

I would like to thank my fellow members of the Institute; the help, advice and opinions offered by Chris Roth, Truitt Wiensz, and Paul Loewen were invaluable to me over the years. My thanks also go out to Drs. Ted Llewellyn, Adam Bourassa, and Nick Lloyd. Many times I relied upon their advice to point me to a solution. It was their enthusiasm that impressed upon me the importance of atmospheric research and inspired my interests many years ago. I would also like to express my heartfelt thanks to my supervisor Dr. Doug Degenstein whose guidance, encouragement, and generosity not only made my work here possible but also a pleasure. He allowed me both the guidance and the freedom I needed to accomplish my goals and his commitment to his students is a genuine testament to his amazing character.

To my family, especially my wonderful wife Yang: thank you for your unending support and encouragement.

Contents

List of Figures

List of Tables

List of Abbreviations

DLL Dynamically-Linked Library

DSP Diffuse Scattering Points

ECI Earth Centered Inertial

ECMWF European Centre for Medium-Range Weather Forecasts

HALOE Halogen Occultation Experiment

IRI InfraRed Imager

LOS Line of Sight

MJD Modified Julian Date

MSIS Mass Spectrometer Incoherent Scatter model

OLOS Observer Line of Sight

OO Object Oriented

OS Optical Spectrograph

OSIRIS Optical Spectrograph Infra-Red Imaging System

PI Picard Iteration

POAM Polar Ozone and Aerosol Measurement

RTM Radiative Transfer Model

SAA Solar Azimuth Angle

SAGE Stratospheric Aerosol and Gas Experiment

SAM Stratospheric Aerosol Measurement

SaskMART Saskatchewan Multiplicative Algebraic Reconstruction Technique developed at the University of Saskatchewan

SSA Stratospheric Sulphate Aerosol

SZA Solar Zenith Angle

UTLS Upper Troposphere - Lower Stratosphere

vmr volume mixing ratio

Chapter 1

Introduction

The details of many atmospheric events and processes elude study due the difficulty involved in their measurement. Satellite based remote sensing is a powerful technique for atmospheric science, especially in cases where continuous in situ observation is impractical. Satellites can also offer global coverage and their potentially long mission lives can provide data sets over many years; for example the OSIRIS instrument discussed in Section 1.2 has been collecting data from 2001 to present (*Llewellyn et al.*, 2004).

Often the information of interest may not be directly observable by satellite and the recovery of the information of interest from satellite observations can pose many difficulties. The directly observable data collected by satellites are used to reconstruct the state or value of interest in the atmosphere through a process called retrieval. This process requires the use of what is known as a forward model, which predicts the observable data based on a given value or state of interest.

SASKTRAN is a fully spherical computerized Radiative Transfer Model (RTM) developed at the University of Saskatchewan. It has been highly successful serving as a forward model for atmospheric measurement. Previous versions of SASKTRAN are scalar; therefore current retrieval processes omit polarized information and the known polarization responses in optical measurement devices. Having a fully polarized RTM is a vital step to improving the accuracy of SASKTRAN's results and therefore improving retrievals of atmospheric data. The goal of this thesis work is to produce a version of SASKTRAN that is capable of performing polarized radiative transfer calculations.

This chapter provides an introduction to topics that are relevant to this thesis work. The first section describes aerosols and their origins. It goes on to cover why

their study is important to the atmospheric science community and recount previous efforts to measure them. Following that is a description of the OSIRIS instrument and the known sensitivities to polarization it possesses. +Retrievals are described in greater detail in the subsequent section, specifically the algorithm used with SASKTRAN and OSIRIS data is explained. These topics are not the subject of this thesis work but are included to give context to this work and illustrate its motivation. The final section of this chapter provides a summarized outline for the remainder of this document.

1.1 Aerosols

Aerosols are liquid, solid, or mixed phase particles suspended in the atmosphere and their size and composition varies greatly. Anything from volcanic ash to suspended ice crystals qualify as aerosols and therefore there is a complex and diverse range of effects that aerosols may have on the atmosphere. For example due to water's supersaturation point at standard atmospheric temperatures and pressures the presence of solid phase aerosol is often necessary for condensation of water vapour; this affects humidity levels and creates water droplets, a different type of aerosol (*Twomey*, 1977). Aerosols of all types affect chemical processes in the atmosphere and can be used as tracers for air movement (*Fleagle and Businger*, 1980). Also, through light scattering aerosols play a significant role in the radiative balance of the Earth, an increasingly emphasized area of research.

One very common type of aerosol is the suspended ice crystal, which can be found at high altitudes. When they are in a high enough concentration they form cirrus clouds, which are high altitude clouds that are typically found near the tropopause. These clouds have a tenuous appearance if visible and often are too thin to be observed by the naked eye. Sulphate aerosols are also found at high altitudes all over the globe. They consist of hydrated sulphuric acid and are found in high concentrations in what is known as the Junge layer. The Junge layer is found within the stratosphere, typically around 25 km in altitude.

Both of these aerosols can be produced by natural mechanisms but they are also the result of anthropogenic sources. Because of their link to human activity and their wide range of effects on the atmosphere there is ample motivation for further study. Long term globally distributed measurements of aerosols with high vertical resolution would allow for their analysis.

In the following subsections information about common aerosols and their effects on the atmosphere are discussed. Although certain details are used to model the optical properties of aerosols, the microphysics of aerosols and their links to atmospheric physics are not the subject of this thesis. This information is included to illustrate the motivation for the development of an accurate polarized RTM.

1.1.1 Origins of Important Atmospheric Aerosols

There are a variety of ways that aerosols are produced naturally including the lifting of particulate matter from the ocean surface or dusty terrain by turbulent wind, the deposition of large quantities of extraterrestrial material in the highest regions of the atmosphere, and the formation of drops or particles directly from gas phase (*Twomey*, 1977). Aerosol production due to volcanic activity and forest fires is also common and can cause large disturbances in the regular background distributions.

Based on natural emission rates for some common sources of certain aerosols and much higher emission rates related to industrial activity it is clear that anthropogenic sources have been significant for well over a century (*Vestreng et al.*, 2007). This anthropogenic contribution may be causing substantial changes to the atmosphere (*Hofmann et al.*, 2009). One well documented example is the influence of background sulphate aerosols on the accelerated springtime depletion of ozone in polar regions (*Solomon*, 1999).

Sulphur dioxide is emitted or produced in the atmosphere by many natural processes like volcanic emission and biological decay (*Granat et al.*, 1976). Many industrial processes, including combustion, some smelting processes, and petroleum refining, release large amounts of sulphur dioxide that greatly outweigh natural production (*Vestreng et al.*, 2007). Once in the stratosphere the sulphur dioxide oxidizes and then reacts further with water vapour to produce the hydrated droplets of sulphuric acid that make up Stratospheric Sulphate Aerosol (SSA).

Although the background Junge layer is always present in the stratosphere the majority of sulphur released into the atmosphere does not leave the troposphere and has a short lifetime (*Granat et al.*, 1976). Strong convective forces, often created by forest fires and rising hot air near the equator, may inject aerosols or their source gasses into the stratosphere. Volcanic eruptions also commonly inject sulphate aerosols into the stratosphere. In extreme cases they have been observed to persist in the stratosphere for years (*Symons*, 1888).

Another aerosol present in the Upper Troposphere - Lower Stratosphere (UTLS) that is of concern are ice particles that make up cirrus clouds. These clouds form when moist parcels of air are lifted to high altitudes where they cool and water vapour freezes. The uplifting that creates these clouds may be caused by deep convective cells, synoptic scale weather systems, or waves induced by terrain. Temperature and humidity conditions that allow the condensation of pure water droplets (homogeneous nucleation) are more extreme than those for condensation of water droplets on some pre-existing particle (non-homogeneous nucleation). So other forms of aerosols are usually present to serve as nuclei where ice crystallization takes place (*Twomey*, 1977). Cirrus clouds are limited to the tropopause and below because of the increasing temperatures in the stratosphere.

Because other aerosols are important for the formation of cirrus clouds they are also influenced by human activity. For example high altitude aircrafts leave behind exhaust which serves as nuclei for condensation and crystallization. *Sassen* (1997) demonstrates that these anthropogenic cirrus clouds have non-negligible effects on the Earth's radiation budget.

The conditions under which the cirrus clouds form strongly affect the characteristics of its ice crystals. The amount of available condensation nuclei and water vapour, as well as the rate an air parcel is cooled dictate the characteristic size of the crystals (*Twomey*, 1977). The cooling rate of a parcel is dominated by its upward speed, which in turn is dictated by the cause of the uplifting. For instance parcels lifted by deep convection in tropical storms can rise at speeds of metres per second (*Jensen et al.*, 1994) while parcels lifted by advancing fronts at mid-latitudes rise at centimetres per second (*Starr and Cox*, 1985).

In general the size of an aerosol particle is dictated by a number of factors. Particles are grown by the condensation of surrounding vapours and through coagulation with other particles. Under some conditions they may shrink due to evaporation or they may be directly removed from the atmosphere due to precipitation or sedimentation. To further complicate matters the rates at which these effects act are dependent on particle size. It is the balance of all these factors that leads to the steady state size distribution and number densities present in the atmosphere (*Twomey*, 1977). Studies by *Bingen et al.* (2004) and *Bauman et al.* (2003) show that when the stratosphere is in its steady state a single mode log-normal distribution appropriately fits the size distribution.

Significant amounts of SSA are generated through anthropogenic sources and the entire globe is potentially affected by the Junge layer that SSA form. Extensive work has been done to perform retrievals from OSIRIS limb scattered spectra observations using SASKTRAN to obtain SSA information as discussed by *Bourassa* (2007). Because they are an important area of study and because of SASKTRAN's role in their measurement further discussion of aerosols in this work will relate to SSA.

1.1.2 Effects of Stratospheric Sulphate Aerosols

Sulphate aerosols change the radiative balance of the Earth. Aerosols may increase the atmosphere's ability to reflect solar radiation; this would shield the Earth and create a cooling effect. At the same time they may increase the amount of infrared radiation reflected back to Earth, acting like a blanket and making the surface of the Earth warmer. Both of these effects are very much dependent upon the distribution of the particle size. Evidence shows that the net effect of SSA is to cool the Earth (*Lacis et al.*, 1992). The magnitude of this cooling is still open to debate, especially during periods of active volcanism.

Aerosols also serve as condensation and ice formation nuclei. Because of this they affect the amount of cloud coverage as well as the clouds' droplet size and composition, which changes their scattering efficiency. Clouds are effective at reflecting solar radiation back to space and infrared radiation back to Earth. So aerosols have indirect effects on the radiative balance of the Earth as well by influencing cloud formation (*Lohmann and Feichter*, 2005).

The link between cloud formation and aerosols also has an important impact upon atmospheric chemistry. SSA contributes to the formation of polar stratospheric clouds, which play a critical role in the chemistry of springtime ozone destruction. It has been shown that even the background level of sulphate aerosols influences the extent of ozone destruction at midlatitudes (*Solomon*, 1999).

These effects and the significant anthropogenic contribution to sulphate aerosols necessitates the study of SSA. Accurate and effective measurement of SSA levels will allow us to monitor anthropogenic sources and help to estimate the impact they have on the environment. Such a measurement set exists as SSA have been retrieved from OSIRIS measurements that date back to 2001. The RTM developed as part of this thesis work will help to better interpret the OSIRIS measurements providing more accurate aerosol distributions.

1.1.3 Measurements of Stratospheric Sulphate Aerosols

Measurements of SSA have been taken for decades, both directly using balloon mounted instruments and remotely from lidar and satellite measurements. Previous measurement sets have been severely limited in location, vertical resolution, or both.

The colours present in the twilight sky led *Gruner and Kleinert* (1927) to suggest a persistent layer of aerosols exists in the stratosphere. The first direct evidence for this layer was recorded by *Junge et al.* (1961) who took in situ measurements using high altitude balloons. The device he used measured two particle size ranges, the first being 0.01μm to 0.1μm in radius and the second being 0.1μm to 1.0μm. He found that while the number of smaller particles decreased with altitude to an undetectable amount by 20 km the larger particles showed a peak at 20 km. Further measurements have demonstrated that this distribution of larger particles around 20 km is persistent and not localized to any given region. This ubiquitous background distribution of aerosols is often called the Junge layer. *Rosen* (1971) has shown by further in situ measurements that stratospheric aerosols from this region are largely composed of hydrated sulphuric acid. Because SSA are typically liquid droplets on the order of a micron surface tension would be the dominant force determining their shape so they are generally treated as spherical particles.

Balloon based measurements like those run by *Deshler et al.* (2003) have collected more than thirty years of stratospheric aerosol data for individual sites that allow analysis of long term trends of both number density and size distribution parameters. The measurement also allow for very high vertical resolution. Unfortunately each balloon launch is a very involved endeavor and by their nature the measurements are limited to the launch location.

Many measurements of aerosol extinction values have been taken using satellite based solar occultation instruments such as the Stratospheric Aerosol Measurement (SAM) II, the Stratospheric Aerosol and Gas Experiment (SAGE) I II and III (*McCormick et al.*, 1979; *Russell and McCormick*, 1989; *Thomason and Taha*, 2003), the Halogen Occultation Experiment (HALOE) (*Russell et al.*, 1993), and the Polar Ozone and Aerosol Measurement (POAM) II and III (*Glaccum et al.*, 1996; *Lucke et al.*, 1999). Together these instruments have recorded information about stratospheric aerosol densities and size distributions from 1978 to 2005. Currently the Atmospheric Chemistry Experiment (ACE), using the Measurements of Aerosol Extinction in the Stratosphere and Troposphere Retrieved by Occultation (MAESTRO) (*Sioris et al.*, 2010) and the

ACE imagers (*Vanhellemont et al.*, 2008), perform solar occultations and are capable of measuring aerosol parameters.

Satellite based solar occultation works by viewing the sun through the atmosphere as the instrument experiences local sunrises and sunsets along its orbit. Generally the instrument's line of sight is fixed on the sun and as it moves this line of sight passes through a range of altitudes tangent to the Earth's curvature. During this time it records measurements of optical or infrared wavelengths. Regular measurements above the atmosphere are also recorded and used for comparison and calibration. Occultation data is used to calculate the aerosol extinction values, number densities, and size distributions. This solar occultation technique inherently limits the instrument to measuring only two profiles each orbit and the orbit geometry also limits the locations of the measurements to a relatively small latitude band over a given day or week.

Globally distributed measurements of stratospheric aerosol would be far more useful. Global coverage would allow us to track transport processes and study global fluctuations. Measurements of stratospheric aerosol with a high vertical resolution and global coverage may be retrieved from spectrographic data recorded by the OSIRIS instrument (which is described in detail in Section 1.2) when coupled with an effective RTM like SASKTRAN (described in Section 2.2.1).

1.2 OSIRIS

The Optical Spectrograph and InfraRed Imaging System (OSIRIS) is a Canadian device on board the Swedish spacecraft Odin launched in February of 2001. Odin has a circular, sun-synchronous orbit, inclined 98° from the equator, at an altitude near 600 km, with a 96 minute period. Because of this OSIRIS stays very near local dusk on the ascending track and near local dawn on the descending track, going through local midnight near the southern pole and local noon near the northern pole (*Llewellyn et al.*, 2004). OSIRIS is a limb-viewing device, which means that its lines of sight project from the instrument through the atmosphere without intersecting the Earth's surface to measure scattered light. This is in contrast with nadir-viewing devices whose line of sight is fixed towards the Earth's surface, or occultation devices whose line of sight is fixed on the sun or stars.

The Optical Spectrograph (OS) has a field of view that spans approximately 40 km horizontally and 1 km vertically. It makes repeated measurements approximately every

2 km while scanning up and down between tangent altitudes of about 10 km to 100 km. The scan period is around 1.5 minutes which allows nearly 60 scans every orbit. Because of the orbit geometry and because the OS's field of view points along the orbit path the OS only sees the summer hemisphere illuminated by the sun, except during the equinoxes when the entire orbit is illuminated (*Bourassa*, 2007).

The OS measures 280 nm to 810 nm with a 1353 pixel-wide CCD, with a spectral resolution of approximately 1 nm. Data from the wavelength range of 475 to 535 nm is discarded due to contamination from the spectrograph's order sorter. The InfraRed Imager (IRI) consists of three channels that record the limb radiance at 1260, 1270, and 1530 nm. Each consists of an array of 100 photodetectors with a tangent altitude resolution of about 1 km. Therefore the IRI simultaneously measures 100 vertical kilometers in tangent altitude. The IRI and its measurements will not be discussed further in this work.

As first observed by *Wood* (1902) all diffraction gratings experience spectral anomalies resulting from complex interactions between the diffracted and incident electromagnetic waves at the surface of the grating. These interactions are strongly affected by the polarization of the incident radiation. Although vector diffraction theory is required to accurately predict the effects of these Wood's anomalies, the existence of a relation to polarization can be understood qualitatively if we imagine linearly polarized light reflecting from the surface of the grating. Light that has a polarization parallel to the grooves will react differently than if its polarization is perpendicular to the grooves. These different reactions vary how well light is reflected or absorbed by the grating. For a detailed explanation of the polarization of light please refer to Section 2.3.

The polarization sensitivities of the OS have been well documented by *McLinden et al.* (2002). They were characterized experimentally using randomly polarized light sources which were passed through linear polarizers before reaching the OS. A coordinate system is defined whose axes are parallel and perpendicular to the grating grooves as depicted in Figure 1.1. We also define an angle α that is measured between this perpendicular axis and the direction of linear polarization.

Stokes Vectors are four element column matrices, $\underline{I} = \begin{bmatrix} I & Q & U & V \end{bmatrix}^T$, that describe the intensity and polarization state of light as explained in detail in Section 2.3.1. The incident Stokes Vector $\underline{I}$ will be related to the diffracted Stokes vector, $\underline{I}_{dif}$, by the equation

$$\underline{I}_{dif} \propto \mathbf{GX}\underline{I}. \tag{1.1}$$

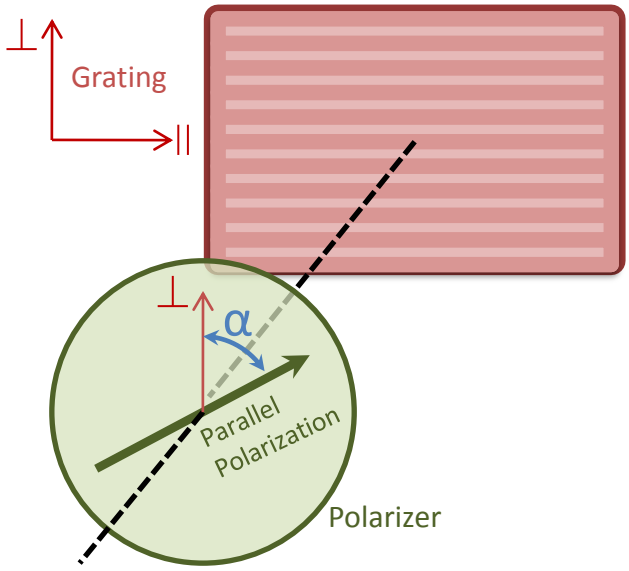

Figure 1.1: Schematic representation of the parallel polarization direction of the linear polarizer, measured with respect to the orientation of the OS diffraction grating. Adapted from *McLinden et al.* (2002).

The linear transformation introduced by the grating is the product of an unknown 4x4 matrix and a flat field response function, $f(\lambda)$. This may be written as

$$\underline{\mathbf{G}} = f(\lambda) \begin{bmatrix} 1 & g_{12}(\lambda) & g_{13}(\lambda) & g_{14}(\lambda) \\ g_{21}(\lambda) & g_{22}(\lambda) & g_{23}(\lambda) & g_{24}(\lambda) \\ g_{31}(\lambda) & g_{32}(\lambda) & g_{33}(\lambda) & g_{34}(\lambda) \\ g_{41}(\lambda) & g_{42}(\lambda) & g_{43}(\lambda) & g_{44}(\lambda) \end{bmatrix}. \tag{1.2}$$

The factor $f(\lambda)$ corresponds to the effect of the grating on the radiance of randomly polarized light.

The linear polarizer's transformation matrix is represented by the known 4x4 matrix,

$$\underline{\mathbf{X}} = \begin{bmatrix} 1 & \cos(2\alpha) & \sin(2\alpha) & 0 \\ \cos(2\alpha) & \cos^2(2\alpha) & \cos(2\alpha)\sin(2\alpha) & 0 \\ \sin(2\alpha) & \cos(2\alpha)\sin(2\alpha) & \sin(2\alpha) & 0 \\ 0 & 0 & 0 & 0 \end{bmatrix}. \tag{1.3}$$

Since the OS only directly measures the diffracted radiance McLinden et al. retains only the first row of $\underline{\mathbf{G}}$. They likewise omit the fourth element of $\underline{I}_{dif}$ and the fourth

column and row of $\underline{\mathbf{X}}$ since they only deal with circular polarization, which is negligible in the atmosphere. For a normalized, randomly polarized, inbound Stokes vector Equation 1.1 can be re-written as

$$\begin{aligned} I_{diff} &= f(\lambda) \begin{bmatrix} 1 \\ g_{12}(\lambda) \\ g_{13}(\lambda) \end{bmatrix}^T \begin{bmatrix} 1 & \cos(2\alpha) & \sin(2\alpha) \\ \cos(2\alpha) & \cos^2(2\alpha) & \cos(2\alpha)\sin(2\alpha) \\ \sin(2\alpha) & \cos(2\alpha)\sin(2\alpha) & \sin(2\alpha) \end{bmatrix} \begin{bmatrix} 1 \\ 0 \\ 0 \end{bmatrix} . \\ &\propto 1 + g_{12}(\lambda)\cos(2\alpha) + g_{13}\sin(2\alpha) \end{aligned} \tag{1.4}$$

During OSIRIS calibration a polarizer was rotated at 15° intervals from $\alpha = 0°$ to $\alpha = 180°$ and the response for each CCD pixel was measured. The response for two pixels is shown in Figure 1.2. The linear regression fits shown for pixels #357 and #1100 were $0.1 - 0.099\cos(2\alpha) - 0.002\sin(2\alpha)$ and $0.1 + 0.021\cos(2\alpha) - 0.011\sin(2\alpha)$ respectively. The factors g_{12} and g_{13} have all been obtained from the linear regression fits for each pixel's response and are provided by McLinden et al.

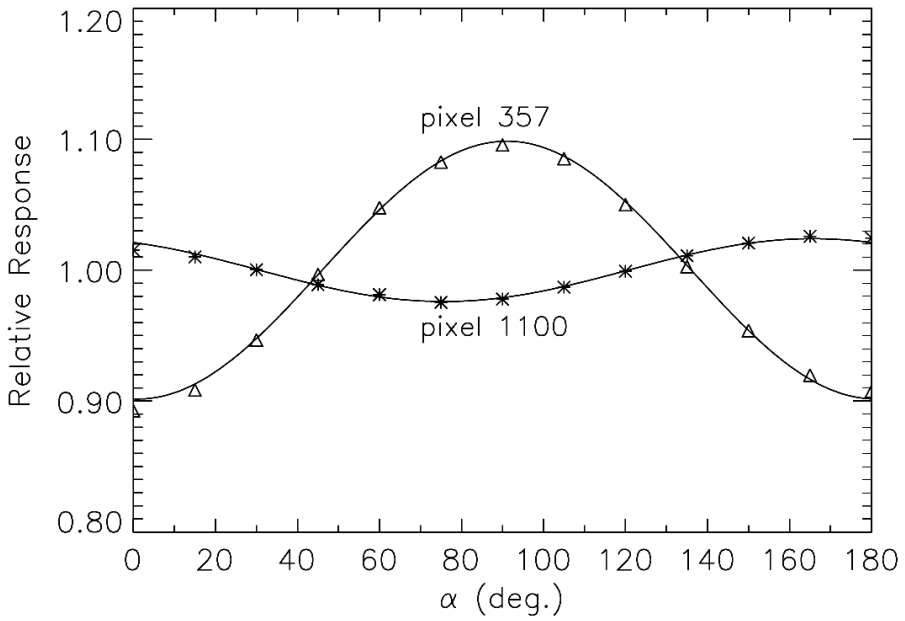

Figure 1.2: Variation of relative grating response for pixels #357 and #1100. Laboratory data are shown as symbols along with linear regression to fit the data. Image from *McLinden et al.* (2002).

The schematic in Figure 1.3 shows a second set of axes that McLinden et al. defined to be parallel and perpendicular to a reference plane. This reference plane would be

defined to contain OSIRIS's position vector and line of sight. This convention is what would be employed while considering real measurements with respect to the orientation of the Earth, sun, and OSIRIS. Transforming to this coordinate system is equivalent to a 90° rotation which, as described in Section 2.3.4, is represented by the matrix

$$\underline{\mathbf{R}}(90^\circ) = \begin{bmatrix} 1 & 0 & 0 & 0 \\ 0 & -1 & 0 & 0 \\ 0 & 0 & -1 & 0 \\ 0 & 0 & 0 & 1 \end{bmatrix}. \tag{1.5}$$

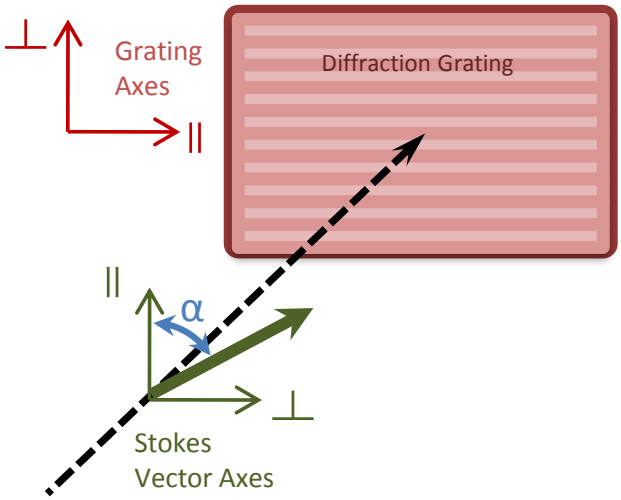

Figure 1.3: Schematic representation of the parallel polarization direction of the linear polarizer, measured with respect to the orientation of the OS diffraction grating. Adapted from *McLinden et al.* (2002).

Therefore radiance observed by OSIRIS for any incident Stokes Vector may be written as

$$\begin{aligned} I_{diff} &= f(\lambda) \begin{bmatrix} 1 & g_{12}(\lambda) & g_{13}(\lambda) \end{bmatrix} \underline{\mathbf{R}}(90^\circ)\underline{I} \\ &= f(\lambda)\left[I - g_{12}(\lambda)Q - g_{13}(\lambda)U\right] \end{aligned}. \tag{1.6}$$

These factors g_{12} and g_{13} are shown in Figure 1.4.

All optical spectrographs will experience anomalies produced by polarized light and with OSIRIS these anomalies have been characterized. RTMs are used to predict what is observed by instruments like OSIRIS and these observations and predictions are used in tandem to retrieve information about the atmosphere. Because Wood's anomalies

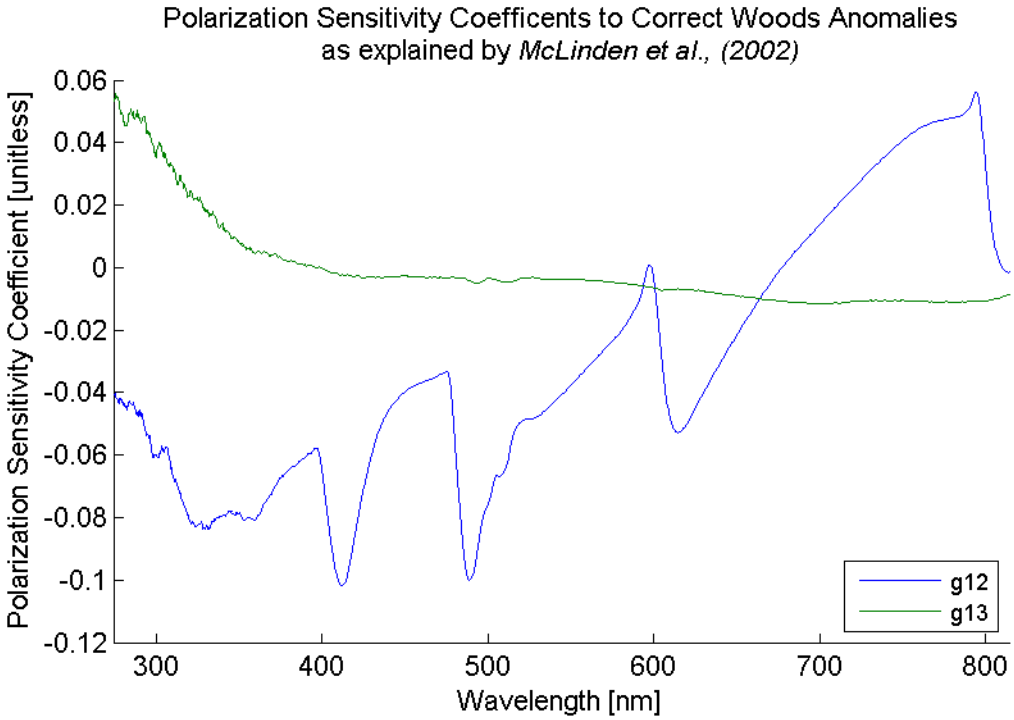

Figure 1.4: The OSIRIS grating parameters g_{12} and g_{13} as measured by *McLinden et al.* (2002)

are present in the observations a polarized RTM is required to improve retrievals of atmospheric information.

1.3 Retrievals

Theories and laws are constructed such that if we know the state of a system we will be able to predict some observable quantity. This formulation may be called a forward model. Often we have measured quantities produced by the system and must use this information to deduce the state of the system. This is called the inverse problem and it inevitably arises in many branches of experimental science where perfect knowledge of the state is unattainable.

If the system under scrutiny is linear, then it usually possible to directly invert the forward model and use the measurements to find the state of the system. In cases where the system is nonlinear and where the measurements are discrete in space and time, such as the effects of aerosol densities upon scattered sunlight measurements, the forward model will not be invertible. In cases like this numerical methods must be used to retrieve an approximate solution from the measurements and the forward model.

Some details about retrievals and the specific retrieval method used in conjunction with the SASKTRAN RTM are provided below. This information provides context and sheds light on the motivation behind RTM development. However the retrieval process itself is not developed in this thesis.

1.3.1 SaskMART

The Saskatchewan Multiplicative Algebraic Reconstruction Technique (SaskMART) is an iterative method for solving the inverse problem that was first developed to deblur Fabry-Perot images by *Lloyd and Llewellyn* (1989). It has previously been used as a retrieval technique by *Degenstein et al.* (2003) and *Bourassa et al.* (2007). It is similar to other inversion techniques, like those developed by *Chahine* (1970) and *Twomey* (1975), but provides advantages over them as well. SaskMART has the important ability to incorporate multiple independent observations of the same location into the inversion process and may result in reduced computation times.

If we have a column matrix of independent measurements called the retrieval vector, $\underline{\mathbf{y}}$, and a column matrix of unknown state parameters, $\underline{\mathbf{x}}$, then they are related by,

$$\underline{\mathbf{y}} = \underline{\mathbf{F}}(\underline{\mathbf{x}}, b) + \epsilon \tag{1.7}$$

where $\underline{\mathbf{F}}$ is the forward model and is composed of physical laws and theory, b is other information about the atmosphere that we know or are inferring, and ϵ is the associated measurement error.

For a one dimensional set of state parameters, like a vertical profile of the atmosphere, SaskMART gives the $(n+1)^{th}$ iteration for the the i^{th} parameter by the equation,

$$x_i^{(n+1)} = x_i^{(n)} \sum_j \frac{y_j}{F_j(\underline{\mathbf{x}}^{(n)}, b)} W_{ij} \tag{1.8}$$

where the elements W_{ij} make up a weighting matrix that defines the influence of the j^{th} state parameter on the i^{th} measurement.

The RTM SASKTRAN, described in detail in Section 2.2, serves as a forward model to simulate the light that would be observed by OSIRIS, which is used to construct a retrieval vector. The state parameter of interest is the SSA profile in the atmosphere. Previous retrievals performed by *Bourassa et al.* (2007) used a weighting matrix based on the intersections of the observer's line of sight through the atmospheric cells nearest the tangent altitude.

1.3.2 The Retrieval Vector

The retrievals of stratospheric sulphate aerosols, presented by *Bourassa et al.* (2007), employ a retrieval vector based on the radiance observed at a short wavelength, $\lambda_s = 470\,\text{nm}$, and a long wavelength, $\lambda_l = 750\,\text{nm}$, from an OSIRIS scan. These are normalized to the measurement at a reference tangent, $h_r = 40\,\text{km}$, to reduce the influence of ground scatter. The ratio of these normalized radiances was used to eliminate influence from fluctuations in the neutral atmospheric density and natural logarithm is taken to make a more manageable vector due to the exponential nature of the height profile. The j^{th} element of the vector corresponds to the j^{th} observation from a scan and may be written as,

$$y_j = \log\left(\frac{I(h_j,\lambda_l)/I(h_r,\lambda_l)}{I(h_j,\lambda_s)/I(h_r,\lambda_s)}\right) - \log\left(\frac{I_o(h_j,\lambda_l)/I_o(h_r,\lambda_l)}{I_o(h_j,\lambda_s)/I_o(h_r,\lambda_s)}\right) \tag{1.9}$$

where $I(h_j,\lambda)$ is the observed radiance along the line of sight that is tangent to the curvature of the Earth at height h_j for wavelength λ. The variable I_o is produced by the forward model using an aerosol free atmosphere for the simulation. This aerosol free radiance is also used to minimize the influence of other atmospheric variables on the vector.

These two wavelengths were chosen to get the largest separation possible within the OSIRIS spectra while avoiding interfering features in the spectra. The longer wavelength provides sensitivity to aerosol scattering, which is still in effect at long wavelengths. Shorter wavelengths are more sensitive to molecular and atomic scattering so $I(h_j,\lambda_s)/I(h_r,\lambda_s)$ is used to normalize the vector to reduce the influence of non-aerosol scatterers. Because the optical depth of the atmosphere increases too much for short wavelengths at lower altitudes λ_s could not be shorter than 470 nm. Because of the O_2 absorption band at 762 nm and the strong sensitivities to polarization described in Section 1.2 at the long end of the OS spectra λ_l could not be moved to a wavelength longer than 750 nm.

With a polarized version of SASKTRAN and using the polarization sensitivity relation, Equation 1.6, it should be possible to perform more accurate retrievals of aerosol densities. A vector SASKTRAN will produce more accurate radiance values to be used in the retrieval vector. Also with an accurate model of the long end of the simulated OS spectra it would be possible to move λ_l to longer wavelengths since it will no longer be necessary to avoid the strong OS polarization sensitivity at long wavelengths. This will increasing the retrieval's sensitivity. Although it is not the

topic of this thesis, it should also be possible to use a vector version of SASKTRAN to take advantage of the polarization response to construct a retrieval vector that could differentiate between suspended ice crystals and SSA in the atmosphere.

1.4 Outline

The continued and expanded study of atmospheric species including aerosols like SSA and cirrus clouds is of great importance to the scientific community. The ability to evaluate global trends over long time frames is necessary to estimate the impact of human activity on the world and generate some remedy. OSIRIS has collected globally distributed spectrographic measurements dating back to 2001 that when coupled with the scalar SASKTRAN RTM in the SaskMART retrieval technique produces information about several atmospheric species of interest. To improve these retrievals it is necessary to have a RTM that accurately simulates polarized light in the atmosphere. Creating a vector version of SASKTRAN to fulfil this need is the subject of this work.

The background information required to complete this work makes up Chapter 2. It will include the derivation of radiative transfer equations and a functional description of the scalar version of SASKTRAN and some of its components. The representation of the polarization state of light is derived and explained as well as the mathematical operations that describe light scattering processes. The radiative transfer equations are defined for polarized scattering. Finally the design goals for this work and the specific changes are presented to produce a vector SASKTRAN capable of performing polarized radiative transfer calculations.

Chapter 3 covers the details of the implementation of the vector SASKTRAN model. This describes how the SASKTRAN components were altered or replaced in order to calculate polarized radiative transfer and meet the model's design goals. This chapter also includes a description of several interpolation methods for polarized source terms and a study of their effectiveness. This study highlighted a problem that may result from interpolating between different reference frames used to describe the polarization state of the source term. A solution to this issue and a demonstration of its effectiveness are also presented.

To validate the vector SASKTRAN model it was compared to the polarized SCIATRAN model developed at the University of Bremen by Dr. Vladimir Rozanov and Dr. Alexei Rozanov. Chapter 4 contains a description of the SCIATRAN model in its

current state. To compare polarized RTMs Dr. Liebing of the Institute of Environmental Physics and the Institute of Remote Sensing at the University of Bremen has made available a series of initial conditions and radiative transfer results. The chapter continues by outlining how SASKTRAN was configured to match, as closely as possible, the configuration used in the polarized SCIATRAN calculations. The chapter includes a direct comparisons of the results produced by the two polarized models and a discussion of the possible causes for their disagreement.

Chapter 4 also shows results for both the scalar SASKTRAN and vector SASKTRAN after correcting for Wood's anomalies with different aerosol distributions. Simulated retrieval vectors were derived from these calculations and the differences between scalar and vector results are discussed. The significant results of this work and possible future developments are summarized in Chapter 5.

Chapter 2

Background

The nature of computer RTM development requires the understanding of a variety of physical theory and technical knowledge. This chapter serves to introduce the theoretical and practical foundation for this thesis work. It will present the physical theory used to describe the polarization of light, which is used in radiative transfer modeling. It also provides an account of the practical methods used in RTMs, how the SASKTRAN model is structured, and the changes that must be implemented to create a polarized version of SASKTRAN.

The first section includes a derivation of the equation of radiative transfer to illustrate the meaning and importance of the equation's terms. Analytic solutions to the radiative transfer equation pose many difficulties and in some cases are not achievable so this section goes on to explain a numerical process called the method of successive orders of scattering. In practice the implementation of these equations and techniques may differ drastically between computational RTMs so to change and improve upon SASKTRAN its specific internal structure must be understood. The subsequent section includes a functional description of SASKTRAN's components and organization. Stokes Vectors and phase matrices for Rayleigh scattering and Mie scattering are derived from basic electromagnetic theory to aid in the understanding of the polarization of light. This chapter closes with a presentation of polarized radiative transfer equations as well as a description of the changes to SASKTRAN that are required to develop a polarized RTM.

2.1 Radiative Transfer Modeling

Understanding the radiation field in the atmosphere has been a goal of physicists since Lord Rayleigh attempted to explain the observed colour and polarization of light from the sky in 1871. The development of the equation of radiative transfer by *Chandrasekhar* (1960) allowed rigorous analysis of the transmission of radiation in the atmosphere. Since then the interest in computational RTMs has increased considerably as they may be used by inversion algorithms to retrieve atmospheric parameters from direct measurements. The accuracy of this retrieval process necessarily depends on the accuracy of the RTM and this motivates research into the improvement of these models.

2.1.1 Equations of Radiative Transfer

The power, in terms of photons, transmitted by a monochromatic field from a small surface element, $\mathrm{d}A$, into a small solid angle element, $\mathrm{d}\Omega$, in the direction $\hat{\Omega}$, in a time $\mathrm{d}t$, at the position $\underline{r}$ is the radiance, $I(\underline{r}, \hat{\Omega})$. Therefore, the units of radiance are

$$\left[I(\underline{r}, \hat{\Omega})\right] = \frac{\text{photons}}{\text{s} \quad \text{cm}^2 \quad \text{str} \quad \text{nm}}. \tag{2.1}$$

The coordinates for this radiant field are depicted in Figure 2.1. At the point of interest a local primed coordinate system is defined that has been rotated such that $\hat{z}'$ is parallel to $\underline{r}$. This provides a description of the intensity of the radiant field at one point, in one direction, but we are concerned with the transfer of radiation from one point to another. For this purpose the parametrization coordinate s will be introduced. Point $\underline{r}$ will be written as the equation:

$$\underline{r} = \underline{r}_o + \hat{\Omega} s \tag{2.2}$$

where $\underline{r}_o$ is a reference position where the radiance is incident and s is a distance measured parallel to $\hat{\Omega}$ as depicted in Figure 2.2. The radiant field along a given path will then be written as $I(s)$.

As radiation travels along a path it will be attenuated as it interacts through absorption or scattering with the atmospheric constituents. The probability of interaction per particle for a particular species quantified in units of area, $\sigma_i(s)$, is called the species cross section where the index i refers to a particular species. Both the cross section and the volume number density $n_i(s)$, which has units of inverse volume, depend on

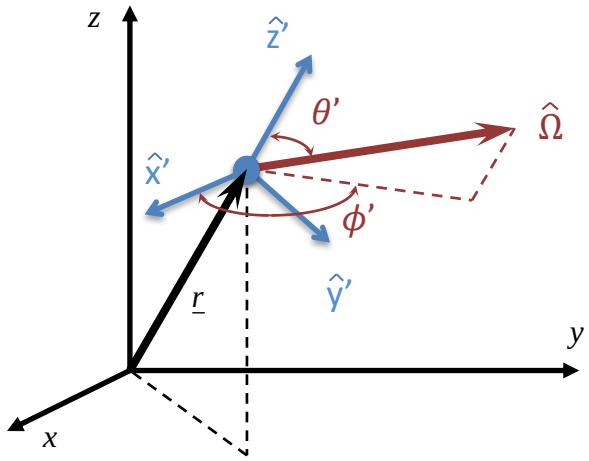

Figure 2.1: Specifying the radiant field requires three spacial coordinates to define the position and two coordinates for the directional distribution

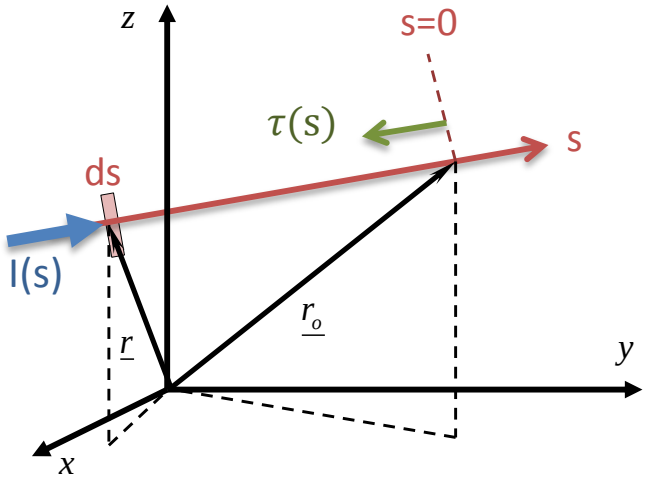

Figure 2.2: The path length coordinate s is defined to be zero at the observation point and increases in the direction of radiation propagation. Figure adapted from *Bourassa* (2007).

the position along the path of propagation. The total extinction, $\chi(s)$, can therefore be found by the summation over all species or,

$$\chi(s) = \sum_i \sigma_i(s) n_i(s), \tag{2.3}$$

and has units of inverse length. The change in the radiance through an extremely short

path length, ds, due to extinction is

$$\frac{\mathrm{d}I(s,\hat{\Omega})}{\mathrm{d}s} = -\chi(s)I(s,\hat{\Omega}). \tag{2.4}$$

We rearrange Equation 2.4 and formulate it as an integral to solve for I,

$$\int_{I(s,\hat{\Omega})}^{I(0,\hat{\Omega})} \frac{\mathrm{d}I'(s,\hat{\Omega})}{I'(s,\hat{\Omega})} = -\int_{s}^{0} \chi(s')\mathrm{d}s'. \tag{2.5}$$

Defining the optical depth as a dimensionless quantity that is the fraction of light attenuated by a path length of s. It must be related to the extinction by the equation

$$\mathrm{d}\tau(s) = -\chi(s)\mathrm{d}s \tag{2.6}$$

where the negative sign occurs because the s and τ are antiparallel coordinates with a common origin as depicted in Figure 2.2; so s is negative and decreasing where τ is positive and increasing. It is worth noting that for a homogeneous layer of thickness s the optical depth is simply

$$\tau = \chi(s)s. \tag{2.7}$$

Therefore we may rewrite Equation 2.5 in terms of the optical depth,

$$\int_{I(s,\hat{\Omega})}^{I(0,\hat{\Omega})} \frac{\mathrm{d}I'(s,\hat{\Omega})}{I'(s,\hat{\Omega})} = -\int_{\tau(s)}^{\tau(0)} \mathrm{d}\tau'. \tag{2.8}$$

The result is,

$$\ln\left(\frac{I(0,\hat{\Omega})}{I(s,\hat{\Omega})}\right) = \tau(0) - \tau(s), \tag{2.9}$$

and the optical depth is zero at $s = 0$ by definition so we may rearrange this expression to obtain the radiance at a reference point in terms of the radiance at any point along the path and the optical depth,

$$I(0,\hat{\Omega}) = I(s,\hat{\Omega})e^{-\tau(s)}. \tag{2.10}$$

This analysis provides an expression for how light is attenuated along a line of sight due to scattering and absorption and thus far has included no source terms. However, light from all directions will be scattered into the line of sight as well necessitating the addition of a source term, J, to Equation 2.4,

$$\frac{\mathrm{d}I(s,\hat{\Omega})}{\mathrm{d}s} = \chi(s)(-I(s,\hat{\Omega}) + J(s,\hat{\Omega})). \tag{2.11}$$

Because the source term receives contributions from all directions, an exact solution for this equation requires simultaneously solving for the entire atmosphere.

For wavelengths where there is no photochemical emission and where blackbody thermal emission is negligible compared to scattering ($< 2\,\mu$m, (*Bourassa*, 2007)) we can write the source function as an integral of the radiance over all directions as it is scattered into the direction $\hat{\Omega}$,

$$J(s,\hat{\Omega}) = \frac{\chi_{\text{scat}}(s)}{\chi(s)} \int_{4\pi} I(s,\hat{\Omega}')p(s,\hat{\Omega},\hat{\Omega}')\mathrm{d}\Omega'. \tag{2.12}$$

The dimensionless phase function, $p(s,\hat{\Omega},\hat{\Omega}')$, defines the probability that light traveling in the original propagation direction, $\hat{\Omega}'$, will be scattered into the direction $\hat{\Omega}$. Here it is also shown to depend on the argument s to account for the change in the properties of the scatterers with position. The scalar phase function corresponds to the first element of a phase matrix, described in Section 2.3. The source term as defined this way has the same units as the radiance or,

$$\Big[J(s,\hat{\Omega})\Big] = \frac{\text{photons}}{\text{s}\quad \text{cm}^2\quad \text{str}\quad \text{nm}}. \tag{2.13}$$

Because the species that absorb radiation do not contribute to the source term the fraction $\frac{\chi_{\text{scat}}(s)}{\chi(s)}$ is required where $\chi_{\text{scat}}(s)$ is the extinction that is due to scattering alone and does not include absorption. Using Equation 2.6 we may rewrite the left hand side of Equation 2.12 as $J(\tau,\hat{\Omega})$.

Now we may rearrange Equation 2.11 to obtain:

$$\frac{\mathrm{d}I(\tau,\hat{\Omega})}{\mathrm{d}\tau} - I(\tau,\hat{\Omega}) = -J(\tau,\hat{\Omega}). \tag{2.14}$$

We will substitute the derivative,

$$\frac{\mathrm{d}}{\mathrm{d}\tau}\left(I(\tau,\hat{\Omega})e^{-\tau}\right) = e^{-\tau}\left(\frac{\mathrm{d}I(\tau,\hat{\Omega})}{\mathrm{d}\tau} - I(\tau,\hat{\Omega})\right) \tag{2.15}$$

into Equation 2.14 to obtain the integrable form of the equation,

$$\frac{\mathrm{d}}{\mathrm{d}\tau}\left(I(\tau,\hat{\Omega})e^{-\tau}\right) = -J(\tau,\hat{\Omega})e^{-\tau}. \tag{2.16}$$

The integral from a reference point, τ_o, to any point along the path, τ, is

$$I(\tau,\hat{\Omega})e^{-\tau} - I(\tau_o,\hat{\Omega})e^{-\tau_o} = -\int_{\tau_o}^{\tau} J(\tau',\hat{\Omega})e^{-\tau'}\mathrm{d}\tau'. \tag{2.17}$$

By choosing the reference point to be at the observer (where $\tau_o = 0$) and the optical depth τ to where the line of sight exits the atmosphere or intersects the Earth, we obtain an expression for the observed radiance along the line of sight,

$$I(0, \hat{\Omega}) = I(\tau, \hat{\Omega})e^{-\tau} + \int_0^\tau J(\tau', \hat{\Omega})e^{-\tau'}\mathrm{d}\tau'. \tag{2.18}$$

It is important to keep in mind that in the coordinates shown in Figure 2.2 the optical depth is zero at the observer at $\underline{r}_o$. So the equation above applies to any position and any line of sight and to emphasize this point it may be rewritten as

$$I(\underline{r}_o, \hat{\Omega}) = I(\tau, \hat{\Omega})e^{-\tau} + \int_0^\tau J(\tau', \hat{\Omega})e^{-\tau'}\mathrm{d}\tau'. \tag{2.19}$$

So the observed radiance depends on the source function along a line of sight, and the source function depends on the radiance that arrives at each point from all directions as shown by Equation 2.12. Therefore to evaluate this equation one must solve the entire atmosphere simultaneously. By employing some simplifying assumptions, like assuming the atmosphere is composed of parallel homogeneous planes an analytic solution proves to be difficult but possible. When using more accurate geometries solving Equation 2.19 analytically may be impossible.

2.1.2 Successive Orders of Scattering

To avoid simultaneously solving the equations of radiative transfer for the entire atmosphere it is possible to employ a technique called the method of successive orders. In this model it is possible to calculate the radiance that has been scattered n times, called the n^{th} order, from the light that has been scattered $n-1$ times. In this method the light is first propagated from the sun to source points in the atmosphere and on the ground. The light is then scattered into outward directions that have been discretized over the entire 4π solid angle to create the first order source terms. This source is propagated throughout the atmosphere and scattered again to make the second order source terms. The second order is propagated to produce the third and so on. In this way the total radiance at any point in the atmosphere is the sum of the individual orders.

It is convenient to group the scattering events into four categories: single scatter from the atmosphere, single scatter from the ground, multiple scatter from the atmosphere and multiple scatter from the ground. These cases are handled separately in the SASKTRAN implementation.

Light that is scattered once is calculated directly. Points along an observer's line of sight are chosen to be the source points. Sunlight is propagated through the atmosphere to those points where it is scattered into the line of sight and propagated to the observer. If the direction of the sun is $\hat{\Omega}_s$, the line of sight is in the direction $\hat{\Omega}$, F_s is the sun's irradiance, and $p(s, \hat{\Omega}, \hat{\Omega}_s)$ is the scalar phase function then we can write the atmospheric single scatter contribution as,

$$I_{a1}(s_0, \hat{\Omega}) = \int_{s_0}^{s_1} J_{a1}(s, \hat{\Omega}) e^{-\tau(s)} \chi(s) \mathrm{d}s \tag{2.20}$$

where the single scatter source term is

$$J_{a1}(s, \hat{\Omega}) = \frac{\chi_{\text{scat}}(s)}{\chi(s)} e^{-\tau(\text{sun},s)} p(s, \hat{\Omega}, \hat{\Omega}_s) F_s. \tag{2.21}$$

Here light is collected and attenuated along the line of sight from where the line of sight terminates at s_1 back to the observer position s_0. If the observer's line of sight ends at the ground then a contribution, I_{g1}, is calculated by propagating light from the sun to that point on the surface where it is scattered in a Lambertian sense, before propagating back to the observer. If the line of sight does not intersect the ground then the term I_{g1} is zero. Using a for the albedo and s_g for the point on the ground the single scatter term from the ground is

$$I_{g1}(s_0, \hat{\Omega}) = \frac{a}{\pi} e^{-\tau(\text{sun},s_g)} e^{-\tau(s_g,s_0)} F_s \cos(\theta_{\text{sza}}), \tag{2.22}$$

where θ_{sza} is Solar Zenith Angle (SZA), which is the angle between the local vertical direction at the Earth's surface and the direction to the sun.

The second order atmospheric source term is calculated at each source point by substituting Equations 2.20 and 2.22, the incoming radiance produced by the first order of scattering, into Equation 2.12,

$$J_{a2}(s, \hat{\Omega}) = \frac{\chi_{\text{scat}}(s)}{\chi(s)} \int_{4\pi} p(s, \hat{\Omega}, \hat{\Omega}') \left[I_{a1}(s, \hat{\Omega}') + I_{g1}(s, \hat{\Omega}') \right] \mathrm{d}\Omega'. \tag{2.23}$$

The I_{a1} and I_{g1} terms bring the first order atmospheric radiance and ground radiance to the position s from the direction $\hat{\Omega}'$. The integral in terms of $\hat{\Omega}'$ acts to collect this incoming radiance from all directions and scatter it in the outward direction, $\hat{\Omega}$. The second order radiance from atmospheric scattering is therefore

$$I_{a2}(s_0, \hat{\Omega}) = \int_{s_0}^{s_1} \chi(s) e^{-\tau(s)} J_{a2}(s, \hat{\Omega}) \mathrm{d}s. \tag{2.24}$$

By applying Lambertian scattering to radiance inbound from all upward directions the second order ground term is,

$$I_{g2}(s_0, \hat{\Omega}) = \frac{a}{\pi} e^{-\tau(s_g, s_0)} \int_{2\pi} I_{a1}(s_g, \hat{\Omega}') \cos(\theta') \mathrm{d}\Omega'. \tag{2.25}$$

In this fashion source functions for each order of scattering are found using the previous order so the equations for the n^{th} order atmospheric scattering can be generalized to

$$J_{an}(s, \hat{\Omega}) = \frac{\chi_{\text{scat}}(s)}{\chi(s)} \int_{4\pi} p(s, \hat{\Omega}, \hat{\Omega}') \left[I_{a(n-1)}(s, \hat{\Omega}') + I_{g(n-1)}(s, \hat{\Omega}') \right] \mathrm{d}\Omega', \tag{2.26}$$

and

$$I_{an}(s_0, \hat{\Omega}) = \int_{s_0}^{s_1} J_{an}(s, \hat{\Omega}) e^{-\tau(s)} \chi(s) \mathrm{d}s. \tag{2.27}$$

We can also generalize the ground scattering contribution to the n^{th} order to obtain

$$I_{gn}(s_0, \hat{\Omega}) = \frac{a}{\pi} e^{-\tau(s_g, s_0)} \int_{2\pi} I_{a(n-1)}(s_g, \hat{\Omega}') \cos(\theta') \mathrm{d}\Omega'. \tag{2.28}$$

The total radiance that reaches an observer can be found by summing the contributions from all the orders or,

$$\begin{aligned} I(s_0, \hat{\Omega}) = \int_{s_0}^{s_1} \chi(s) e^{-\tau(s)} \left[J_{a1}(s, \hat{\Omega}) + J_{a2}(s, \hat{\Omega}) + \sum_{n=3}^{\infty} J_{an}(s, \hat{\Omega}) \right] \mathrm{d}s \\ + \left[I_{g1}(s_0, \hat{\Omega}) + I_{g2}(s_0, \hat{\Omega}) + \sum_{n=3}^{\infty} I_{gn}(s_0, \hat{\Omega}) \right] \end{aligned} . \tag{2.29}$$

The first two orders of source terms have been taken out of their summations for computational reasons that will be explained later. In following sections the differences between the first two orders of scattering and higher orders of scattering will be explained and this equation may serve as a reminder of that fact.

Because of the recursive nature of these equations the calculations must be made in order. The source functions and ground scattering components of the previous order must be found prior to the calculation of the source functions and ground scattering components of the current order. As radiation propagates throughout the atmosphere it is eventually absorbed or escapes the atmosphere; therefore the contribution from each order of scattering is smaller than the preceding order and the first order contributes the greatest to the observed signal. This technique converges to a solution in three to four orders of scattering for the red end of the visible spectrum and may require up to twenty orders for the blue end (*Bourassa*, 2007).

2.2 SASKTRAN

Traditionally RTMs assumed the atmosphere could be represented by homogeneous parallel planes, which simplifies the mathematics of radiative transfer a great deal (*Chandrasekhar*, 1960). Such models show good agreement for nadir viewing geometries but it has long been known that one must resort to a spherical shell model of the atmosphere for limb viewing geometries due to the significant contribution of light scattered multiple times (*Collins et al.*, 1972). SASKTRAN uses an atmosphere of spherical homogeneous cells of variable thickness.

There are three types of scatterers included in the SASKTRAN atmosphere; molecules, aerosols, and the ground. Scattering by molecules and aerosols is calculated using geographic position dependant cross sections, number densities and phase functions. The Rayleigh phase functions, which are used for scattering by molecular species and are derived in Section 2.3.2, are computed directly by SASKTRAN code. The Mie phase functions, which are used for aerosols and are described in Section 2.3.3, are calculated using code developed by *Wiscombe* (1980). Scattering from the ground is Lambertian and is calculated directly using a non-uniform illumination of the ground (*Bourassa et al.*, 2008), as in Equations 2.22, 2.25, and 2.28.

SASKTRAN is a C++ based code library developed at the University of Saskatchewan; it is available both as source code and a collection of Dynamically-Linked Libraries (DLL). It heavily employs the Object Oriented (OO) design paradigms that C++ offers. The model has a high degree of modularity that allows for effective multithreading. OO design also allows the use of inheritance and polymorphism to promote code reuse and easily extending existing classes for future improvements.

The goal of this thesis work is to modify SASKTRAN such that it may model polarized radiative transfer, making it a more valuable tool in the retrieval of information about the atmosphere. The polarized or vector SASKTRAN will be designed to minimize the impact on speed and memory resources. The modifications will also be designed to change the structure of the model as little as possible to maintain usability and encourage future development. The vector SASKTRAN will be capable of switching to non-polarized calculations as well to further reduce the performance impact when the user is modeling situations where polarization is not critical. In the following section the structure of SASKTRAN, especially portions that are relevant to the thesis work, will be described.

2.2.1 The Organization of SASKTRAN

Conceptually, the SASKTRAN model consists of four main components: Lines of Sight, Diffuse Scattering Points, vertical Profiles of diffuse points, and the Observer Line of Sight. These components work with each other to quickly and accurately compute the radiance received by the observer. They are structured to take advantage of symmetry that arises in the model and work well in a multithreaded environment.

A Line of Sight (LOS) is a geometric ray that starts at a known point in space and extends outwards in a specific direction. Positions are chosen at intervals along the length of the ray to find the source function terms, J_{a1}. Sunlight is propagated through the atmosphere to these points and scattered into the direction of the LOS to directly calculate the source functions at these points according to Equation 2.21. If the ray intersects the ground then light is also propagated down to that intersection point and it is scattered outwards. The LOS uses these source functions to find the single scatter contributions to the radiance from the atmosphere and the ground following Equations 2.20 and 2.22 respectively as is illustrated in Figure 2.3.

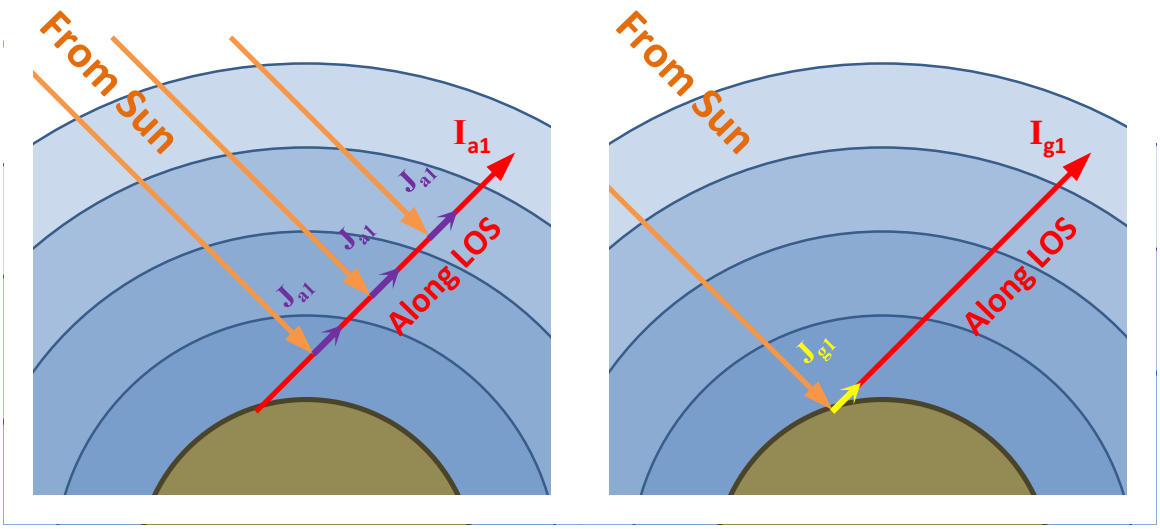

Figure 2.3: Schematic of first order radiance calculated by a SASKTRAN Line of Sight component.

The Diffuse Scattering Points (DSPs) are the components of SASKTRAN that provide source function values for light scattered multiple times. Each DSP possesses multiple LOSs whose rays are distributed over all directions. The DSP uses its LOSs to determine the radiance from the previous order of scattering, the $n-1$ terms in

Equation 2.26, before scattering this radiance outwards again to obtain the source function values, J_{an}. This is shown schematically in Figure 2.4.

Once the source functions have been found, they are used while integrating along the LOSs to find the n^{th} order radiance for each LOS. To obtain the source function in the direction of a LOS it is interpolated from surrounding precalculated source functions as depicted in Figure 2.5 because the source function values have been determined at set directions. To obtain the source functions actually at points along the LOS the source functions are linearly interpolated from the DSP positions to those points. Once these interpolations are complete the n^{th} order of atmospheric radiance along the LOS, I_{an} may be found by applying Equation 2.27.

Because SASKTRAN uses Lambertian scattering for the ground, directional interpolation is not required for the ground based contribution. If the LOS intersects the Earth spatial interpolations from diffuse points on the ground are still required and the contribution represented by Equation 2.28 is calculated.

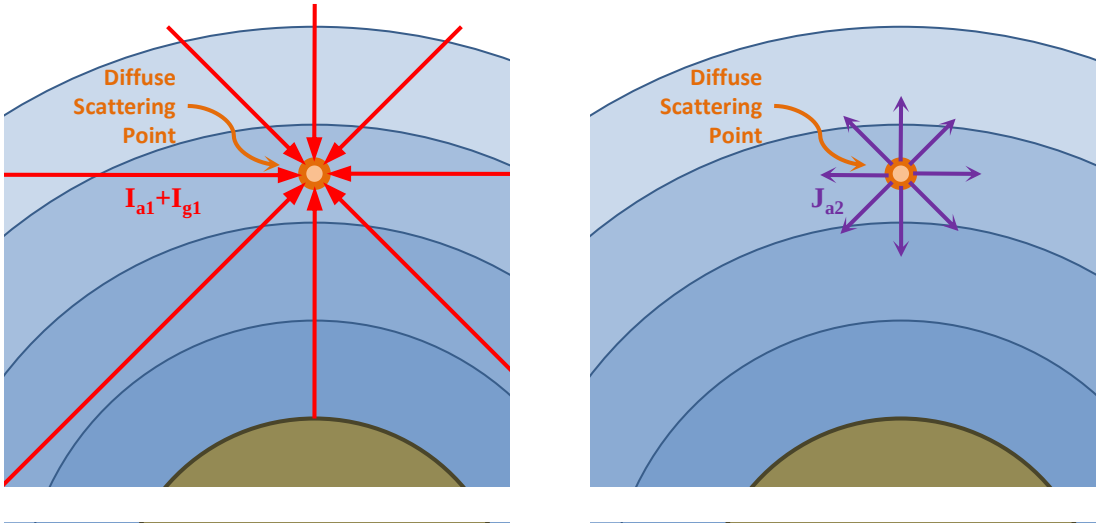

Figure 2.4: Each Diffuse Scattering Point uses its Lines of Sight to find the first order radiance values. These radiance values are then used by the DSP to calculate the second order source functions.

In the current release version of SASKTRAN it is assumed that the atmosphere can be accurately approximated by homogeneous spherical cells. The vertical profiles of diffuse points are collections of DSPs. Each profile has a diffuse point on the boundary of each spherical cell, and in the center of each cell. It is known that for spherical shell atmospheres the radiance in a given spherical cell will be symmetrical with respect to

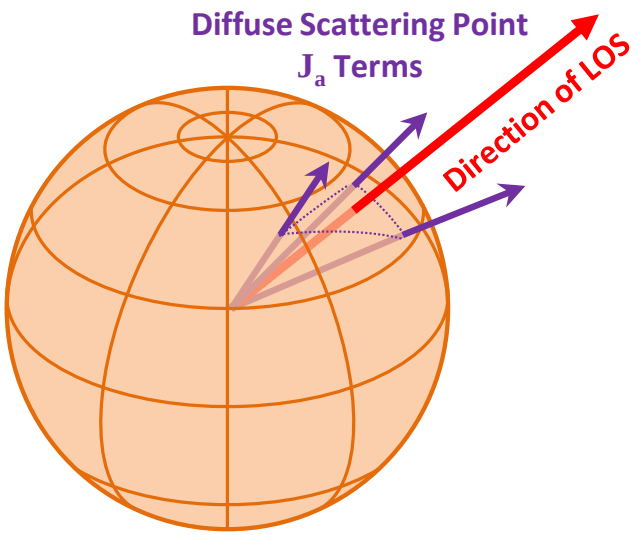

Figure 2.5: Each DSP has source functions precalculated for directions evenly distributed over a unit sphere. Source functions for nearby directions are selected and used to interpolate the source function at the LOS direction.

Solar Azimuth Angle (SAA), for example see the work by *Lenoble and Sekera* (1961). We can exploit this symmetry by only calculating source functions values at varying SZAs. This drastically reduces the number of diffuse Profiles required to calculate the radiance field. SASKTRAN places the diffuse Profiles at select SZA intervals along the path of the Observer Line of Sight as illustrated in Figure 2.6. This also means that the spatial interpolation from the DSPs to a LOS is reduced from a three dimensional interpolation to interpolation with respect to altitude and SZA alone.

The Observer Line of Sight (OLOS) is the component of SASKTRAN that calculates the radiance received by the observer at the requested viewing geometry. Just like a LOS it calculates its first order atmospheric and ground source functions directly and the source functions from higher orders of scattering are interpolated from the DSPs. These second order source function values produced by DSPs are based on first order source functions calculated directly by the LOSs. This direct computation of source functions makes the first two orders of radiance at the observer, which contribute the most to the final signal, highly accurate. Every higher order of observed radiance is found from interpolated source functions but higher order radiance contributes much less to the final signal as demonstrated by *Bourassa* (2007) for OSIRIS wavelengths. Equation 2.29 separates the first and second order radiances from the summation of

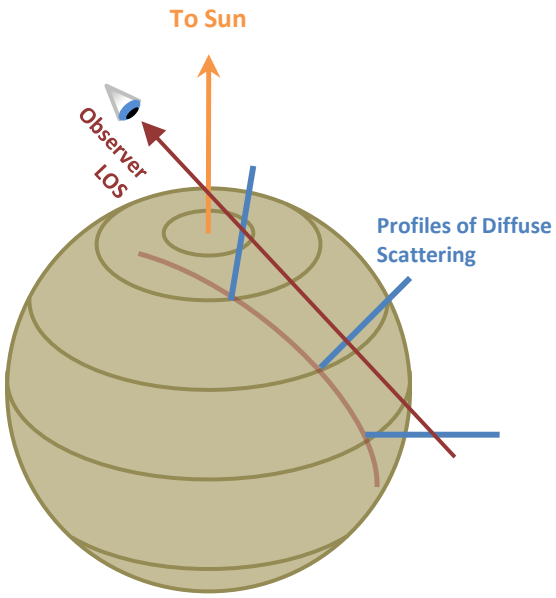

Figure 2.6: Schematic of Profiles placed along the Observer Line of Sight, at select SZA intervals.

higher orders to illustrate this difference.

To carry out the necessary calculations the equations of radiative transfer shown in Section 2.1.2 must be rewritten to approximate the integrals and interpolate values through discrete summations. The irradiance from the sun, attenuated down to the i^{th} point, is

$$F_i = F_s e^{-\tau(sun,s_i)} \tag{2.30}$$

which is used in the following equations to find the first order atmospheric and ground radiance at the j^{th} location for direction $\hat{\Omega}$:

$$I_{a1j}(\hat{\Omega}) = \sum_i f_{a1i} F_i \tag{2.31}$$

and

$$I_{g1j}(\hat{\Omega}) = f_{g1} F_g. \tag{2.32}$$

The factors in these summations are

$$f_{a1i} = \chi_{\text{scat}i} p_i(\hat{\Omega}, \hat{\Omega}_{\text{sun}}) e^{-\tau_i} \Delta s_i \tag{2.33}$$

and

$$f_{g1} = \frac{a}{\pi} \cos(\theta_{\text{sza}}) e^{-\tau(s_g,s_j)}. \tag{2.34}$$

The n^{th} order source function for the j^{th} DSP in the k^{th} direction may be written as

$$J_{anj}(\hat{\Omega}_k) = \sum_i f_{Jai} \left[I_{a(n-1)j}(\hat{\Omega}_i) + I_{g(n-1)j}(\hat{\Omega}_i) \right] \tag{2.35}$$

with a summation factor of $f_{Jai} = \chi_{\text{scat}j} p_j(\hat{\Omega}_k, \hat{\Omega}_i) \Delta\Omega_i$. Figure 2.7 schematically shows this calculation as it takes place in a DSP.

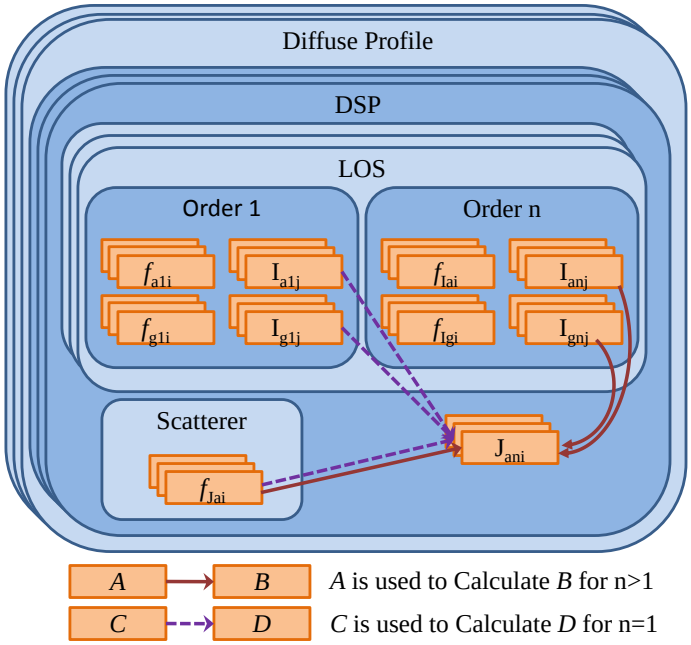

Figure 2.7: Each DSP finds a set of outbound source functions J_{ani} from the $n-1$ radiance terms produced by the DSP's LOSs.

The n^{th} order atmospheric radiance has additional summations to interpolate source functions. The summation over j uses the weighting factor ζ_j to interpolate between diffuse points in terms of altitude and solar zenith angle. The summation over k uses the weighting factor ξ_k to interpolate between outbound directions at a given DSP. The n^{th} order atmospheric radiance at the l^{th} location may be written as

$$I_{anl} = \sum_i \left\{ e^{-\tau_i} \Delta s_i \sum_j \left[\zeta_j \sum_k \left(\xi_k J_{anj}(\hat{\Omega}_k) \right) \right] \right\} \tag{2.36}$$

or, as in SASKTRAN, the inner summations may be "unrolled" and the equation can simply be rewritten as

$$I_{anl} = \sum_i f_{Iai} J_{ani}(\hat{\Omega}_i) \tag{2.37}$$

with a factor of $f_{Iai} = e^{-\tau_i}\Delta s_i \zeta_i \xi_i$. The n^{th} order ground radiance at the l^{th} location is found through the equation

$$I_{gnl} = \sum_i f_{Igi} I_{a(n-1)g}(\hat{\Omega}_i) \tag{2.38}$$

with a factor of $f_{Igi} = \frac{a}{\pi} e^{-\tau(s_g, s_l)} \cos(\theta_i)\Delta\Omega_i$. These calculations are shown schematically in Figure 2.8 as they occur in the LOS and OLOS modules.

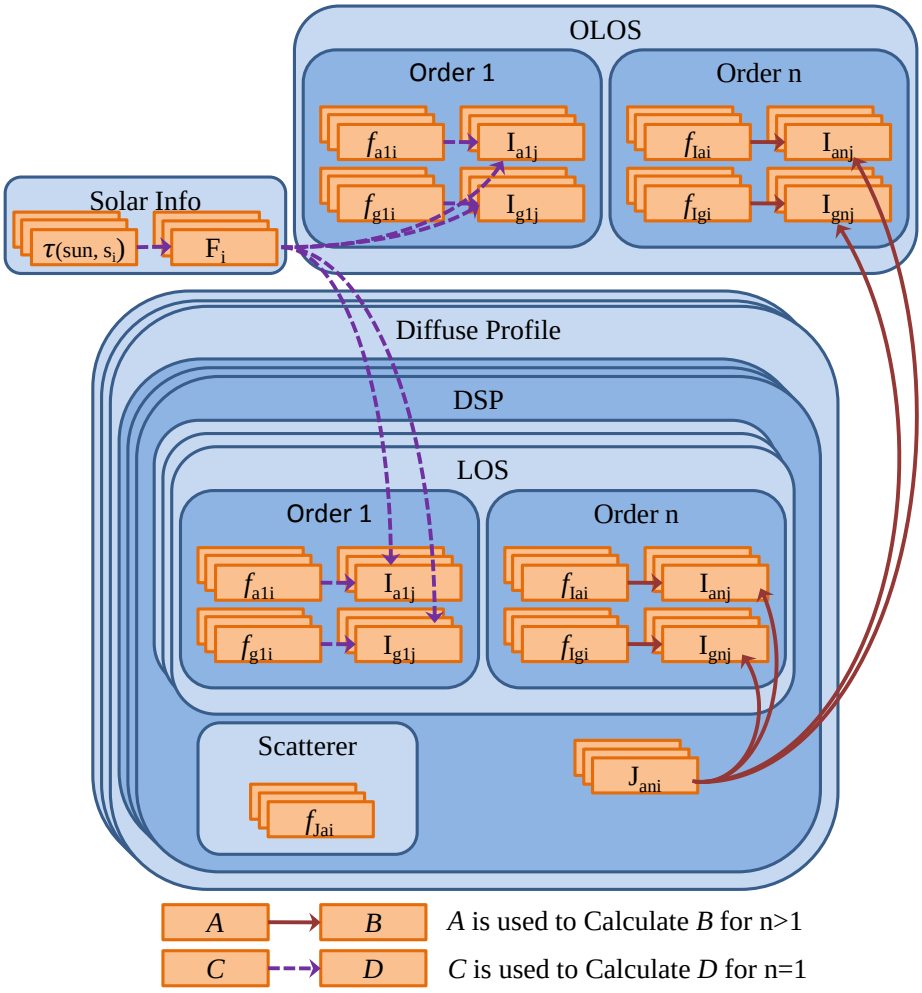

Figure 2.8: Each LOS and OLOS finds the atmospheric and ground radiance for each order. The second and higher orders of radiance are interpolated from the source functions calculated by the DSPs.

The factors f_{Jai}, f_{Iai}, and f_{Igi} depend on the optical properties of the atmosphere or ground and on geometry but do not depend on the order of scattering. This means that for each wavelength these factors only need to be computed once and after that

initial setup SASKTRAN can quickly iterate through many orders of scattering by evaluating these summations repeatedly in sequence.

SASKTRAN has been constructed to be capable of multithreaded processing to take advantage of multiple core computers, which have become ubiquitous in recent years. Initial set up and calculations in SASKTRAN are performed by a thread that creates, manages, and coordinates other threads that are used for processing. Because the scattering and absorption processes are wavelength dependent each wavelength of radiation requires its own set of radiative transfer calculations. Each of the processing threads is given a wavelength to process independently. The four components of SASKTRAN described above are structured in a way that keeps the information based on geometry alone partitioned from information that is dependant on the wavelength of the light. This way the geometry information, such as the LOS path length, requires a single initialization by the manager thread and is thereafter shared by the different processing threads. Each processing thread generates the information that is wavelength dependent, for example the phase functions, before performing the radiative transfer calculations. When a processing thread completes its radiative transfer calculations the resulting radiance is returned to the manager thread and the manager starts the processing thread on a new wavelength if there are any remaining.

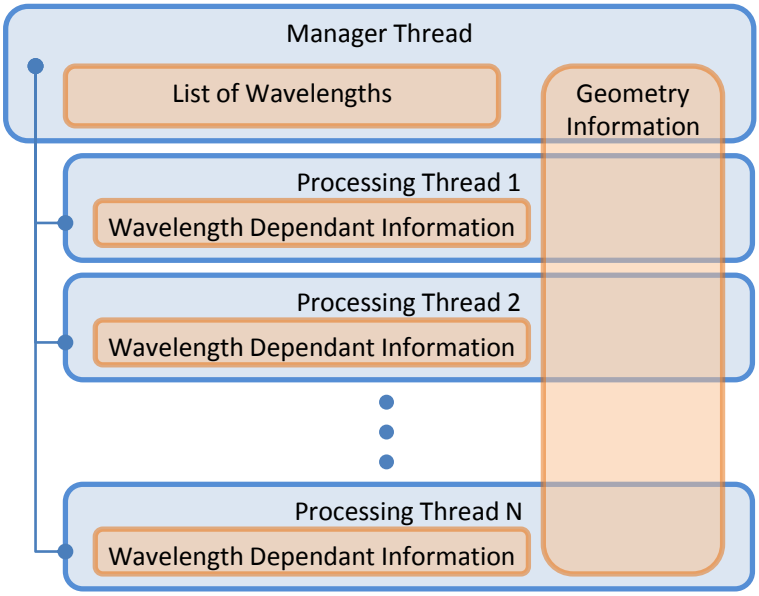

Figure 2.9: Separate threads process different wavelengths in parallel but share geometry information, which is wavelength independent.

2.3 Polarized Light

2.3.1 Polarization and the Stokes Vector

In the electrically neutral atmosphere, where particles are separated by large distances with respect to their size, monochromatic light propagation is accurately modeled by a plane wave solution to the wave equation. In this case the electric and magnetic fields may be written as:

$$\underline{E}(\underline{r},t) = \mathrm{Re}\{\underline{\tilde{E}_o} e^{\pm i(\underline{k}\cdot\underline{r}\pm\omega t)}\} \quad \tfrac{\mathrm{N}}{\mathrm{C}} \tag{2.39}$$

and

$$\underline{H}(\underline{r},t) = \mathrm{Re}\{\underline{\tilde{H}_o} e^{\pm i(\underline{k}\cdot\underline{r}\pm\omega t)}\} \quad \tfrac{\mathrm{A}}{\mathrm{m}} \tag{2.40}$$

where underscores denote a vector quantity, tildes denote complex values that contain phase information, and 'Re' denotes 'the real part of'. In these equations $\underline{r}$ is the position, t is time, and E_o and H_o are the magnitudes of the electric field and magnetic fields. The value $\underline{k}$ is the wave vector, which points in the direction of wave propagation, and ω is the frequency of the light. In non-conducting media the wave number, which is the magnitude of the wave vector, and the frequency are related by the equations:

$$\omega = \tfrac{k}{\sqrt{\epsilon\mu}} = kc \quad \tfrac{1}{\mathrm{s}} \tag{2.41}$$

or

$$k = \tfrac{\omega}{c} = \tfrac{2\pi}{\lambda} \quad \tfrac{1}{\mathrm{m}} \tag{2.42}$$

where ϵ is the permittivity with units of $\frac{\mathrm{F}}{\mathrm{m}}$, μ is the permeability with units of $\frac{\mathrm{N}}{\mathrm{A}^2}$, λ is the wavelength with units of m, and c represents the speed of light with units of $\frac{\mathrm{m}}{\mathrm{s}}$.

By taking the appropriate derivatives of Equations 2.39 and 2.40, using the field definition for free space of $\mu\underline{H} = \underline{B}$, and substituting them into Maxwell's equations for free space (*Griffiths*, 1999) we obtain:

$$\begin{aligned}
\nabla\cdot\underline{E} = \tfrac{1}{\epsilon}\rho &\Rightarrow \underline{k}\cdot\underline{E} = 0 \\
\nabla\times\underline{E} = -\tfrac{\partial B}{\partial t} &\Rightarrow \underline{k}\times\underline{E} = \omega\mu\underline{H} \\
\nabla\cdot\underline{B} = 0 &\Rightarrow \underline{k}\cdot\underline{H} = 0 \\
\nabla\times\underline{B} = \mu\epsilon\tfrac{\partial E}{\partial t} &\Rightarrow \underline{k}\times\underline{H} = -\omega\epsilon\underline{E}
\end{aligned} \quad . \tag{2.43}$$

This demonstrates that the wave vector, the electric field, and the magnetic field are all mutually perpendicular. It also shows that any of the three vector quantities can be described completely by the other two, so for example we will proceed by describing the wave using only the electric field equation and the wave vector.

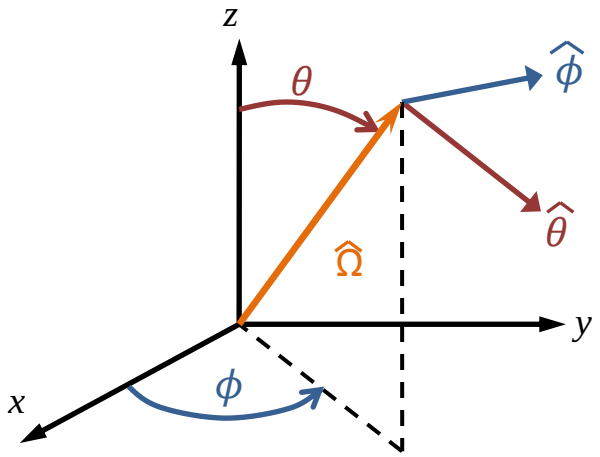

Figure 2.10: Polar coordinate system and unit vectors for wave propagation

We represent the wave propagating in direction $\hat{\Omega}$, where $\underline{k} = k\hat{\Omega}$, in polar coordinates as depicted in Figure 2.10. Because the field vectors are always perpendicular to the propagation we find that they always lie in the $\hat{\theta} - \hat{\phi}$ plane and that these three directions form a right handed coordinate system. Therefore we may always represent $\underline{\tilde{E}_o}$ with the components $\tilde{E}_\theta$ and $\tilde{E}_\phi$.

Under this coordinate system the real components of the electric field may also be written as:

$$\begin{aligned} E_\theta &= E_{o\theta} \cos(\Delta_\theta + \underline{k} \cdot \underline{r} - \omega t) \\ E_\phi &= E_{o\phi} \cos(\Delta_\phi + \underline{k} \cdot \underline{r} - \omega t) \end{aligned} \tag{2.44}$$

where Δ_θ and Δ_ϕ are the phases that were contained within the complex values $\underline{\tilde{E}_o}$ and $\underline{\tilde{H}_o}$ in Equations 2.39 and 2.40. It is clear that if we fix the location and vary time these equations trace out an ellipse that lies in the $\hat{\theta} - \hat{\phi}$ plane. The shape of the ellipse depends upon the magnitude of the two electric field components and the phase difference between them. This relationship is referred to as the polarization state of the wave. For example if the two components are exactly in phase the ellipse will be squashed down to a straight line, if they are exactly out of phase and of equal magnitude the ellipse becomes a circle. Ellipses corresponding to varying phase differences are depicted in Figure 2.11.

As stated above, it is possible to describe an electromagnetic plane wave knowing only the direction of propagation, the wave number (or equivalently the frequency, or wavelength), and the electric field. The electric field strength is not directly measurable and this poses complications when we are interested in experimentally learning about

the characteristics of a plane wave. To address this issue it is advantageous to introduce a measurable four element array called the Stokes Vector, $\underline{I}$. It is constructed from the $\hat{\theta}$ and $\hat{\phi}$ components of the electric field. The array's components are real valued combinations of the electric field components and their complex conjugates:

$$\mathrm{d}\Omega \cdot \underline{I} = \tfrac{1}{2}\sqrt{\tfrac{\epsilon}{\mu}} \begin{bmatrix} \tilde{E}_{o\theta}\tilde{E}^*_{o\theta} + \tilde{E}_{o\phi}\tilde{E}^*_{o\phi} \\ \tilde{E}_{o\theta}\tilde{E}^*_{o\theta} - \tilde{E}_{o\phi}\tilde{E}^*_{o\phi} \\ -2\mathrm{Re}\{\tilde{E}_{o\theta}\tilde{E}^*_{o\phi}\} \\ -2\mathrm{Im}\{\tilde{E}_{o\theta}\tilde{E}^*_{o\phi}\} \end{bmatrix} \quad \frac{\text{photons}}{\text{s} \quad \text{cm}^2 \quad \text{nm}} \tag{2.45}$$

where 'Im' stands for 'the imaginary part of'. The complex values $\tilde{E}_{o\theta}$ and $\tilde{E}_{o\phi}$ represent magnitudes and phase offsets and may be rewritten as $\tilde{E}_{o\theta} = E_{o\theta}e^{i\Delta_\theta}$ and $\tilde{E}_{o\phi} = E_{o\theta}e^{i\Delta_\phi}$. Using the expression $\Delta = \Delta_\theta - \Delta_\phi$ we can simplify Equation 2.45 so it becomes:

$$\mathrm{d}\Omega \cdot \underline{I} = \tfrac{1}{2}\sqrt{\tfrac{\epsilon}{\mu}} \begin{bmatrix} E^2_{o\theta} + E^2_{o\phi} \\ E^2_{o\theta} - E^2_{o\phi} \\ -2E_{o\theta}E_{o\phi}\cos\Delta \\ 2E_{o\theta}E_{o\phi}\sin\Delta \end{bmatrix} \quad \frac{\text{photons}}{\text{s} \quad \text{cm}^2 \quad \text{nm}} \ . \tag{2.46}$$

The factor of $\mathrm{d}\Omega$ represents the solid angle element that encloses the ray and has units of steradians.

The Poynting vector describes the instantaneous rate of energy flow through a unit area and in the case of a plane wave it lies parallel to the unit vector $\hat{\Omega}$ (*Griffiths*, 1999). It can be described by the equation:

$$\underline{S} = \tfrac{1}{\mu}\underline{E}(\underline{r}, t) \times \underline{H}(\underline{r}, t) \quad \tfrac{\mathrm{W}}{\mathrm{m^2nm}} \tag{2.47}$$

and its time averaged value, which we will call the irradiance, is the power transmitted per unit area:

$$\langle \underline{S} \rangle = \tfrac{1}{2\mu}(\underline{\tilde{E}_o} \times \underline{\tilde{H}_o}^*) \quad \tfrac{\mathrm{W}}{\mathrm{m^2nm}} \ . \tag{2.48}$$

Making use of Equations 2.42 and 2.43 we obtain:

$$\begin{aligned} \langle \underline{S} \rangle &= \tfrac{k}{2\mu\omega}(\tilde{E}_{o\theta}\tilde{E}^*_{o\theta} + \tilde{E}_{o\phi}\tilde{E}^*_{o\phi})\hat{\Omega} \\ &= \tfrac{1}{2}\sqrt{\tfrac{\epsilon}{\mu}}(E^2_{o\theta} + E^2_{o\phi})\hat{\Omega} \qquad \tfrac{\mathrm{W}}{\mathrm{m^2nm}} \ . \\ &= \tfrac{1}{2}\sqrt{\tfrac{\epsilon}{\mu}}|\underline{E}|^2\hat{\Omega} \end{aligned} \tag{2.49}$$

Comparing the first element of Equation 2.46 with Equation 2.49 one sees immediately that the first element is the power flowing through a unit of area. This means that the

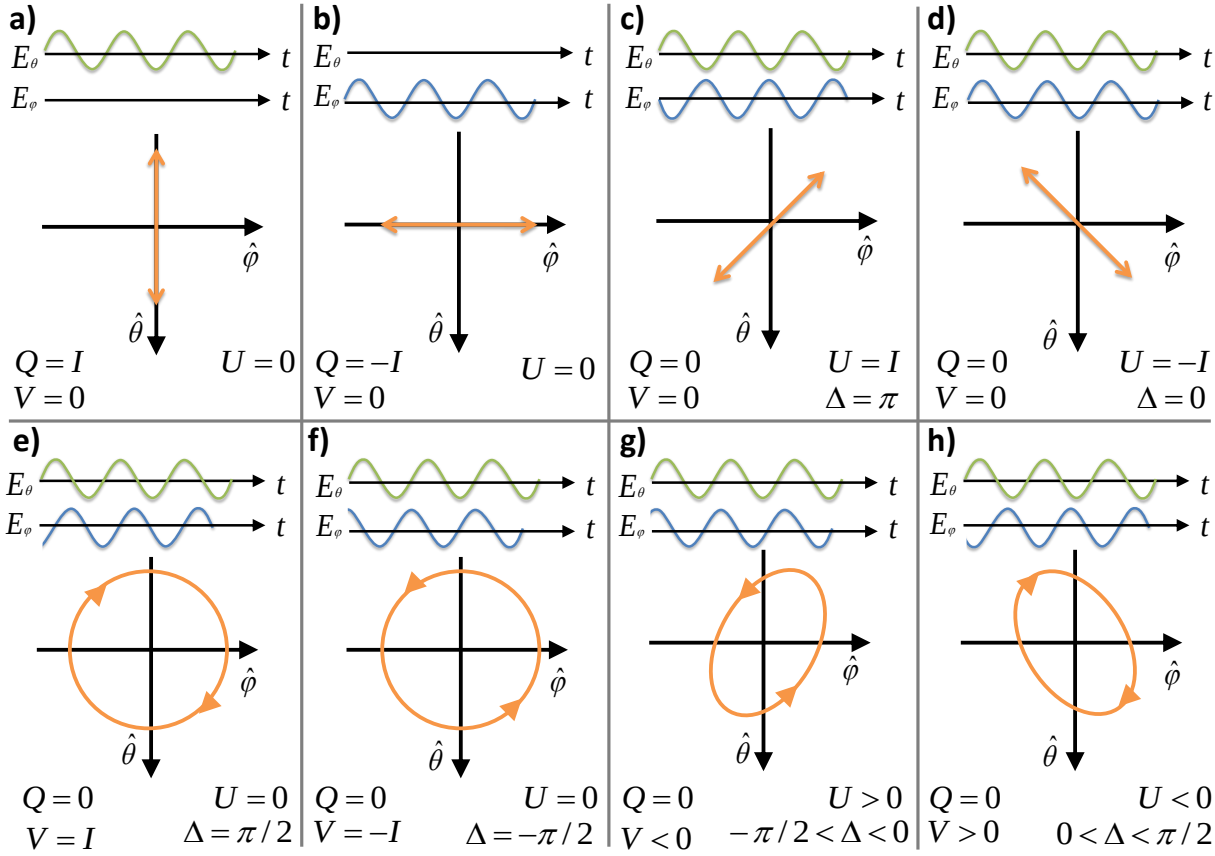

Figure 2.11: Polarization ellipses, traced by electric field vector, for varying phase differences. Axis orientation follows *Mishchenko et al.* (2002).

first element of $\underline{I}$ is the radiance and the entire vector may be written in units of

$$[\underline{I}] = \frac{\text{photons}}{\text{s} \quad \text{cm}^2 \quad \text{nm} \quad \text{str}}. \tag{2.50}$$

This first element is therefore the same as the radiance used in Section 2.1 where it is used in radiative transfer equations.

The second element of $\underline{I}$ is a measure of linear polarization and is regularly called Q. It will be equal to I when the wave is entirely polarized in the $\hat{\theta}$ direction and equal to -I when the wave is entirely polarized in the $\hat{\phi}$ direction. It may be measured using a photometer and a linear polarizer. These cases are shown in Figures 2.11 a) and b).

The third element, called U, is a measure of linear polarization along lines that are $\pm\pi/4$ radians from $\hat{\theta}$. If the two components are exactly in phase or anti-phase with each other and of the same magnitude then they will create a flat line and U will be equal to $\pm I$. These cases are shown in Figures 2.11 c) and d).

Finally the element called V is a measure of how circular the ellipse is. If the two perpendicular components of $\underline{E}$ have a phase offset of $\pm\frac{\pi}{2}$ and are of equal magnitude then the ellipse becomes a circle and V will be positive or negative I, depending on which component is leading or lagging. These cases are shown in Figures 2.11 e) and f). This quantity can be measured using a linear polarizer and quarter wave plate, which is a device that introduces a $\frac{\pi}{4}$ phase shift between the components.

The linear, $\pi/4$ linear, and circular components are different representations of the electric field; each pair of components corresponding to its own pair of orthogonal coordinates. Because of this orthogonality every polarization state can be constructed out of a pair of either linear, $\pi/4$ linear, or circular components. This is very useful since the Stokes vector derived from these components can all be directly measured. In the case of completely polarized light we we have the equality:

$$I^2 = Q^2 + U^2 + V^2. \tag{2.51}$$

Although this analysis has assumed the light was completely polarized it is possible, and indeed more common, for light to be randomly polarized or only partially polarized. In this case we have the inequality:

$$I^2 > Q^2 + U^2 + V^2. \tag{2.52}$$

This can simply be handled by superimposing a polarized wave with a wave that has a phase offset between the $\hat{\theta}$ and $\hat{\phi}$ components that changes randomly with time.

2.3.2 Scattering by Small Particles

Elastic scattering of electromagnetic radiation can be imagined as a two part process. First the incident radiation excites oscillations in the scatterer's charge carriers at the same frequency as the wave. Secondly, because the oscillating charge is accelerating it re-radiates outward. The scattered radiation is of the same frequency as that of the incident (*Mishchenko et al.*, 2002). Mathematically the scattering process can be represented by a matrix operation.

The shape, composition, and size of the scatterer relative to the wavelength of the radiation dictate how the radiation is scattered. If the wavelength and the scatterer are of comparable sizes the shape becomes very important. Consider a plane wave incident on a long rod shaped scatterer; modes of oscillation along the length of the rod will be excited to a different degree than modes across the width.

In cases where the wavelength is much larger than the scatterer we employ the Rayleigh approximation where the scatterer may be treated as a dipole oscillator induced by the incoming radiation (*Goody and Yung*, 1989). The Rayleigh approximation is of importance because it is applicable to the scattering of optical wavelengths by the vast majority of the atmospheric constituents. The derivation of the Rayleigh scattering matrix will be outlined below for illustration of the principles behind its use, and of the general process used to find Stokes transformation matrices.

The induced dipole moment of a Rayleigh scatterer is proportional to the electric field,

$$\underline{P} = \alpha \underline{E} \quad \text{Cm} \tag{2.53}$$

and from classical electromagnetic theory the radiant energy emitted by the dipole would be (*Lenoble*, 1993),

$$\begin{aligned} W &= \tfrac{ck^4}{12\pi\epsilon} \underline{P} \cdot \underline{P}^* \\ &= \tfrac{ck^4}{12\pi\epsilon} |\underline{P}|^2 \qquad \tfrac{\text{J}}{\text{s}} \ . \\ &= \tfrac{c\alpha^2 k^4}{12\pi\epsilon} |\underline{E}|^2 \end{aligned} \tag{2.54}$$

A value called the scattering cross section, σ_{scat}, and has units of area is defined as the ratio of the total power of the scattered radiation to the incident power per unit area. So using Equations 2.49 and 2.54 we find,

$$\sigma_{\text{scat}} = \tfrac{\alpha^2 k^4}{6\pi\epsilon^2} \quad \text{m}^2 \tag{2.55}$$

If we orient the $\hat{\theta} - \hat{\phi}$ plane such that $\hat{\theta}$ lies in a plane that contains the propagation directions of both the incident and outbound waves we may write the scattered electric field components as:

$$\begin{aligned} E_{\text{scat}\theta} &= \tfrac{k^2 \alpha E_\theta}{4\pi\epsilon r} e^{-ikr} cos(\Theta) \qquad \tfrac{\text{N}}{\text{C}} \\ E_{\text{scat}\phi} &= \tfrac{k^2 \alpha E_\phi}{4\pi\epsilon r} e^{-ikr} \end{aligned} \tag{2.56}$$

where Θ is the angle between the inbound and outbound directions. A complete derivation of these equations are presented in *Griffiths* (1999) although the form of this equation is closer to that found in *Lenoble* (1993). From these equations and

Equation 2.46 we can construct a scattered vector with the same units,

$$\begin{aligned} \mathrm{d}\Omega \cdot \underline{I}_{\mathrm{scat}} &= \tfrac{1}{2}\sqrt{\tfrac{\epsilon}{\mu}}\left(\tfrac{k^2\alpha}{4\pi\epsilon r}\right)^2 \begin{bmatrix} E_{o\theta}^2\cos^2\Theta + E_{o\phi}^2 \\ E_{o\theta}^2\cos^2\Theta - E_{o\phi}^2 \\ -2E_{o\theta}E_{o\phi}\cos\Delta\cos^2\Theta \\ 2E_{o\theta}E_{o\phi}\sin\Delta\cos^2\Theta \end{bmatrix} \\ &= \tfrac{1}{2}\sqrt{\tfrac{\epsilon}{\mu}}\tfrac{k^4\alpha^2}{16\pi^2\epsilon^2 r^2} \begin{bmatrix} E_{o\theta}^2\cos^2\Theta + E_{o\phi}^2 \\ E_{o\theta}^2\cos^2\Theta - E_{o\phi}^2 \\ -2E_{o\theta}E_{o\phi}\cos\Delta\cos^2\Theta \\ 2E_{o\theta}E_{o\phi}\sin\Delta\cos^2\Theta \end{bmatrix}. \end{aligned} \tag{2.57}$$

This ray is being scattered into some solid angle $\mathrm{d}\Omega$ that is related to a spherical surface area element $\mathrm{d}A = r^2\mathrm{d}\Omega$. For a unit surface area element we use $\mathrm{d}\Omega = \frac{1}{r^2}\mathrm{str}$ and we may rewrite the vector as,

$$\underline{I}_{\mathrm{scat}} = \frac{1}{2}\sqrt{\frac{\epsilon}{\mu}}\frac{k^4\alpha^2}{16\pi^2\epsilon^2} \begin{bmatrix} E_{o\theta}^2\cos^2\Theta + E_{o\phi}^2 \\ E_{o\theta}^2\cos^2\Theta - E_{o\phi}^2 \\ -2E_{o\theta}E_{o\phi}\cos\Delta\cos^2\Theta \\ 2E_{o\theta}E_{o\phi}\sin\Delta\cos^2\Theta \end{bmatrix}. \tag{2.58}$$

Therefore the problem reduces to finding the matrix $\underline{\mathbf{p}}_R(\Theta)$ from the equation:

$$\underline{I}_{\mathrm{scat}} = \sigma_{\mathrm{scat}}\underline{\mathbf{p}}_R(\Theta)\underline{I}, \tag{2.59}$$

or

$$\frac{3}{16\pi} \begin{bmatrix} E_{o\theta}^2\cos^2\Theta + E_{o\phi}^2 \\ E_{o\theta}^2\cos^2\Theta - E_{o\phi}^2 \\ -2E_{o\theta}E_{o\phi}\cos\Delta\cos^2\Theta \\ 2E_{o\theta}E_{o\phi}\sin\Delta\cos^2\Theta \end{bmatrix} = \underline{\mathbf{p}}_R(\Theta) \begin{bmatrix} E_{o\theta}^2 + E_{o\phi}^2 \\ E_{o\theta}^2 - E_{o\phi}^2 \\ -2E_{o\theta}E_{o\phi}\cos\Delta \\ 2E_{o\theta}E_{o\phi}\sin\Delta \end{bmatrix}. \tag{2.60}$$

By inspection we can find the phase matrix for scatterers much smaller than the wavelength:

$$\underline{\mathbf{p}}_R(\Theta) = \tfrac{3}{16\pi} \begin{bmatrix} 1+\cos^2\Theta & \cos^2\Theta - 1 & 0 & 0 \\ \cos^2\Theta - 1 & 1+\cos^2\Theta & 0 & 0 \\ 0 & 0 & 2\cos^2\Theta & 0 \\ 0 & 0 & 0 & 2\cos^2\Theta \end{bmatrix} \tfrac{1}{\mathrm{str}}\ . \tag{2.61}$$

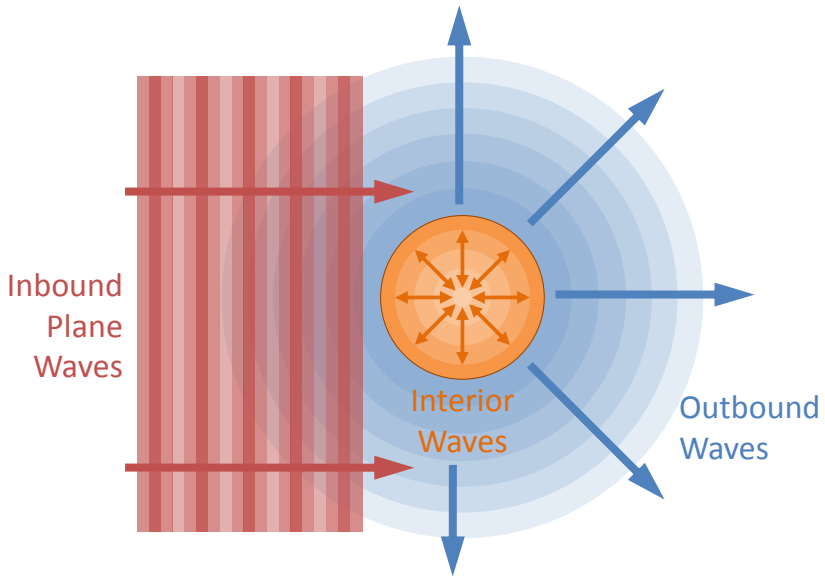

Figure 2.12: The incident plane wave and the scattered wave are superimposed to find the total external wave. This is used in conjunction with the interior wave and boundary conditions to solve the undetermined coefficients.

2.3.3 Scattering by Large Particles

The Rayleigh approximation does not apply to particles whose size is comparable to the wavelength. Larger particles are often approximated as homogeneous spheres and analyzed using a mathematical approach developed by Gustav Mie. Substances that exist as highly irregular shapes, like cirrus ice crystals which are often shaped like hexagonal rods or disks, are not approximated well using Mie scattering solution. Much more complicated analysis is required to accurately model their scattering processes. Mie scattering is used regularly to model the properties of sulphate aerosols, which are spherical liquid droplets on the order of a micron.

The Mie solution decomposes the incident plane wave in terms of spherical equations. The scattered and internal fields are also in written in terms of spherical equations with undetermined coefficients. The total external field is the superposition of the incident and scattered fields which is used alongside the internal field and the boundary conditions to solve for the coefficients. These fields are depicted schematically in Figure 2.12.

A solution is obtained by putting the incident plane wave in terms of a linear combination of the derivatives of orthogonal solutions to a scalar wave equation. These

scalar solutions are composed of spherical Bessel functions and Legendre polynomials. A brief outline of the derivation of a Mie scattering matrix follows to illustrate the principles used to obtain scattering matrices for systems that are more complicated than the Rayleigh case.

Following the solution as presented by *van de Hulst* (1962) we see the incident, internal, and scattered fields have functions of the form:

$$\underline{E} = \underline{M}_v + i\underline{N}_u \tag{2.62}$$

where

$$\begin{aligned} \underline{M}_\psi &= \nabla \times (\underline{r}\psi) \\ \underline{N}_\psi &= \tfrac{1}{mk}\nabla \times (\underline{M}_\psi) \end{aligned} \tag{2.63}$$

where m is the index of refraction, defined by $m^2 = -\frac{4\pi i \varrho}{\omega}$, ϱ is the conductivity of the particle, and ψ is a solution to the scalar wave equation. We assume the incident wave is traveling in the positive $\hat{z}$ direction initially and E_θ lies in the $\hat{x}$ direction. The solutions to the scalar wave equation, u and v, are defined differently for the incident and scattered waves. Specifically the incident wave has,

$$\begin{aligned} u_{inc} &= e^{i\omega t}\cos\phi \sum_{n=1}^{\infty}(-i)^n \frac{2n+1}{n(n+1)} P_n^1(\cos\theta) j_n(kr) \\ v_{inc} &= e^{i\omega t}\sin\phi \sum_{n=1}^{\infty}(-i)^n \frac{2n+1}{n(n+1)} P_n^1(\cos\theta) j_n(kr) \end{aligned} \tag{2.64}$$

where P_n^1 is a Legendre polynomial and j_n is the spherical Bessel function of the first kind. The scattered wave has the functions,

$$\begin{aligned} u_{\text{scat}} &= e^{i\omega t}\cos\phi \sum_{n=1}^{\infty} -a_n(-i)^n \frac{2n+1}{n(n+1)} P_n^1(\cos\theta) h_n^{(2)}(kr) \\ v_{\text{scat}} &= e^{i\omega t}\sin\phi \sum_{n=1}^{\infty} -b_n(-i)^n \frac{2n+1}{n(n+1)} P_n^1(\cos\theta) h_n^{(2)}(kr) \end{aligned} \tag{2.65}$$

where $h_n^{(2)}$ is a spherical Bessel function of the second kind. The internal field has the functions,

$$\begin{aligned} u_{int} &= e^{i\omega t}\cos\phi \sum_{n=1}^{\infty} mc_n(-i)^n \frac{2n+1}{n(n+1)} P_n^1(\cos\theta) j_n(kr) \\ v_{int} &= e^{i\omega t}\sin\phi \sum_{n=1}^{\infty} md_n(-i)^n \frac{2n+1}{n(n+1)} P_n^1(\cos\theta) j_n(kr) \end{aligned} . \tag{2.66}$$

The values a_n, b_n, c_n, and d_n are all undetermined coefficients. Following van de Hulst we know that using the boundary conditions at the surface of the sphere we can

eliminate c_n, and d_n and find,

$$\begin{aligned} a_n &= mk^2 r_s^2 \frac{j_n'(mkr_s)j_n(kr_s) - mj_n(mkr_s)j_n'(kr_s)}{j_n'(mkr_s)h_n^{(2)}(kr_s) - mj_n(mkr_s)h_n^{(2)'}(kr_s)} \\ b_n &= mk^2 r_s^2 \frac{mj_n'(mkr_s)j_n(kr_s) - j_n(mkr_s)j_n'(kr_s)}{mj_n'(mkr_s)h_n^{(2)}(kr_s) - j_n(mkr_s)h_n^{(2)'}(kr_s)} \end{aligned} \tag{2.67}$$

where r_s is the radius of the sphere.

At large distances from the scatterer the spherical Bessel functions of the second kind employed in the scalar solutions to the scattered field can be simplified using the approximation

$$h_n^{(2)}(kr) \sim \frac{i^{n+1}}{kr} e^{-ikr}. \tag{2.68}$$

This allows us to simplify the scalar solutions:

$$\begin{aligned} u_{\text{scat}} &= -\tfrac{i}{kr} e^{-ikr - i\omega t} \cos\phi \sum_{n=1}^{\infty} a_n \frac{2n+1}{n(n+1)} P_n^1(\cos\theta) \\ v_{\text{scat}} &= -\tfrac{i}{kr} e^{-ikr - i\omega t} \sin\phi \sum_{n=1}^{\infty} b_n \frac{2n+1}{n(n+1)} P_n^1(\cos\theta) \end{aligned} \tag{2.69}$$

Using these scalar solutions along with Equations 2.62 and 2.63 to find the electric field we find we can write:

$$\begin{aligned} E_{\text{scat}\theta} &= -\tfrac{i}{kr} e^{-ikr - i\omega t} \cos\phi S_2(\theta) \\ E_{\text{scat}\phi} &= -\tfrac{i}{kr} e^{-ikr - i\omega t} \sin\phi S_1(\theta) \end{aligned} \tag{2.70}$$

where

$$\begin{aligned} S_1(\theta) &= \sum_{n=1}^{\infty} \frac{2n+1}{n(n+1)} \left[a_n \frac{1}{\sin\theta} + b_n \frac{d}{d\theta} \right] P_n^1(\cos\theta) \\ S_2(\theta) &= \sum_{n=1}^{\infty} \frac{2n+1}{n(n+1)} \left[b_n \frac{1}{\sin\theta} + a_n \frac{d}{d\theta} \right] P_n^1(\cos\theta) \end{aligned} \tag{2.71}$$

are called the amplitude functions.

Van de Hulst also derives the extinction, scattering and absorption efficiencies using the amplitude functions and obtains,

$$\begin{aligned} Q_{\text{ext}} &= \tfrac{2}{(kr_s)^2} \sum_{n=1}^{\infty} (2n+1) \text{Re}\{a_n + b_n\} \\ Q_{\text{scat}} &= \tfrac{2}{(kr_s)^2} \sum_{n=1}^{\infty} (2n+1)(|a_n|^2 + |b_n|^2) \\ Q_{\text{abs}} &= Q_{\text{ext}} - Q_{\text{scat}} \end{aligned} \tag{2.72}$$

The cross sections are related to their respective efficiency by way of the equation,

$$\sigma = \pi r_s^2 Q \tag{2.73}$$

At this point it is possible to find the phase matrix for light scattered by a sphere based on this solution for the scattered field. As was shown for Rayleigh scattering one constructs Stokes vectors from the incident and scattered electric fields and solves for the transformation matrix that would transform the inbound field into the scattered field. Assuming that the scattered direction lies in the $\hat{x} - \hat{z}$ plane we know $\phi = 0$, and we obtain the equation given by *Hansen and Travis* (1974),

$$\underline{\mathbf{p}}'_M = \sigma_{\text{scat}} \frac{3}{8} \begin{bmatrix} \frac{1}{2}(S_1 S_1^* + S_2 S_2^*) & \frac{1}{2}(S_1 S_1^* - S_2 S_2^*) & 0 & 0 \\ \frac{1}{2}(S_1 S_1^* - S_2 S_2^*) & \frac{1}{2}(S_1 S_1^* + S_2 S_2^*) & 0 & 0 \\ 0 & 0 & \frac{1}{2}(S_1 S_2^* + S_2 S_1^*) & \frac{i}{2}(S_1 S_2^* - S_2 S_1^*) \\ 0 & 0 & \frac{-i}{2}(S_1 S_2^* - S_2 S_1^*) & \frac{1}{2}(S_1 S_2^* + S_2 S_1^*) \end{bmatrix} \tag{2.74}$$

This result gives the phase matrix for a scatterer with a single radius. As mentioned in Section 1.1.1 aerosols exist naturally at a range of sizes. Once a function is found that accurately describes the size distribution the bulk phase matrix for the atmosphere can be found by performing a weighted average over the particle radius,

$$\underline{\mathbf{p}}_M = \frac{\int_0^\infty \underline{\mathbf{p}}'_M f(r_s) \mathrm{d}r_s}{\int_0^\infty f(r_s) \mathrm{d}r_s} \tag{2.75}$$

2.3.4 The Scattering Plane

Because it simplifies the derivations in both cases outlined above, and for more complex shapes, we required the E_θ component to be measured in a plane that contains both the incident and outbound directions, $\hat{\Omega}_1$ and $\hat{\Omega}_2$ respectively. This plane is called the scattering plane and it is depicted in Figure 2.13.

The $\hat{\theta}_1$ and $\hat{\phi}_2$ directions may be in any direction with respect to the scattering plane initially. To apply the phase matrices to these cases we must apply a rotation operation to the electric field components:

$$\underline{\tilde{E}}_{\text{rot}} = \begin{bmatrix} \cos\eta & \sin\eta \\ -\sin\eta & \cos\eta \end{bmatrix} \underline{\tilde{E}} \tag{2.76}$$

where η is measured as the angle between $\hat{\theta}_1$ and the scattering plane. This results in

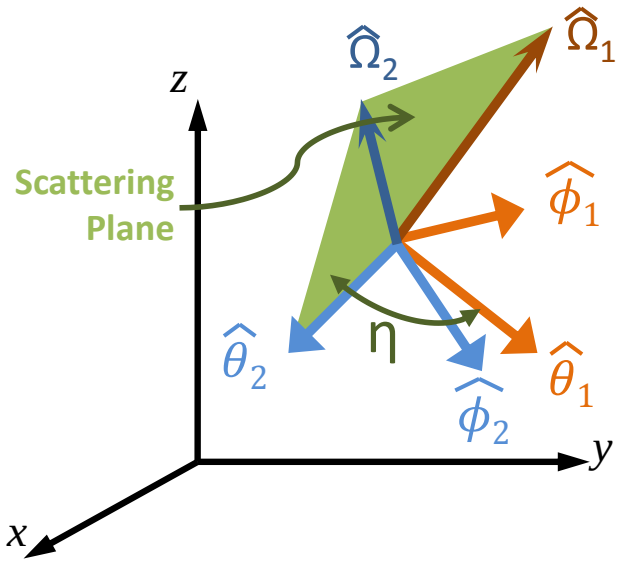

Figure 2.13: Depiction of the scattering plane and rotation angle η

a rotated Stokes vector of the form:

$$\underline{I}_{\text{rot}} = \frac{1}{2}\sqrt{\frac{\epsilon}{\mu}} \begin{bmatrix} E_{o\theta}^2 + E_{o\phi}^2 \\ \cos 2\eta(E_{o\theta}^2 - E_{o\phi}^2) + \sin 2\eta(2E_{o\theta}E_{o\phi}\cos\Delta) \\ \cos 2\eta(-2E_{o\theta}E_{o\phi}\cos\Delta) - \sin 2\eta(E_{o\theta}^2 - E_{o\phi}^2) \\ 2E_{o\theta}E_{o\phi}\sin\Delta \end{bmatrix}. \tag{2.77}$$

From this we can find the rotation matrix for Stokes vectors,

$$\underline{\mathbf{R}}(\eta) = \begin{bmatrix} 1 & 0 & 0 & 0 \\ 0 & \cos 2\eta & \sin 2\eta & 0 \\ 0 & -\sin 2\eta & \cos 2\eta & 0 \\ 0 & 0 & 0 & 1 \end{bmatrix}. \tag{2.78}$$

It will be useful later to state explicitly that the rotation matrix is a function of the incident and outbound directions as well as the direction $\hat{\theta}_1$,

$$\underline{\mathbf{R}}(\eta) = \underline{\mathbf{R}}(\hat{\Omega}_1, \hat{\theta}_1, \hat{\Omega}_2). \tag{2.79}$$

2.4 Polarized Equations of Radiative Transfer

Using Stokes vectors, phase matrices, and rotation matrices it is now possible to re-write the equations of radiative transfer in a polarized form. The coordinates for a

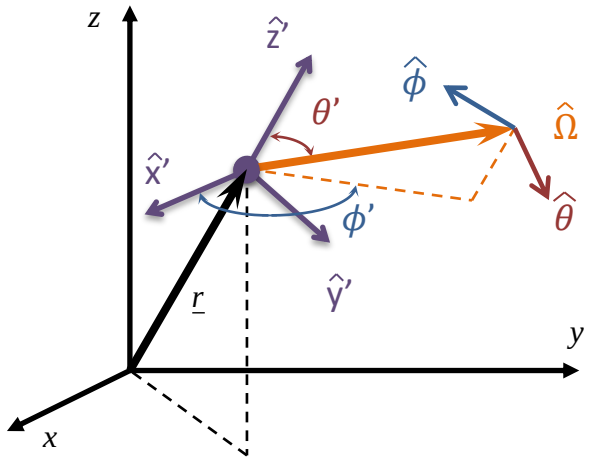

Figure 2.14: Specifying the polarized radiant field requires three spacial coordinates to define the position, two coordinates for the directional distribution, and coordinates defining the orientation of the polarization plane

polarized radiant field, depicted in Figure 2.14, require the definition of the plane of polarization (the $\hat{\theta} - \hat{\phi}$ plane) to which the Stokes vector may be referenced. Rather than keep track of both $\hat{\theta}$ and $\hat{\phi}$ we use the fact that $\hat{\Omega}$, $\hat{\theta}$, and $\hat{\phi}$ are all mutually perpendicular and only concern ourselves with $\hat{\theta}$. With this in mind we say the radiant field is defined by $\underline{I}(\underline{r}_o, \hat{\Omega}, \hat{\theta})$. Following the same reasoning as Section 2.1.1 we can arrive at analogous equations for polarized radiative transfer.

The atmospheric single scatter contribution to the radiance observed is

$$\underline{I}_{a1}(s_0, \hat{\Omega}, \hat{\theta}) = \int_{s_0}^{s_1} \chi(s) e^{-\tau(s,0)} \underline{J}_{a1}(s, \hat{\Omega}, \hat{\theta}) \mathrm{d}s \tag{2.80}$$

Because the Stokes vector from the sun, $\underline{F}_s$, is assumed to be randomly polarized there is no reason to rotate the Stokes vector before applying the scattering phase matrix. After applying the scattering operation, however, the resulting Stokes vector must be rotated to correspond to $\hat{\theta}$ and therefore the single scatter source term is

$$\underline{J}_{a1}(s, \hat{\Omega}, \hat{\theta}) = \frac{\chi_{\text{scat}}(s)}{\chi(s)} e^{-\tau(\text{sun},s)} \underline{\mathbf{R}}(\hat{\Omega}_s, \hat{\theta}_s, \hat{\Omega}) \underline{\mathbf{p}}(s, \hat{\Omega}, \hat{\Omega}_s) \underline{F}_s. \tag{2.81}$$

The ground's single scatter contribution to the radiance may be written as

$$\underline{I}_{g1}(s_0, \hat{\Omega}, \hat{\theta}) = e^{-\tau(\text{sun},s_g)} e^{-\tau(s_g,s_0)} \underline{\mathbf{R}}(\hat{\Omega}_s, \hat{\theta}_s, \hat{\Omega}) \underline{\mathbf{p}}(s_g, \hat{\Omega}, \hat{\Omega}_s) \underline{F}_s. \tag{2.82}$$

The polarized second order atmospheric source term is found using the same steps we used to find Equation 2.23. So we substitute Equations 2.80 and 2.82, the incoming

radiance produced by the first order of scattering, into Equation 2.12 to find,

$$\underline{J}_{a2}(s,\hat{\Omega},\hat{\theta}) = \frac{\chi_{\text{scat}}(s)}{\chi(s)} \int_{4\pi} \underline{\mathbf{R}}(\hat{\Omega},\hat{\theta},\hat{\Omega}')\underline{\mathbf{p}}(s,\hat{\Omega},\hat{\Omega}')\underline{\mathbf{R}}(\hat{\Omega}',\hat{\theta}',\hat{\Omega}) \left[\underline{I}_{a1}(s',\hat{\theta}) + \underline{I}_{g1}(s',\hat{\theta})\right] \mathrm{d}\Omega'. \tag{2.83}$$

The integral over a unit sphere acts to collect this incoming radiance and scatter it in the outward direction, $\hat{\Omega}$. The second order radiance from atmospheric scattering is therefore

$$\underline{I}_{a2}(s_0,\hat{\Omega},\hat{\theta}) = \int_{s_0}^{s_1} \chi(s) e^{-\tau(s)} \underline{J}_{a2}(s,\hat{\Omega},\hat{\theta}) \mathrm{d}s. \tag{2.84}$$

In this fashion source functions for each order of scattering are found using the previous order. So the equations for the n^{th} order atmospheric scattering can be generalized to

$$\underline{J}_{an}(s,\hat{\Omega},\hat{\theta}) = \frac{\chi_{\text{scat}}(s)}{\chi(s)} \int_{4\pi} \underline{\mathbf{R}}(\hat{\Omega},\hat{\theta},\hat{\Omega}')\underline{\mathbf{p}}(s,\hat{\Omega},\hat{\Omega}')\underline{\mathbf{R}}(\hat{\Omega}',\hat{\theta}',\hat{\Omega}) \left[\underline{I}_{a(n-1)}(s,\hat{\Omega}',\hat{\theta}) + \underline{I}_{g(n-1)}(s,\hat{\Omega}',\hat{\theta})\right] \mathrm{d}\Omega', \tag{2.85}$$

and

$$\underline{I}_{an}(s_0,\hat{\Omega},\hat{\theta}) = \int_{s_0}^{s_1} \chi(s) e^{-\tau(s)} \underline{J}_{an}(s,\hat{\Omega},\hat{\theta}) \mathrm{d}s. \tag{2.86}$$

By integrating over 2π we gather all the inbound first order light from above and scatter it outwards into the direction $\hat{\Omega}$ to obtain the second order,

$$\underline{I}_{g2}(s_0,\hat{\Omega},\hat{\theta}) = e^{-\tau(s_g,s_0)} \int_{2\pi} \underline{\mathbf{R}}(\hat{\Omega},\hat{\theta},\hat{\Omega}')\underline{\mathbf{p}}(s,\hat{\Omega},\hat{\Omega}')\underline{\mathbf{R}}(\hat{\Omega}',\hat{\theta}',\hat{\Omega})\underline{I}_{a1}(s_g,\hat{\Omega}',\hat{\theta}) \mathrm{d}\Omega'. \tag{2.87}$$

As with atmospheric scattering this is generalized to the n^{th} order and we obtain the equation

$$\underline{I}_{gn}(s,\hat{\Omega},\hat{\theta}) = e^{-\tau(s_g,s)} \int_{2\pi} \underline{\mathbf{R}}(\hat{\Omega},\hat{\theta},\hat{\Omega}')\underline{\mathbf{p}}(s,\hat{\Omega},\hat{\Omega}')\underline{\mathbf{R}}(\hat{\Omega}',\hat{\theta}',\hat{\Omega})\underline{I}_{a(n-1)}(s_g,\hat{\Omega}',\hat{\theta}) \mathrm{d}\Omega'. \tag{2.88}$$

The total radiance that reaches an observer can be found by summing the contributions from all orders,

$$\begin{aligned} \underline{I}(s_0,\hat{\Omega},\hat{\theta}) = \int_{s_0}^{s_1} \chi(s) e^{-\tau(s)} & \left[\underline{J}_{a1}(s,\hat{\Omega},\hat{\theta}) + \underline{J}_{a2}(s,\hat{\Omega},\hat{\theta}) + \sum_{n=3}^{\infty} \underline{J}_{an}(s,\hat{\Omega},\hat{\theta})\right] \mathrm{d}s \\ & + \left[\underline{I}_{g1}(s_0,\hat{\Omega},\hat{\theta}) + \underline{I}_{g2}(s_0,\hat{\Omega},\hat{\theta}) + \sum_{n=3}^{\infty} \underline{I}_{gn}(s_0,\hat{\Omega},\hat{\theta})\right] \end{aligned}. \tag{2.89}$$

2.5 Organization of the Vector SASKTRAN

The polarized version of SASKTRAN was designed such that the model could be easily switched from the original non-polarized calculations to the polarized versions without a recompilation of the model's source code. The easy switch is desirable because

situations sensitive to polarization would be modeled using the fully polarized calculations while other situations could use the non-polarized calculations, which necessarily require less time and computer resources than the polarized version.

To achieve this goal the main SASKTRAN components described in Section 2.2.1 would still serve the same purposes and their interactions would remain largely unchanged. However the inner workings of these components as well as their surrounding infrastructure must be augmented to create, use, and store the additional polarized information. The vector SASKTRAN model can perform polarized or non-polarized calculations using a single compiled software library. The polarized radiative transfer equations used by the LOSs, DSPs, Profiles, and OLOSs , which use summations to approximate the integrals in the equations in Section 2.4, are presented here along with schematics, and an outline of the changes required to allow SASKTRAN to be polarized.

2.5.1 The Polarized Discrete Radiative Transfer Equations

In Section 2.4 it was explained that we must use the position $\underline{r}$, the propagation direction $\hat{\Omega}$, and the reference direction $\hat{\theta}$. In the vector SASKTRAN model we employ another convention to reduce the coordinates required. Rather than store the direction $\hat{\theta}$ it is always perpendicular to $\hat{\Omega}$ and lies in the solar plane. The solar plane is a plane that contains both the propagation direction $\hat{\Omega}$ and the vector pointing to the sun as illustrated in Figure 2.15. Prior to each scattering event the reference direction must be rotated from the solar plane to the scattering plane, and after each scattering event it must be rotated from the scattering plane into the new solar plane. Rotations to and from some plane are required whether or not this convention is used, and this convention has the benefit of reducing the information stored for each ray by one set of coordinates to merely $\underline{r}$ and $\hat{\Omega}$.

The Stokes Vector representing unscattered light from the sun at the i^{th} position is

$$\underline{F}_i = F_s e^{-\tau(sun,s_i)} \begin{bmatrix} 1 \\ 0 \\ 0 \\ 0 \end{bmatrix}. \tag{2.90}$$

The Q, U, and V elements of this Stokes Vector are zero because only scattering processes change the polarization state of light in the atmosphere and prior to entering

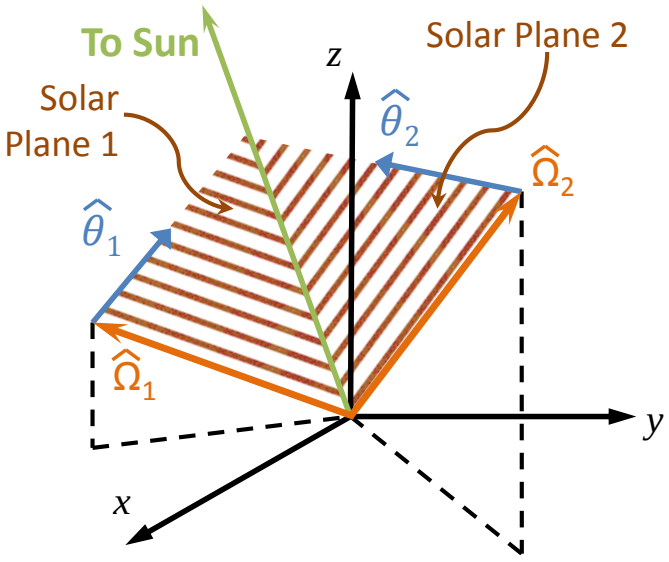

Figure 2.15: The polarization reference direction, $\hat{\theta}$, is always left in a plane that contains both the direction of propagation and the solar vector.

the atmosphere radiation from the sun is completely randomly polarized. Therefore $\underline{F}_i$ remains randomly polarized and the irradiance is only attenuated as it passes from the top of the atmosphere to the i^{th} position.

The first order Stokes Vector due to atmospheric scattering found at the j^{th} point along line of sight is

$$\underline{I}_{a1j}(\hat{\Omega}) = \sum_i f_{a1i} \underline{\mathbf{M}}_{is} \underline{F}_i \tag{2.91}$$

where the factor in the summation is $f_{a1i} = \chi_{\text{scat}i} e^{-\tau_i} \Delta s_i$. In the vector SASKTRAN the rotation and phase matrix at the i^{th} point along the line of sight, $\underline{\mathbf{M}}_{is} = \underline{\mathbf{R}}(\eta_i)\underline{\mathbf{p}}_i(\hat{\Omega}, \hat{\Omega}_{\text{sun}})$, and the summation factor are stored separately.

The ground's contribution to the singly scattered radiance at the j^{th} point along the line of sight is

$$\underline{I}_{g1j}(\hat{\Omega}) = f_{g1} \underline{\mathbf{D}} \underline{F}_g. \tag{2.92}$$

Scattering from the ground is assumed to be Lambertian and depolarizing. Therefore the factor in this summation is $f_{g1} = \frac{a}{\pi} \cos(\theta_{\text{sza}}) e^{-\tau(s_g, s_j)}$ and the depolarization matrix

can be written as

$$\underline{\mathbf{D}} = \begin{bmatrix} 1 & 0 & 0 & 0 \\ 0 & 0 & 0 & 0 \\ 0 & 0 & 0 & 0 \\ 0 & 0 & 0 & 0 \end{bmatrix}. \tag{2.93}$$

The depolarization matrix, $\underline{\mathbf{D}}$, is redundant here because the Stokes Vector $\underline{F}_g$ would be randomly polarized since the light has yet to undergo any scattering. So the equation may be rewritten

$$\underline{I}_{g1j}(\hat{\Omega}) = f_{g1}\underline{F}_g. \tag{2.94}$$

The source function based equivalent of the Stokes Vector in the k^{th} direction at the j^{th} point for the n^{th} order of scattering is

$$\underline{J}_{anj}(\hat{\Omega}_k) = \sum_i \underline{\boldsymbol{f}}_{Jaik} \left[\underline{I}_{a(n-1)j}(\hat{\Omega}_i) + \underline{I}_{g(n-1)j}(\hat{\Omega}_i) \right] \tag{2.95}$$

where the factor in this summation is the matrix

$$\underline{\boldsymbol{f}}_{Jaik} = \chi_{\mathrm{scat}j}\Delta\Omega_i \underline{\mathbf{R}}(\eta_{2ik})\underline{\mathbf{p}}_j(\hat{\Omega}_k, \hat{\Omega}_i)\underline{\mathbf{R}}(\eta_{1ik}). \tag{2.96}$$

This matrix contains a rotation from a reference direction by an angle η_{1ik} into the scattering plane, the scattering matrix, and a rotation from the scattering plane into some desired reference plane by the angle η_{2ik}. Figure 2.16 shows schematically how the information flows within the DSPs to compute these Stokes Vectors.

The atmospheric contribution to the n^{th} order Stokes Vector is found from the source function using the equation

$$\underline{I}_{anl} = \sum_i f_{Iai}\underline{J}_{ani}(\hat{\Omega}_i) \tag{2.97}$$

where the scalar factor in this summation is

$$f_{Iai} = e^{-\tau_i}\Delta s_i \zeta_i \xi_i. \tag{2.98}$$

The variables ζ_i and ξ_i are weighted values for different source functions and are used to interpolate to the desired position and direction respectively.

The ground contribution to the n^{th} order Stokes Vector is found from the previous order of Stokes Vectors,

$$\underline{I}_{gnl} = \sum_i f_{Igi}\underline{\mathbf{D}}\underline{I}_{a(n-1)g}(\hat{\Omega}_i). \tag{2.99}$$

The factor in the summation assumes Lambertian scattering and may be written as $f_{Igi} = \frac{a}{\pi} e^{-\tau(s_g, s_l)} \cos(\theta_i) \Delta\Omega_i$. Again the matrix $\underline{\mathbf{D}}$ is used to depolarize ground scattered light. Figure 2.17 illustrates how information flows within and between different components of the vector SASKTRAN to find the Stokes Vectors.

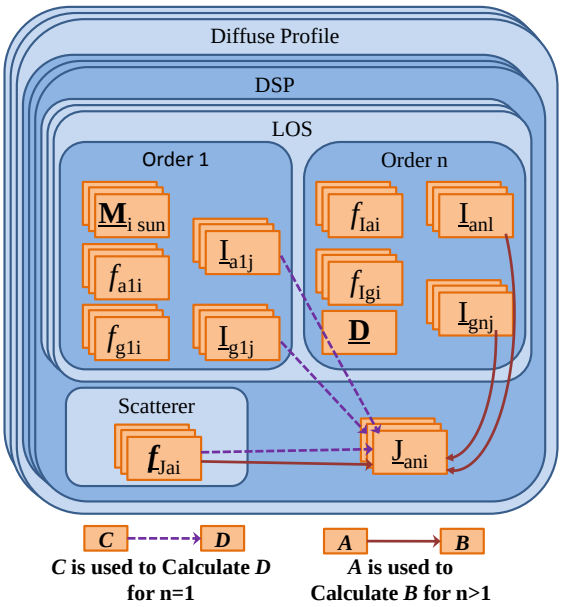

Figure 2.16: A schematic of information flow as each DSP finds a set of outbound source functions J_{ani} from the $n-1$ radiance terms produced by the DSP's LOSs.

2.5.2 Changes to Polarize SASKTRAN

Many of the classes that make up the major components of SASKTRAN and serve as their infrastructure required changes of some type to allow for polarized calculations. There are several design goals that should be adhered to while implementing the polarized model. Any changes should leave the non-polarized components and calculations as unchanged as possible and generate little to no impact on memory and performance; so the polarized components must be fit into SASKTRAN in a way that does not affect non-polarized components. At the same time the polarized model should be able to perform efficiently as well, which would be easier to achieve by making larger changes to SASKTRAN's design. As with any software design it is necessary to balance these principles and others that are somewhat conflicting. The design decisions and the resulting polarized components are described in Section 3.1.

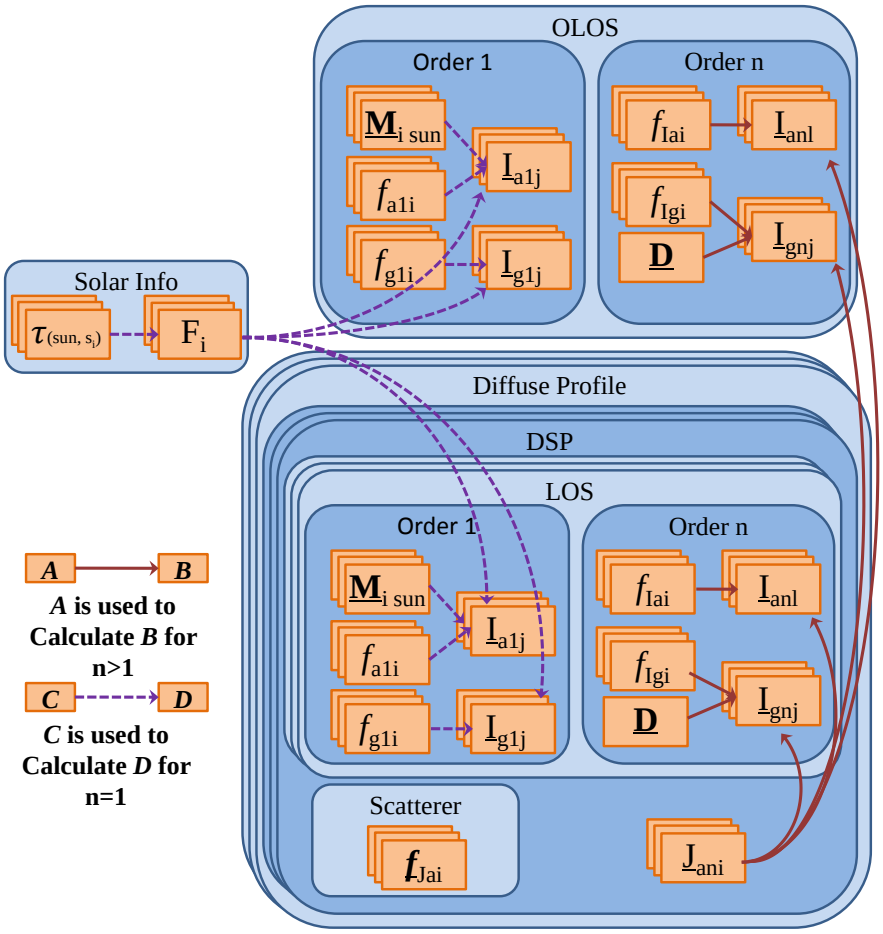

Figure 2.17: A schematic of information flow as each LOS and the OLOS finds its ground at atmospheric radiance from the solar irradiance for the first order of scattering, and from the DSP source functions for higher orders.

The LOSs and OLOS rely on links from these components to the terms that are stored in the solar information tables and the DSPs. They also rely on weighting factors that are entirely scalar in the unmodified SASKTRAN but must be matrices in some cases in the polarized calculations. Creating a system that allows for minimal changes from polarized to non-polarized calculations will lead to the creation of inheritance relationships between new and existing C++ classes.

During polarized calculations it becomes necessary to store Stokes Vectors and phase matrices in place of scalar values. This does require a significantly larger amount of memory than non-polarized calculations. It is therefore crucial that this memory is not allocated while performing non-polarized calculations. It is also important to

consider how vectors and matrices will be accessed both for efficiency reasons and for ease of use. Additionally it is important to consider how to maintain a constant interface between components for both polarized and non-polarized calculations while passing vectors and phase matrices instead of scalar values.

In the scalar SASKTRAN each DSP computes the current order's source function values at predetermined directions based on incoming light from the previous order. The scalar source function in any direction within a given spherical shell is interpolated from these predetermined directions. The source function at any point is a relatively smooth field that allows for interpolation (*Bourassa*, 2007). In the vector SASKTRAN this process must be evaluated with consideration for the source function Stokes Vector $\underline{J}$. Several simple interpolation schemes that fit in SASKTRAN's architecture were evaluated in Section 3.2 below.

Under the reference plane convention described in Section 2.5.1 non-parallel outbound rays have different reference planes. Because of this it was suspected that problems would arise while interpolating the source function Stokes Vector since these rays are, by definition, non-parallel. These concerns were validated while evaluating the source function interpolation schemes and a solution to this issue is described and the results examined in Section 3.3.

Chapter 3

Implementation of the Vector SASKTRAN

The preceding chapter was composed to provide an understanding of the goal of this thesis and how it is achieved. It began by providing the theory and technical information relevant to polarized radiative transfer theory and the organization of the SASKTRAN model. Section 2.5.2 described the specific changes to SASKTRAN that would be necessary to produce a polarized version of SASKTRAN. From this basis SASKTRAN was altered and expanded upon to achieve a polarized RTM and Chapter 3 is dedicated to describing how these changes were implemented.

The first section outlines the polarized components that were added to SASKTRAN; it explains how they function and how they were structured to easily change from polarized to non-polarized calculations. The subsequent section discusses alternative methods for performing directional interpolation of the source functions at the DSPs and evaluates their success. The final section of this chapter describes the solution to a problem that occurs when interpolating between source function Stokes Vectors that have different reference directions and discusses the results.

3.1 Polarized Classes

Within SASKTRAN there are many classes that make up the Lines of Sight, the Diffuse Scattering Points, the Diffuse Profiles, and the Observer Lines of Sight. There are also classes used to supply information to these components, others used to operate as a communication infrastructure between them and there are some that serve as

storage. The changes that were implemented to allow for polarized radiative transfer were designed with the intent to disrupt as little of the existing model as possible and to maintain the ability to perform fast calculations on desktop computers. This required small changes throughout a number of classes but several of the most significant changes to SASKTRAN's structure are outlined here.

The links shown in Figure 2.8 from source function terms, solar irradiance terms, and weighting terms to the irradiances that are calculated at the end of the LOSs and OLOS are all of a similar nature. In SASKTRAN these links are all maintained and used for calculations by the same class, named JValueTable. Each LOS and OLOS has access to a JValueTable to link the solar information used for the first order of scattering, and another JValueTable to link to the many different source terms used for higher orders as shown schematically in Figure 3.1. These objects do not contain source function values themselves but only contain links to the values. This is because all the LOSs relying on the source function values immediately have access to them as they are calculated for each order within the DSPs. This saves going through each JValueTable in each LOS and updating the values for every order of scattering.

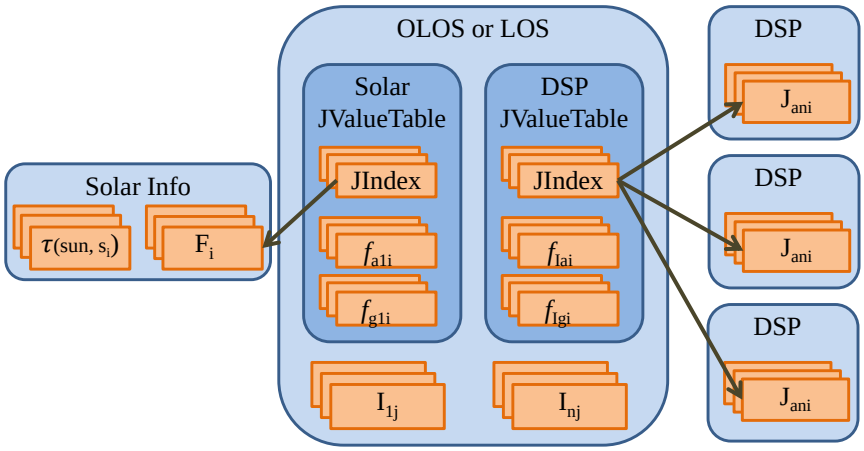

Figure 3.1: A schematic for the links in JValueTables. Each non-polarized LOS or OLOS has two JValueTables, one links to solar irradiance and the other to DSP source functions. They calculate the radiance along a line of sight.

Using JValueTables to link to these different types of terms reduces the size of the code base in SASKTRAN, which makes it easier to store, maintain, and improve upon. As shown in Figure 2.17 while SASKTRAN performs polarized calculations the JValueTables cannot simply use scalar weighting values. In the first order the table

will need to store scattering matrices while linking to scalar values. In higher orders the tables may still store scalar summation factors, but they will need to link to vector source functions. To allow SASKTRAN to provide tables for these different situations an abstract base class was created, called JValueTableBase, such that JValueTable inherits from it. Two more classes, JValueTablePhaseMatrix and JValueTableStokes, also inherit from the base class as shown in Figure 3.2. This forces the classes to have common features in their interface that allows them to be swapped in and out of the LOS or OLOS as the need arises.

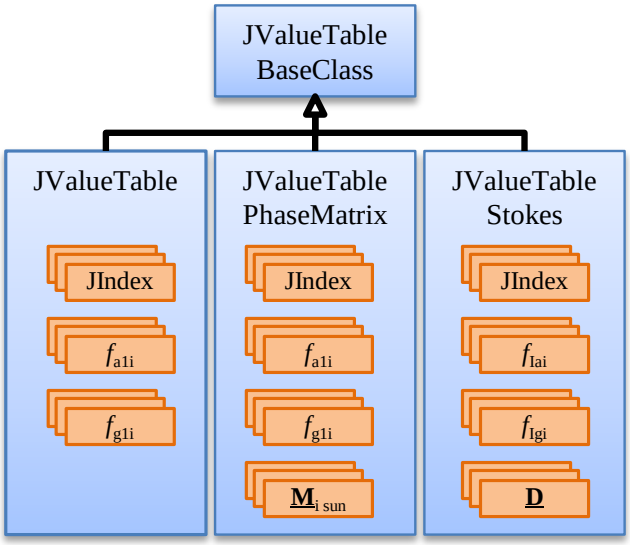

Figure 3.2: This inheritance organization forces the JValueTables to have identical features in their interface, even though their inner workings are different.

Each of these tables required a unique set of functions for connecting the links as well as setting summation factors and, in the case of JValueTablePhaseMatrix, the phase matrix itself. The links themselves are held in objects of the class JIndex as shown in Figures 3.1 and 3.3. These links with the solar information table and with the DSP are established while selecting outbound source functions from which to interpolate, which is described in detail in Section 3.2. As explained in detail in Section 3.3 while this is taking place there is an additional source function Stokes Vector rotation angle that must be determined. The JIndex objects are created in this phase, and used later when this rotation needs to take place. Because of this the JIndex class was augmented such that during this interpolation phase the rotation angle is stored. This made it possible to recover this information later and pass it to where it is required

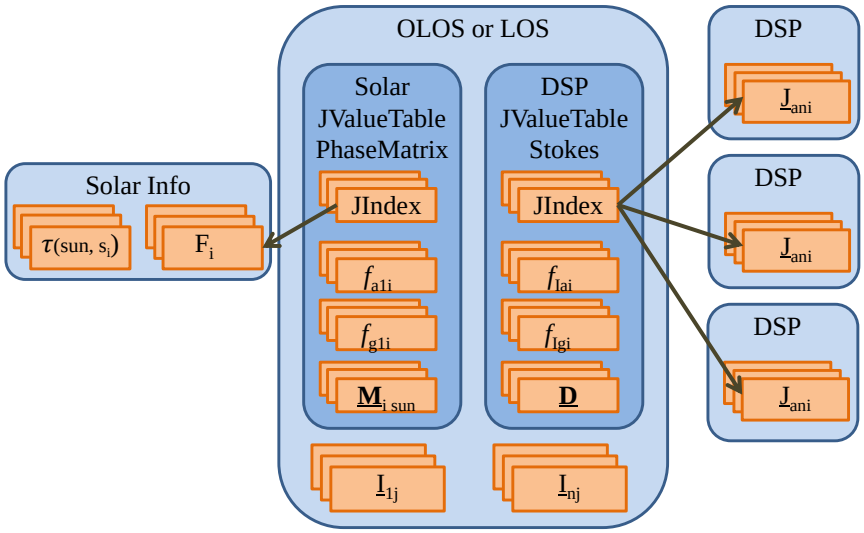

Figure 3.3: Each polarized LOS or OLOS has a JValueTablePhaseMatrix to link to solar irradiance and a JValueTableStokes to link to DSP source functions. They calculate the radiance along a line of sight.

with minimal alterations to SASKTRAN's structure.

Changes were required within the Diffuse Scattering Points and other infrastructure classes as well. Each DSP contains a Scatterer object and a set of source function values. In the original SASKTRAN these are all scalar values that were stored in arrays, which had to be replaced by phase matrices and Stokes Vectors. Several options for storing these non-scalar values were considered.

It is possible to create additional arrays for the polarized parameters that make up the air scattered Stokes Vector source function, the J_{Qani}, J_{Uani}, and J_{Vani} components of the i^{th} vector, as well as separate arrays for the additional phase matrix elements. Dealing with these separate storage vectors quickly becomes clumsy however, especially when passing the information from one SASKTRAN component to another. Instead of passing a single link the components must now pass four. This would necessitate separate interfaces for polarized and non-polarized processing, which is contrary to the design goals.

The second option is to create dedicated classes for storing each individual Stokes Vector and a phase matrix. This method makes things much less clumsy, both while performing radiative transfer calculations and while passing information from one place to the next. The result would be appear smoother but it would still require changing how information is passed and shared between components. It would also require more

memory to store these dedicated classes, and slow down the processes that access the information.

The solution that was implemented uses larger arrays for the polarized calculations and indexes the information differently, as illustrated in Figure 3.4. This method allows the SASKTRAN components to continue to pass information using a single link with the knowledge that it links to four or sixteen consecutive elements that make up either a Stokes Vector or a phase matrix respectively. Retaining the ability to pass a single link means that the interfaces between SASKTRAN components will be uniform for polarized and non-polarized calculations. It also uses less memory and time than creating dedicated storage classes.

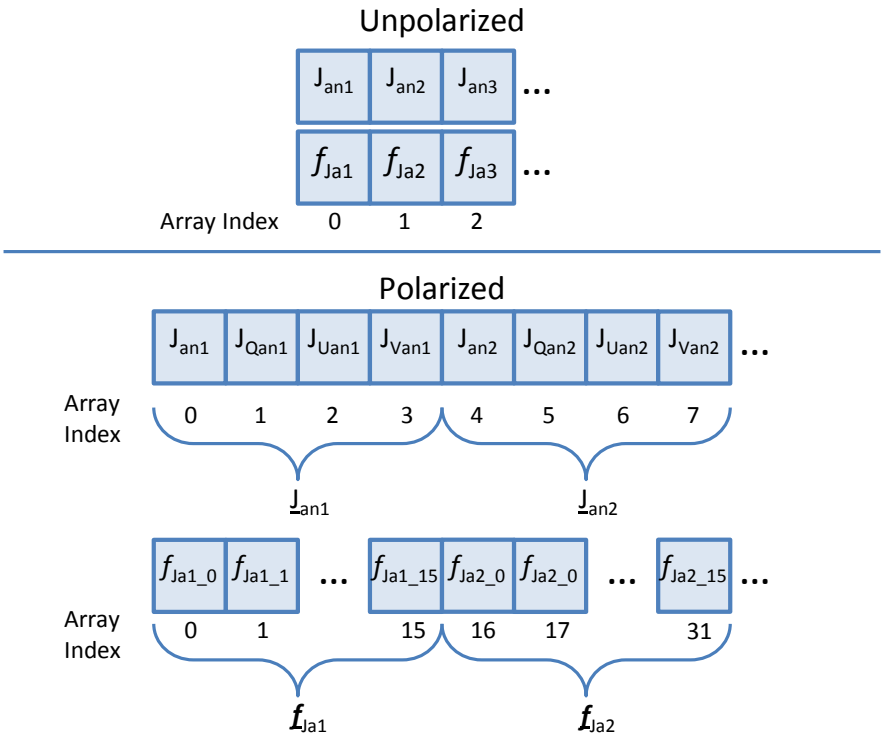

Figure 3.4: Stokes Vector and phase matrix values are stored with each element in sequence in arrays.

3.2 Interpolating Diffuse Source Terms

The Diffuse Scattering Points have precalculated source function values at set outbound directions for the application of Equation 2.97 or 2.99. It is desirable to obtain equal spacing of these precalculated outbound source function values over all directions.

Solutions to the Thomson Problem, named after J.J. Thomson for his investigations in the minimum energy distribution of electrons on a sphere (*Altschuler et al.*, 1997), provides points over an entire sphere that are as evenly distributed as possible. SASKTRAN uses previously determined solutions to this problem as sets of outbound source function directions, which are called minimum energy spheres.

Although SASKTRAN defaults to using minimum energy spheres the users of the model can specify different resolutions for the minimum energy spheres or even entirely different distributions. Therefore the outbound directions could be distributed a variety of ways so it is best to treat the interpolation as if the data points are randomly scattered. A variety of methods have been developed for interpolating from scattered data points. Interpolations schemes where the weighting factor of Equation 2.98, ξ_i, may be determined from geometry alone prior to knowing the source function values must be used because SASKTRAN precalculates these factors. The interpolation equations must be simple enough to be quickly computed and reliable for varying point distributions. It also must be possible to achieve good interpolation with as few points as possible, increasing speed and reducing the memory required to form links and store weighting values. Two methods proposed by *Shepard* (1968) were explored. The first is a general distance weighted method, here referred to as the Shepard method, and another includes directional information, referred to as the Modified Shepard method. A method of linear interpolation on a plane formed between three data points was also examined.

Shepard proposed using a weighted average based on the inverse squared distance from each of the data points to the point of interest and a distance parameter, r'. He further suggested that for large data sets it would be best to limit the weighted average to the data points to those near the point of interest. Shepard recommends using 4 to 10 points in the interpolation. We will call each data point $\underline{D}_j$ and the point to which we are interpolating will be $\underline{A}$. We will define d_j to be the arc length on the unit sphere such that $d_j = \arccos\left(\underline{D}_j \cdot \underline{A}\right)$. If we have a set of N points then when interpolating to $\underline{A}$ we order the points such that $d_1 < d_2 < ... < d_n < ... < d_N$ and only use the first n points. In this case Shepard defines $r' = d_{n+1}$ and we may write

$$s_j = \begin{cases} \frac{1}{d_j} & \text{if } 0 < d_j \leq \frac{r'}{3} \\ \frac{27}{4r'}\left(\frac{d_j}{r'} - 1\right)^2 & \text{if } \frac{r'}{3} < d_j \leq r' \\ 0 & \text{if } r' < d_j \end{cases} \tag{3.1}$$

and

$$\underline{J} = \begin{cases} \dfrac{\sum_{j=1}^{n} s_j^2 \underline{J}_j}{\sum_{j=1}^{n} s_j^2} & \text{if } d_j \neq 0 \text{ for all } j \\ \\ \underline{J}_j & \text{if } d_j = 0 \text{ for any } j \end{cases} \tag{3.2}$$

In the form used to calculate the i^{th} summation factor found in Equation 2.98 for the numerical integration of the source terms along a line of sight we write

$$\xi_i' = \begin{cases} \dfrac{s_i^2}{\sum_{j=1}^{n} s_j^2} & \text{if } d_i \neq 0 \text{ for all } i \\ \\ 1 & \text{if } d_i = 0 \end{cases} . \tag{3.3}$$

The second weighted average scheme proposed by Shepard is an extension of the first that includes directional information. This method is based on the idea that closer points can screen out the influence of farther points along the same direction. We define a unit vector $\hat{d}_j$ as a vector that is tangent to the unit sphere at $\underline{A}$ and points such that its projection on the sphere is the arc that connects $\underline{A}$ to $\underline{D}_j$, depicted in Figure 3.5. If we have two points $\underline{D}_j$ and $\underline{D}_k$ and we know that $d_j < d_k$ and $\hat{d}_j = \hat{d}_k$ then intuitively the value at $\underline{D}_k$ would have less effect on the interpolant than if $\hat{d}_j = -\hat{d}_k$. When $\hat{d}_j$ and $\hat{d}_k$ are in line the value at $\underline{D}_j$ screens the effects of the value at $\underline{D}_k$. To simulate this effect Shepard defines another parameter

$$t_k = \frac{\sum_{j=0}^{n} s_j \left[1 - \hat{d}_j \cdot \hat{d}_k\right]}{\sum_{j=0}^{n} s_j} \tag{3.4}$$

and from this Shepard finds

$$\underline{J} = \begin{cases} \dfrac{\sum_{j=1}^{n} s_j^2 (1 + t_i) \underline{J}_j}{\sum_{j=1}^{n} s_j^2 (1 + t_i)} & \text{if } d_j \neq 0 \text{ for all } j \\ \\ \underline{J}_j & \text{if } d_j = 0 \text{ for any } j \end{cases} \tag{3.5}$$

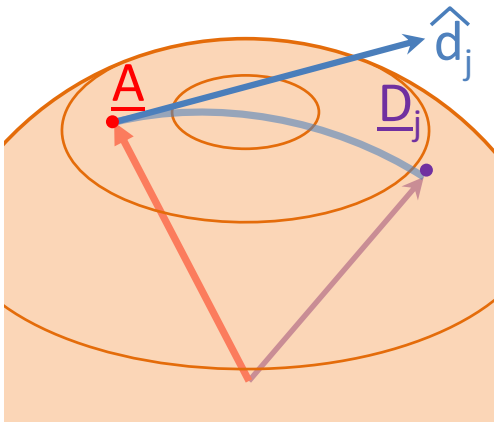

Figure 3.5: The unit vector is tangent to the sphere at the point of interest and makes an arc to the data point.

So we can find the final weighting factor for this modified Shepard method to be

$$\xi_i'' = \begin{cases} \dfrac{s_i^2(1+t_i)}{\sum_{j=1}^{n} s_j^2(1+t_j)} & \text{if } d_i \neq 0 \text{ for all } i \\ 1 & \text{if } d_i = 0 \end{cases} . \tag{3.6}$$

A linear interpolation scheme is another option for finding the source function from a DSP in the direction of a Line of Sight. Three of the nearest directions that surround the LOS direction are selected to form the vertices of a triangle. We will call these vertices $\underline{D}_1$, $\underline{D}_2$, and $\underline{D}_3$. The vector defining the direction of the LOS will be called $\underline{A}$. The vectors connecting these vertices are $\underline{d}_{12} = \underline{D}_2 - \underline{D}_1$ and $\underline{d}_{13} = \underline{D}_3 - \underline{D}_1$ as shown in Figure 3.6. If we create parameters t and u that range from 0 to 1 then we can define the vector from $\underline{D}_1$ to $\underline{A}$ as

$$\underline{d}_1 = t \cdot \underline{d}_{12} + u \cdot \underline{d}_{12}. \tag{3.7}$$

Furthermore, we will define orthogonal x-y coordinates in the plane of the triangle such that the $\hat{x}$ is parallel to $\underline{d}_{12}$. We can write this as

$$\begin{aligned} \underline{d}_{1x} &= t \cdot \underline{d}_{12x} + u \cdot \underline{d}_{13x} \\ \underline{d}_{1y} &= t \cdot \underline{d}_{12y} + u \cdot \underline{d}_{13y} \end{aligned} , \tag{3.8}$$

which may be solved to obtain values for u and t, noting that by our definition $\underline{d}_{12y} = 0$,

$$\begin{aligned} t &= \frac{\underline{d}_{1x}}{\underline{d}_{12x}} - \frac{\underline{d}_{1y} \cdot \underline{d}_{13x}}{\underline{d}_{13y} \cdot \underline{d}_{12x}} \\ u &= \frac{\underline{d}_{1y}}{\underline{d}_{13y}} \end{aligned}, \tag{3.9}$$

We may now interpolate the source function Stokes Vector in the direction of the LOS from the values at the triangle vertices linearly, using an equation that follows the same form as Equation 3.7. This is written as

$$\underline{J}_A = \underline{J}_1 + t(\underline{J}_2 - \underline{J}_1) + u(\underline{J}_3 - \underline{J}_1) \tag{3.10}$$

or rearranged this becomes

$$\underline{J}_A = (1 - t - u)\underline{J}_1 + t\underline{J}_2 + u\underline{J}_3. \tag{3.11}$$

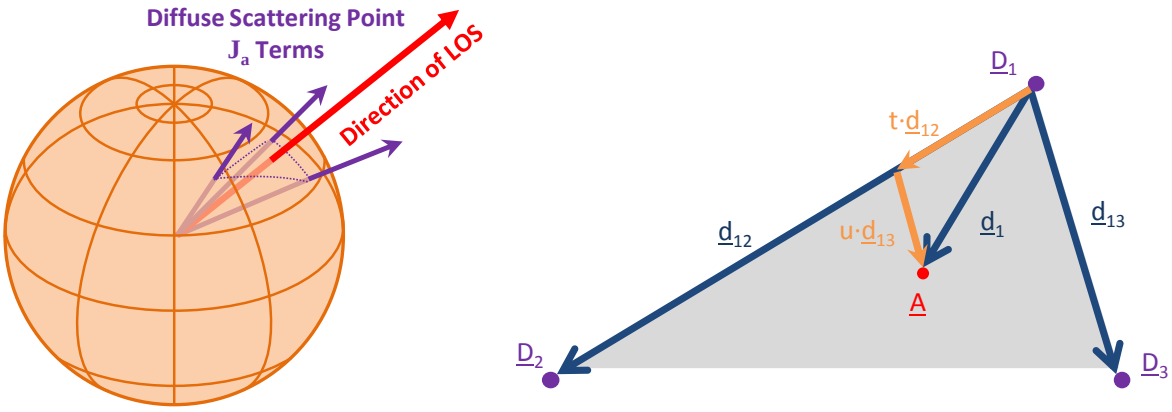

Figure 3.6: The source function Stokes Vector in the direction of the LOS is interpolated linearly from the triangle vertices.

The three vertex weights serve as three weighting consecutive ξ_i factors contributing to f_{Iai} in Equation 2.98, which is used to find the n^{th} order atmospheric radiance. If we say $\underline{J}_{3i} = \underline{J}_1$, $\underline{J}_{3i+1} = \underline{J}_2$, and $\underline{J}_{3i+2} = \underline{J}_3$ then these factors may be written as

$$\begin{aligned} \xi'''_{3i} &= 1 - t_i - u_i \\ \xi'''_{3i+1} &= t_i \\ \xi'''_{3i+2} &= u_i \end{aligned}. \tag{3.12}$$

To examine the effectiveness of these three interpolation schemes the first order source terms from DSPs were found for minimum energy spheres with 169, 196, 225, 256 and 324 directions. These values were calculated directly and involve no interpolation.

They can be taken to be reasonable representations of the source function due to the successful validation of first order light as discussed in Section 4.2 which also involved no interpolation of these source terms.

The source function distribution corresponding to the 169 point minimum energy sphere was used as sample set from which values could be interpolated. Values were then interpolated to the directions of the 324 point distribution so that the interpolants could be compared to the directly calculated values at those points. This was repeated interpolating from the 196, 225, and 256 point distributions as well. The results were sampled at 75.5 km in altitude for a solar zenith angle and solar azimuth angle, measured at the observer, of 52.88° and 142.55° respectively. The atmospheric conditions are identical to those used while comparing with another polarized RTM's results described in greater detail in Section 4.1, and the initial solar irradiance is normalized to 1.

Figure 3.7 is an example of the results of this comparison for Rayleigh scattered 325 nm light. Each plot in this figure represents a unit sphere with θ and ϕ in degrees along the the x and y axes respectively. The first column shows the directly computed values for a 324 point distribution while the second column shows values that were interpolated using the Shepard method from a 169 point distribution. The final column is the difference between the two sets, normalized to the range of values present in the first two columns. The rows represent the $\underline{J}_I$, $\underline{J}_Q$, and $\underline{J}_U$ elements of the source function Stokes Vector. The final element $\underline{J}_V$ is uniformly zero for Rayleigh scattering and so it was not included. Figures 3.8 and 3.9 use the Modified Shepard method and the linear interpolation method respectively, and are produced under otherwise identical conditions.

Because both of Shepard's methods allow us to select the number of data points used in Equations 3.2 and 3.5 this number was varied from four points to seven while performing the interpolations from the 169, 196, 225, and 256 point distributions for both 325 nm and 1700 nm light to sample either end of the optical spectrum. The sum of the absolute difference over the unit sphere between the interpolated $\underline{J}$ and the directly calculated $\underline{J}$ were recorded and the results are plotted in Figures 3.10, and 3.11.

From the trends shown in this study it appears that if they continue the Modified Shepard method may be more successful when using ten or more points for the interpolation but this is contrary to our goal of maintaining speedy calculations by using only

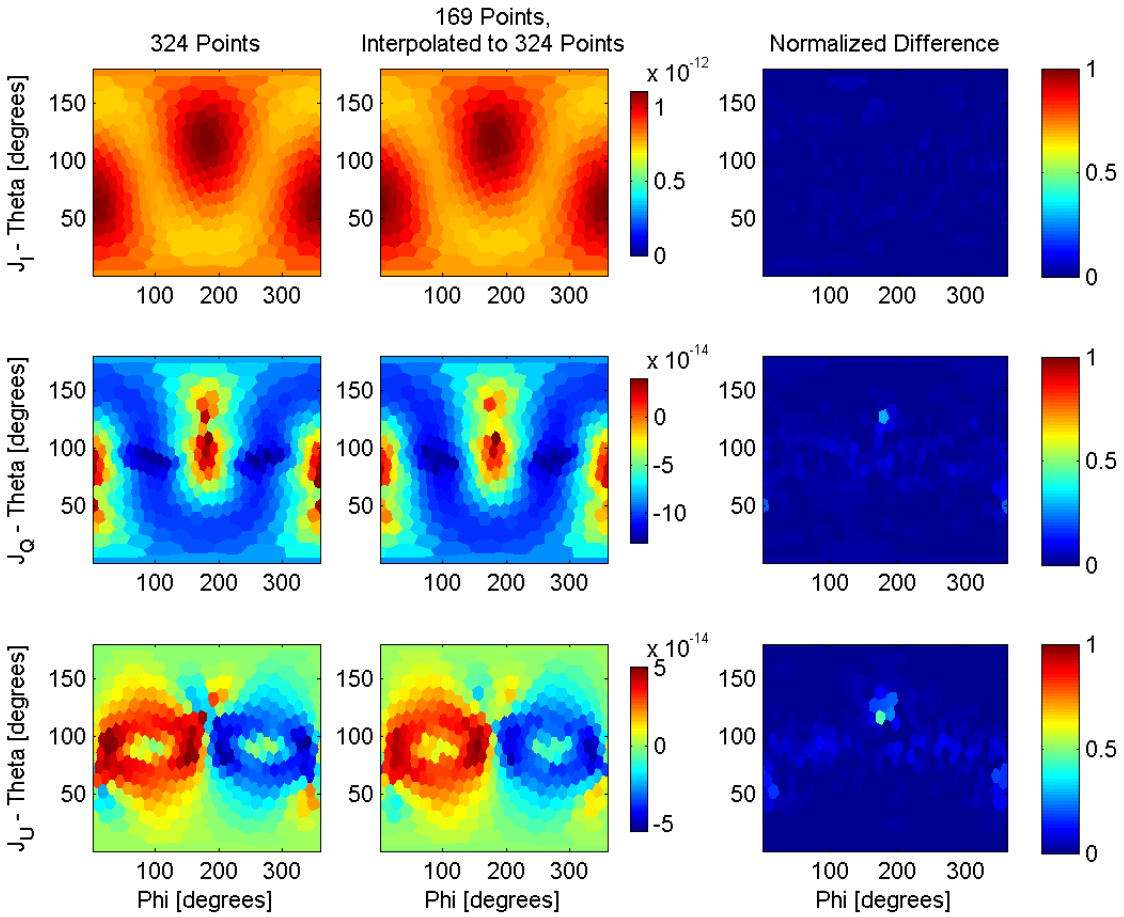

Figure 3.7: A comparison of directly computed source function Stokes Vectors between 324 point distribution over a unit sphere and a field interpolated using the Shepard method from a 169 point distribution, using 5 points for each interpolation.

a few of the nearest points. When using fewer points the standard Shepard method uniformly performed better than the modified version. For both wavelengths and for each initial point distribution using five interpolation points minimized the total error observed over the unit sphere while employing the Shepard method. This configuration will now be compared to the triangular linear interpolation method.

The sum of the absolute differences in the source function Stokes Vectors for the triangular linear interpolation from 169, 196, 225, and 256 point distributions for both 325 nm and 1700 nm light are shown in Table 3.1. An analogous table for the standard Shepard method, using 5 interpolation points, is shown in Table 3.2.

In these tests the Shepard method is slightly superior to the triangular linear in-

	325 nm [10^{-9}]			450 nm [10^{-10}]			765 nm [10^{-12}]			1700 nm [10^{-14}]		
	J_I	J_Q	J_U	J_I	J_Q	J_U	J_I	J_Q	J_U	J_I	J_Q	J_U
169	1.68	1.20	0.84	2.82	2.16	2.18	6.51	6.44	6.44	1.18	1.21	1.20
196	1.60	1.14	0.75	2.69	2.14	1.94	6.13	6.21	5.85	1.10	1.17	1.09
225	1.56	1.11	0.69	2.67	2.03	1.67	6.27	5.62	4.80	1.13	1.06	0.90
256	1.42	1.17	0.62	2.37	2.03	1.58	5.35	5.68	4.64	0.96	1.07	0.87

Table 3.1: The sum of absolute difference for triangular linear interpolation over the unit sphere for several wavelengths. Each row corresponds to a different initial point distribution from which to interpolate.

	325 nm [10^{-9}]			450 nm [10^{-10}]			765 nm [10^{-12}]			1700 nm [10^{-14}]		
	J_I	J_Q	J_U	J_I	J_Q	J_U	J_I	J_Q	J_U	J_I	J_Q	J_U
169	1.11	1.23	1.36	1.92	2.15	2.38	4.20	4.84	5.41	0.81	0.93	1.03
196	1.00	1.10	1.23	1.75	1.97	2.20	4.20	4.84	5.41	0.78	0.89	0.99
225	0.87	0.95	1.07	1.52	1.69	1.91	3.65	4.15	4.70	0.67	0.76	0.86
256	0.84	0.91	1.00	1.42	1.58	1.75	3.36	3.76	4.18	0.61	0.69	0.76

Table 3.2: The sum of absolute difference for the Shepard method, using 5 interpolation points, over the unit sphere for several wavelengths. Each row corresponds to a different initial point distribution from which to interpolate.

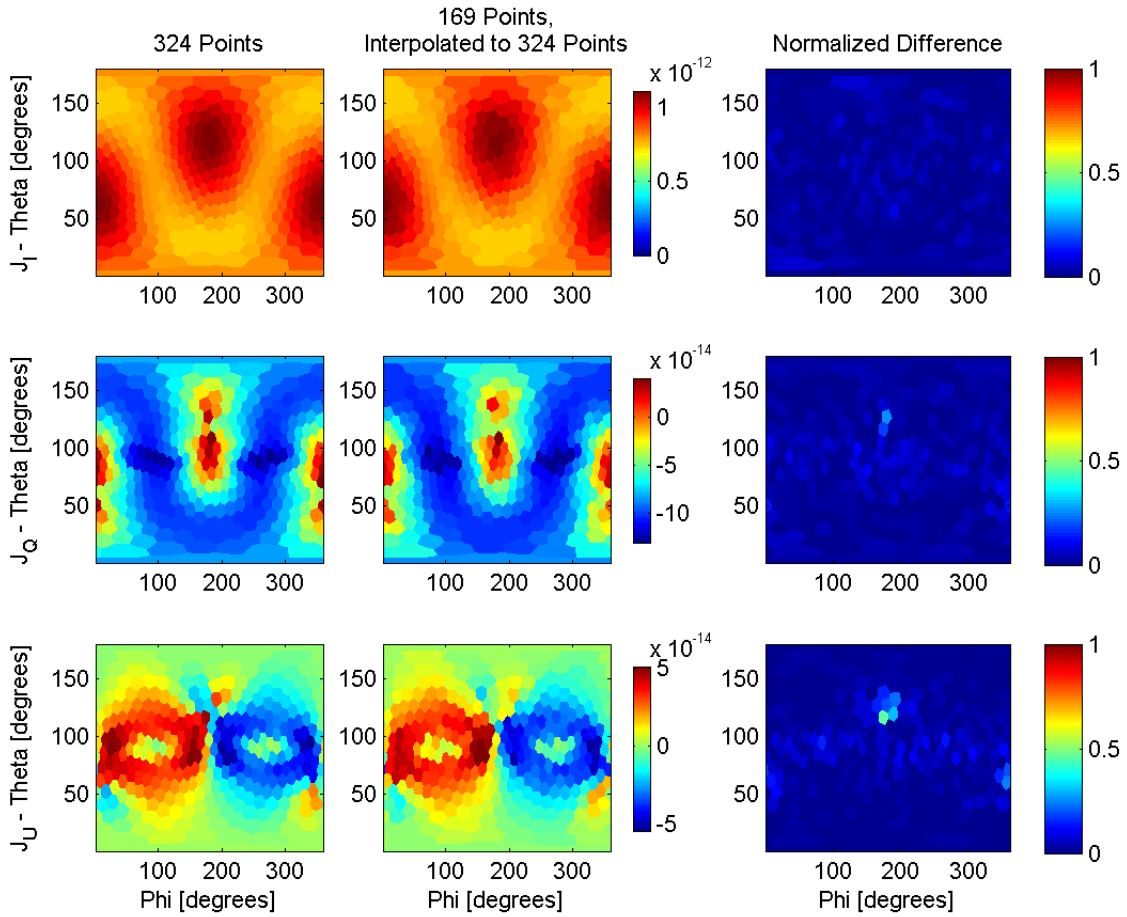

Figure 3.8: A comparison of directly computed source function Stokes Vectors between 324 point distribution over a unit sphere and a field interpolated using the Modified Shepard method from a 169 point distribution, using 5 points for each interpolation.

terpolation except for the J_U values for the lower two wavelengths. However using 5 points with the Shepard method nearly doubles the amount of memory required for source function links and weights that would be stored in the JValueTable objects, when compared to the linear interpolation method. Likewise it nearly doubles the number of calculations that must be performed while creating those links and computing the summations to find the radiance values. Base on the this trade off for speed and smaller memory for accuracy both methods should be made available to users of SASKTRAN.

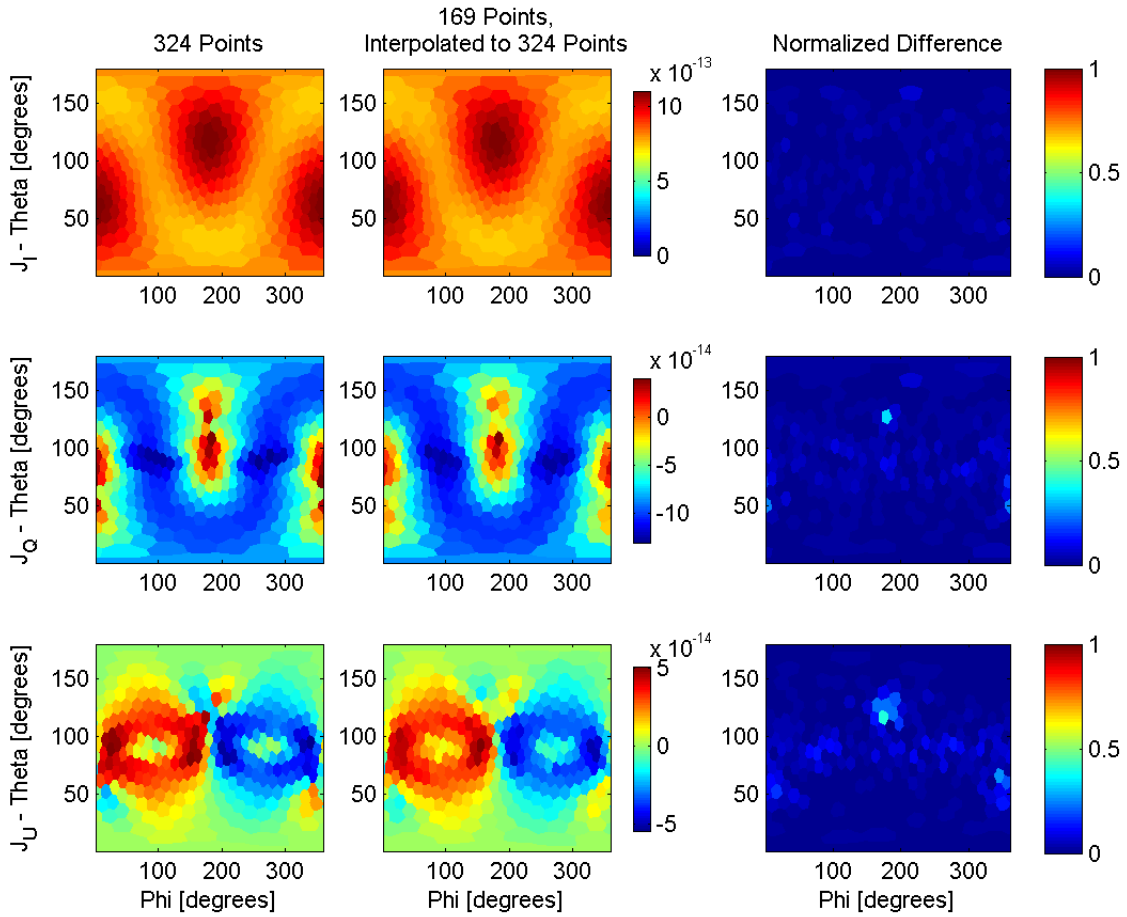

Figure 3.9: A comparison of directly computed source function Stokes Vectors between 324 point distribution over a unit sphere and a field interpolated using the triangular linear interpolation method from a 169 point distribution.

3.3 Rotating Source Terms Prior to Interpolation

By examining the plots in Figures 3.7, 3.8, and 3.9 and their differences it is easy to see that there are two areas in which all the interpolation schemes perform poorly because the J_Q and J_U values change too quickly. This would cause small errors to propagate throughout the model as higher orders of scattering are calculated. Major errors would result if the direction of the Observer Line of Sight corresponds to this erroneous region. It may be possible that a more sophisticated interpolation method could account for these rapid changes in the J_Q and J_U values. However it is possible to understand the cause of the rapid changes and prevent this from creating an issue

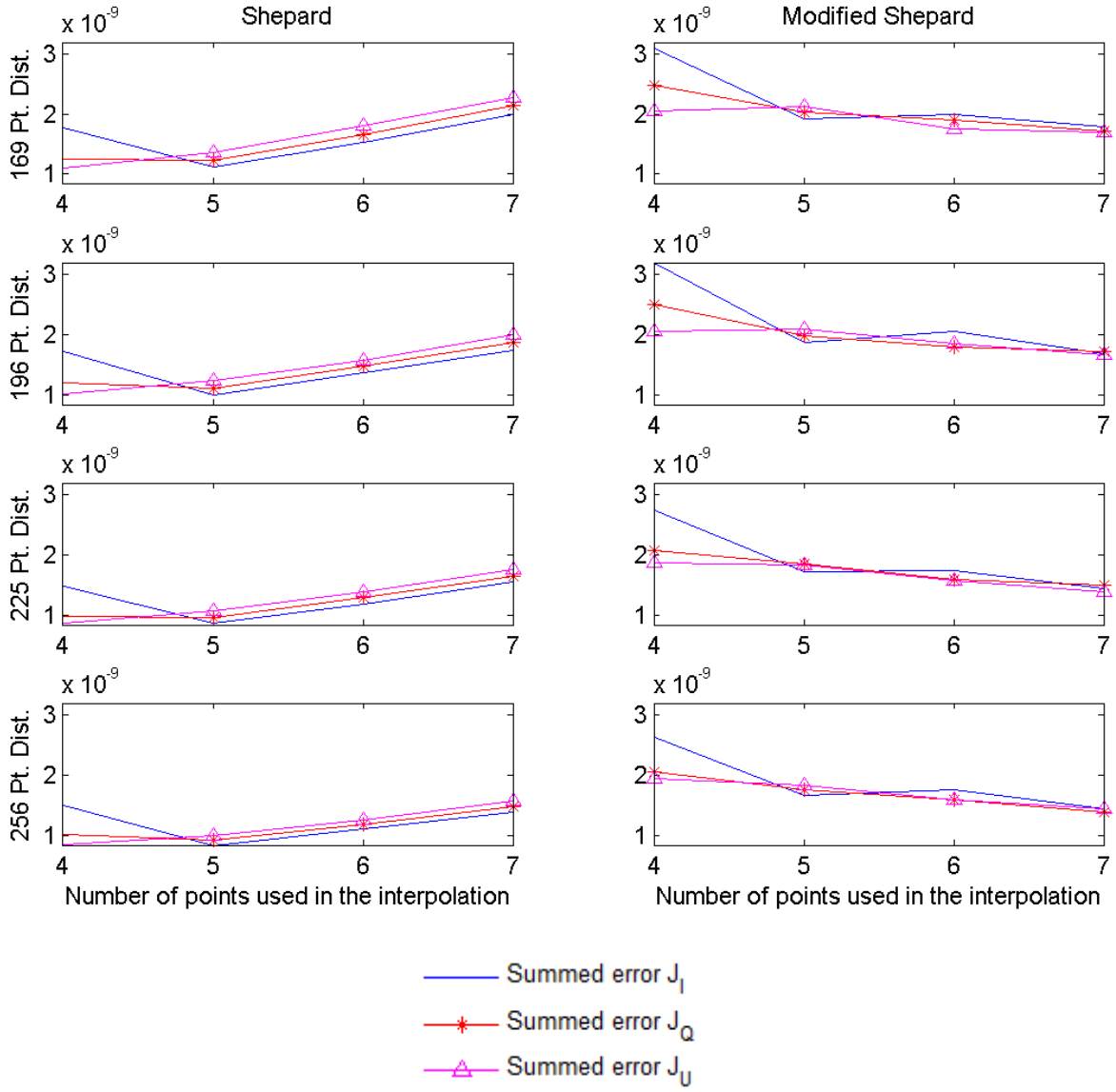

Figure 3.10: Comparing the Shepard method and the Modified Shepard method using the total interpolation error for 325 nm light, starting from 169, 196, 225, and 256 point distributions.

for the interpolation algorithm.

These two problematic regions correspond to the directions towards and away from the sun. As described in Section 2.5.1 the solar direction is used to define the reference plane for each source function Stokes Vector. Directions that are relatively close together on the unit sphere near the solar direction may actually have drastically different reference planes, and therefore drastically different J_Q and J_U values. To compensate

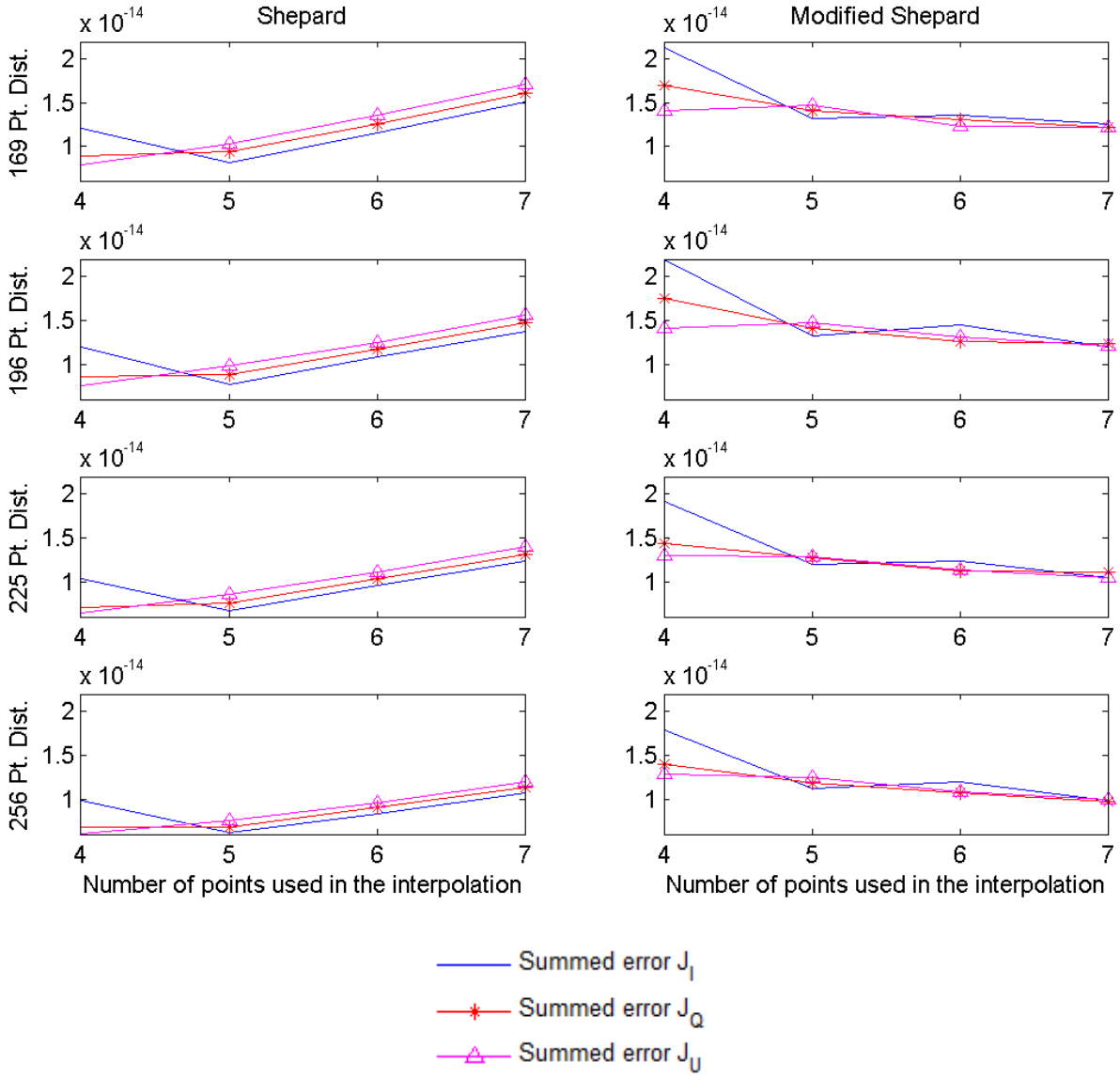

Figure 3.11: Comparing the Shepard method and the Modified Shepard method using the total interpolation error for 1700 nm light, starting from 169, 196, 225, and 256 point distributions.

for this a rotation matrix is applied to the different source vectors before adding them together by following the equation,

$$\underline{J}_i = \sum_j \xi_j \underline{\mathbf{R}}(\eta_j)\underline{J}_j. \tag{3.13}$$

Each contributing source term is rotated by some angle η_j which is taken to be the angle between a pair of unit vectors. These unit vectors are defined to be perpendicular

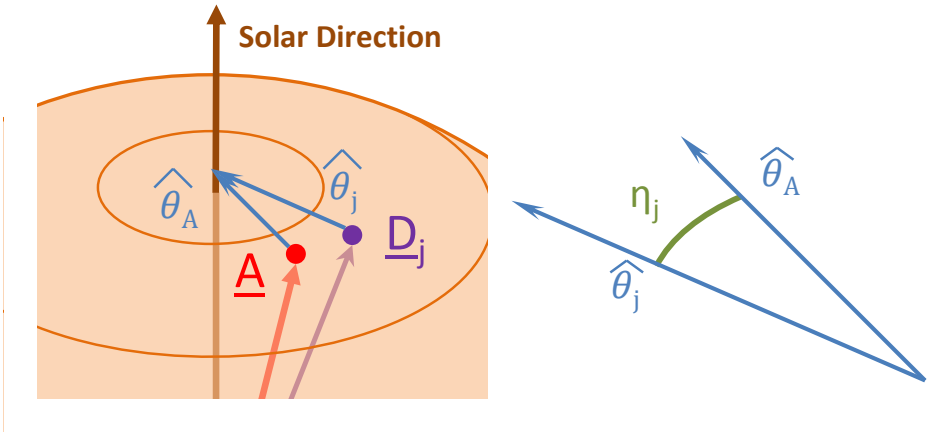

Figure 3.12: Prior to interpolation the source terms Stokes Vectors are rotated to fit the output direction

to the propagation direction and lying in the reference plane, corresponding to the $\hat{\theta}$ vectors shown in Figure 3.12. These rotation corrections are only valid for source function vectors that are approximately parallel with each other. As demonstrated by the improvement in the Figure 3.13 below over Figure 3.7 it is clear that the conditions for approximation are satisfied.

Outbound directions that are not close to being parallel or antiparallel to the solar direction do not require a rotation because the J_Q and J_U terms are relatively smooth. To improve the speed of the interpolation process in SASKTRAN the unnecessary rotations are omitted. Only outbound directions that were within 30° of being parallel or antiparallel with the solar direction were rotated. Following this procedure the results presented in Figure 3.13 were generated.

The results depicted in Figure 3.13 show a drastic improvement due to the application of the rotation matrices. The largest difference between interpolated values drops from 44% of the range of J_Q and J_U signals without rotation to 12% with rotation. These results imply the rotation of the source function Stokes Vectors prior to interpolation is important to achieving accurate results. As described in Section 3.1 the rotation angle for each source function Stokes Vector, η_j is stored in SASKTRAN in a JIndex object while calculating the interpolation weighting function, and it is used by a descendent class of JValueTableBase to complete the radiative transfer calculations.

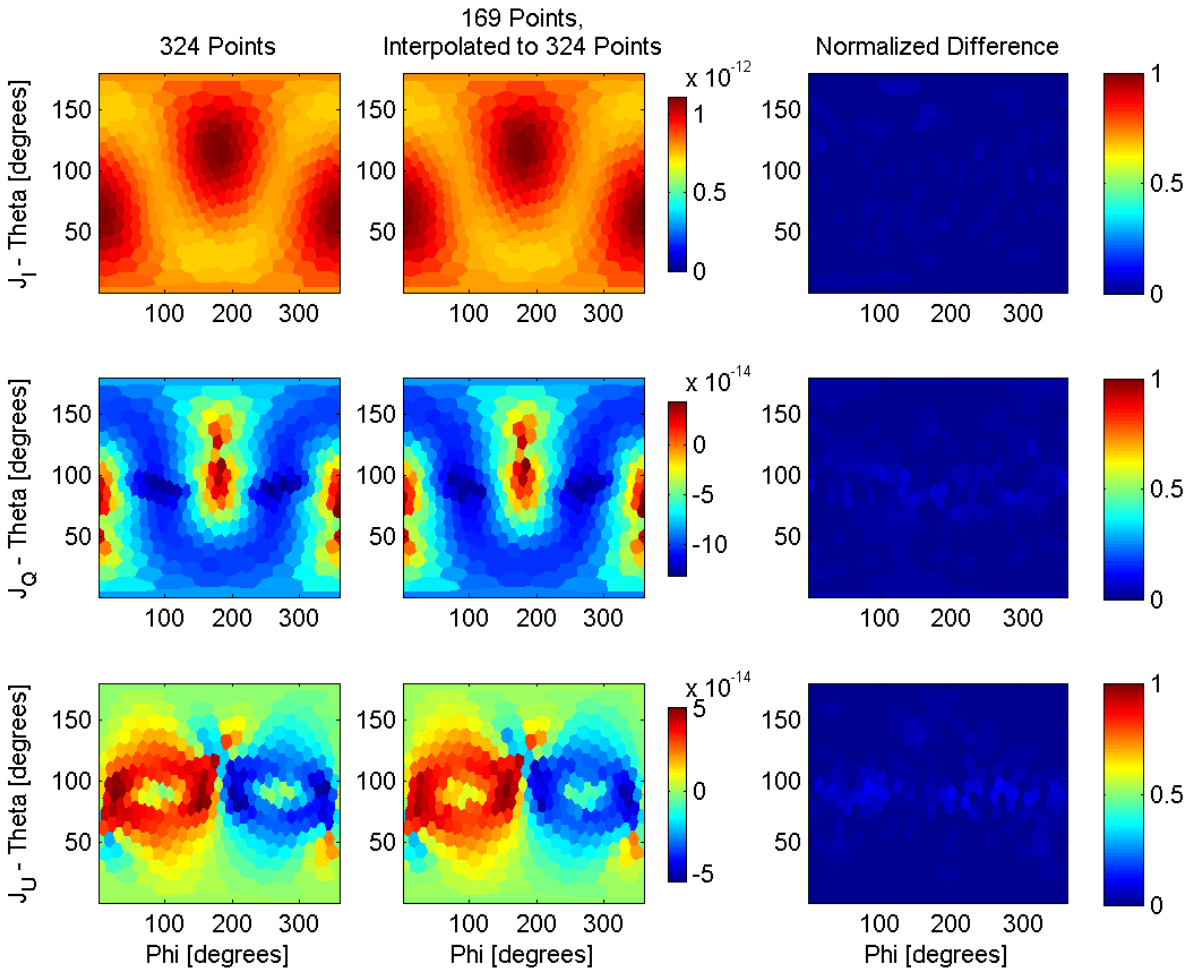

Figure 3.13: A comparison of directly computed source function Stokes Vectors between 324 point distribution over a unit sphere and a field interpolated using the Shepard method with rotations from a 169 point distribution, using 5 points for each interpolation.

Chapter 4

Evaluating Vector SASKTRAN

To validate the vector version of SASKTRAN its results will be compared to results produced by another RTM whose purpose is to simulate polarized radiative transfer that is in development, called vector SCIATRAN. The effects of polarized calculations on simulations including aerosols will also be discussed in this chapter.

The SCIATRAN line of RTMs was first developed by *Rozanov et al.* (2001) for use as a forward model to pair with the the SCIAMACHY (SCanning Imaging Absorption spectroMeter for Atmospheric CHartographY) instrument. SCIAMACHY is an eight channel diode array spectrometer that covers a wavelength range of 240-2385 nm. SCIATRAN supports both a plane-parallel mode and a spherical mode. In spherical mode the model solves the first order of scattering using a combined differential-integral approach for a spherical atmosphere. The multiple scattering source function is approximated using the solution to a plane-parallel atmosphere that is solved at varying solar zenith angles as illustrated schematically in Figure 4.1. To further improve this result it is possible for SCIATRAN to use this approximate spherical solution as the initial estimate for the Picard Iterative (PI) technique (*Rozanov et al.*, 2002). The PI technique employs a fixed point iteration to find a solution to the integral form of the radiative transfer equation. The boundary conditions are set at the top of the atmosphere and the Earth's surface then radiances at each layer of the atmosphere are updated based on nearby layers until an equilibrium condition is reached (*Kuo et al.*, 1995). In contrast to the successive orders of scattering technique each iteration of the PI method at a node n layers from a boundary can take into account up to n-orders of scattering (*Kuo et al.*, 1996).

Presently a vector version of SCIATRAN capable of modeling polarized radiative

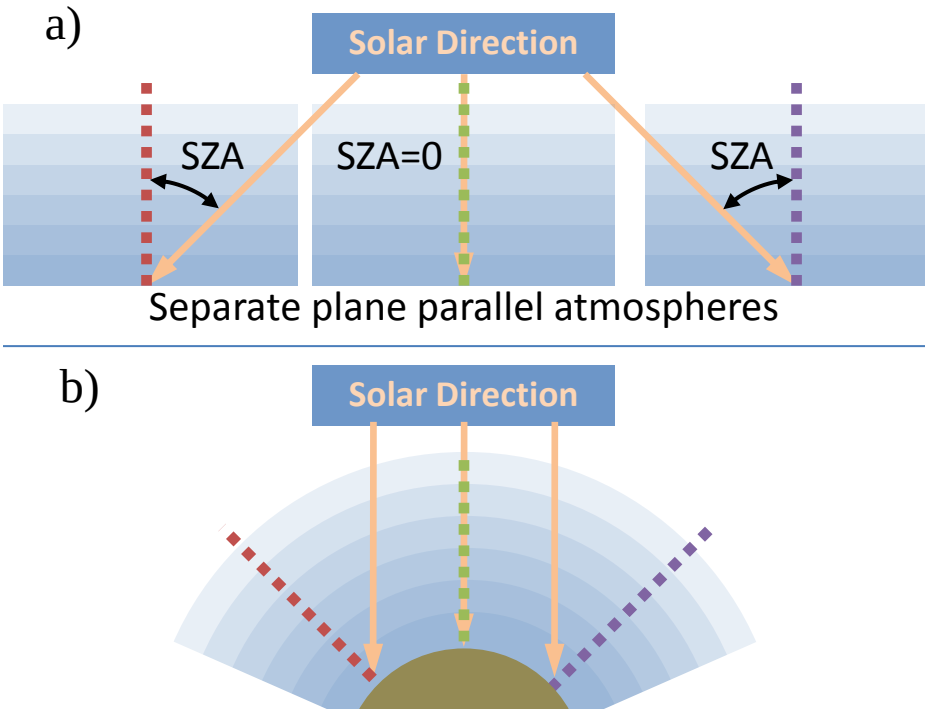

Figure 4.1: SCIATRAN uses plane parallel atmospheres at multiple solar zenith angles for multiple scattering (a) and interpolates values from these atmospheres to construct its spherical approximation (b).

transfer has been developed by Dr. Vladimir Rozanov and Dr. Alexei Rozanov. At the time of writing this document the PI method had not been yet implemented for the vector SCIATRAN. Liebing has made the vector SCIATRAN results available for a variety of viewing geometries and for a specific Rayleigh atmosphere (*Liebing, personal correspondence,* 2010).

The motivation in developing a vector SASKTRAN is to serve as a valuable tool in retrievals in the future, especially while retrieving SSA. To estimate and evaluate the impact of polarized radiative transfer calculations on the SSA retrieval process it will be useful to simulate conditions where SSA is present in the atmosphere and examine the resultant spectra. The details of the SaskMART SSA retrievals provided in Section 1.3.2 define a retrieval vector used to numerically obtain a solution to the aerosol extinction profile. It will also be useful to generate retrieval vectors from polarized and nonpolarized results for varying aerosol conditions to discuss the impact of using the vector SASKTRAN. To obtain these simulations viewing geometries for a profile can be constructed using the locations, directions, and times for the recorded

exposures from an OSIRIS scan. Atmospheric conditions can be established using common climatologies and SSA distributions for the various cases can be constructed based on long term measurement series.

The following section will discuss the efforts undertaken to reproduce the circumstances under which the vector SCIATRAN results were generated. The subsequent two sections will compare the results for single scatter calculations and multiple scatter calculations respectively produced by the vector SCIATRAN and vector SASKTRAN models. The final section in this chapter will examine simulated spectra and retrieval vectors and go on to discuss the effects the vector SASKTRAN's polarized results will have on aerosol retrievals in the future.

4.1 Matching SCIATRAN Conditions

The results presented from the polarized SCIATRAN were produced under specific circumstances that had to be reproduced in SASKTRAN before a comparison could take place. All the results were produced with an observer at 100 km altitude and assuming a spherical Earth with a 6370 km radius. The observer solar zenith angle, ς, is the angle between the solar direction and the zenith at the observer as shown in Figure 4.2. The observer solar azimuth angle, ϖ, is the angle measured between the projection of the solar direction on the x'-y' plane and projection of the line of sight, $\hat{\Omega}$, on the x'-y' plane, also shown in Figure 4.2. For each specified pair of ς and ϖ the RTM calculates results for a range of line of sight tangent altitudes from 0 to 60 km at 5 km intervals.

The SCIATRAN results were calculated for wavelengths of 325, 450, 765.1, and 1700 nm. Only Rayleigh scattering, without absorption, was considered and the Earth albedo was zero. A standard set of atmospheric conditions was provided that specified pressure and temperature, as well as the concentration of O_2, H_20, CO_2, N_2O, CO, and CH_4. These atmospheric parameters are listed in Appendix C. From this information it is possible to calculate the relevant optical properties such as the scattering coefficient and extinction values.

There are several different approximate equations to find scattering extinctions from atmospheric conditions. SCIATRAN uses equations presented by *Edlen* (1953) and *Bodhaine et al.* (1999) to find the index of refraction and then the scattering extinctions. To rule out differences between models that may result from differences

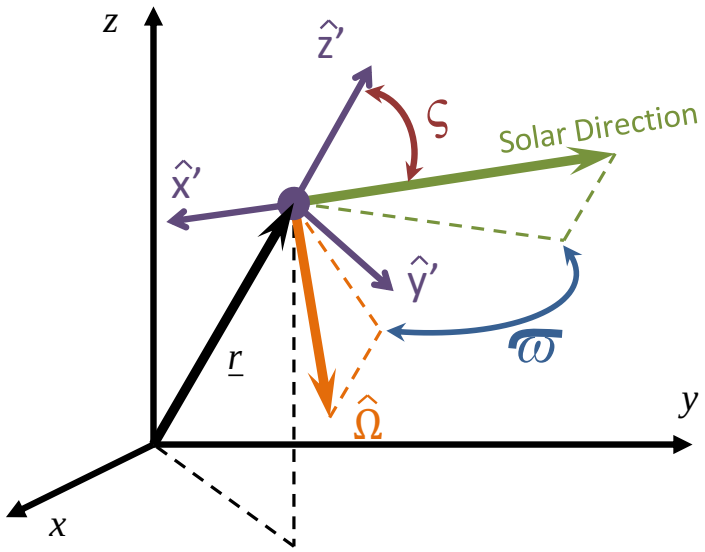

Figure 4.2: The local coordinates used to specify the viewing geometry while comparing with SCIATRAN

in these calculations Liebing provided the resulting extinctions to be used directly in different RTMs. These precalculated extinctions are listed in Appendix D.

4.1.1 A Spherical Earth

The shape of the Earth is very near to that of an oblate spheroid with the flatter regions near the poles and an outward bulge around the equator caused by the Earth's rotation. Within SASKTRAN this shape is approximated using an osculating sphere system. The spheroid shape of the Earth is obtained using the IAU1976 reference geoid (*Bourassa*, 2007) which is within 100 m of the gravitational shape of the Earth. A reference latitude and longitude is chosen based on the average location where the Observer Lines of Sight are tangent to the surface. At this latitude and longitude the north-south curvature of the surface is calculated from the reference geoid and a sphere of the same curvature is used to represent the Earth within SASKTRAN.

This approach allows SASKTRAN to use a truly spherical Earth and atmospheric shells, which makes calculating ray path lengths far simpler and quicker than using an oblate spheroid. It also means that despite this simplification the curvature will be very accurate around the tangent point, where the line of sight contributes most to the final radiance.

The newly polarized version of SCIATRAN uses a truly spherical Earth for the

first order of scattering while higher orders are approximated using a parallel plane atmosphere. To generate the comparison data SCIATRAN used a fixed Earth radius of 6370 km, which was not an option in SASKTRAN.

The SASKTRAN class nxGeodetic is responsible for transforming between coordinate systems and therefore it is also responsible for accessing the IAU1976 reference model, and creating the true sphere that represents the Earth in order to perform these calculations accurately. To address the differences between the spherical Earth in SCIATRAN and SASKTRAN in this work the vector SASKTRAN was given a feature that allows users to override the osculating sphere system. When activated the user defines the desired constant radius. Anywhere within SASKTRAN that a nxGeodetic object is created the sphere that would normally be created based on the curvature of the oblate spheroid is overwritten with the desired sphere. Users of the vector SASKTRAN now have the ability to define a fixed radius Earth which will be useful while comparing it to other models.

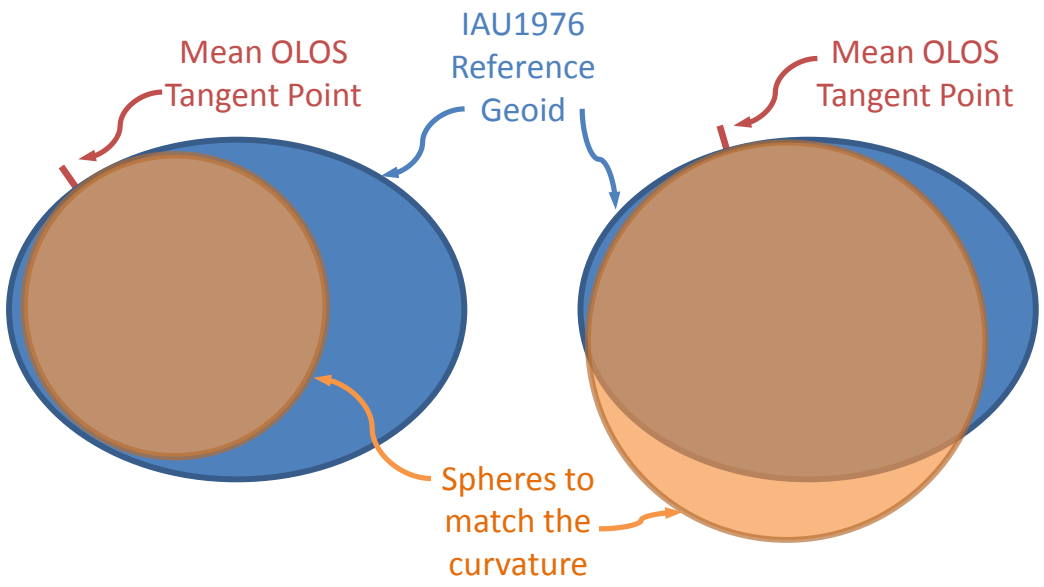

Figure 4.3: By default the sphere used to represent the Earth in SASKTRAN will be that which best matches the curvature of the Earth at the average OLOS tangent point.

4.1.2 The Viewing Geometry

There are a variety of ways to specify the viewing geometry within a RTM. Conventions in different models have evolved throughout their developmental processes and at times it is difficult to share and compare their results. Differences in nomenclature between development groups create ambiguity and may introduce errors while converting from one system to another. For instance the term 'solar zenith angle' may describe different angles within SASKTRAN and SCIATRAN. Viewing geometry conventions used within these two models are shown in Figure 4.4.

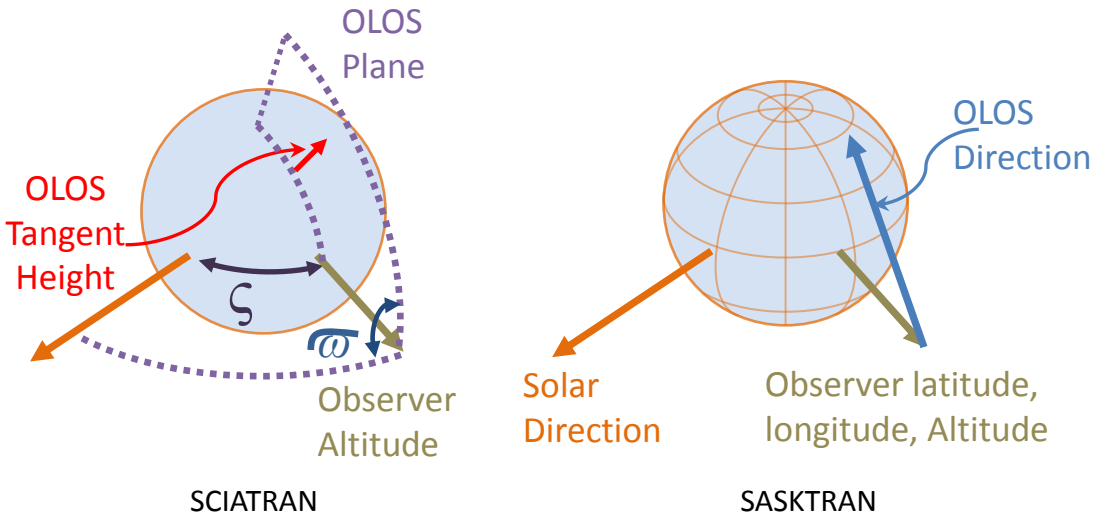

Figure 4.4: Each system specifies the viewing geometry and has been adopted as the convention in its respective radiative transfer model.

The SCIATRAN viewing geometry is specified by the observer line of sight tangent altitude and the coordinates defined in Figure 4.2. At an altitude of 100 km the observer's solar zenith angle ς, solar azimuth angle ϖ, and a set of tangent altitudes defines the viewing geometry. These coordinates are not sufficient to uniquely specify the location of the observer with respect to the true Earth. However the symmetry in the radiant field about the solar direction for an atmosphere composed of spherical homogeneous cells makes this ambiguity in the actual position moot in a spherical RTM.

The osculating sphere system described in Section 4.1.1 creates spheres of different sizes to represent the Earth that best match the measured curvature of the true Earth around the Observer Line of Sight tangent points. In general the ambiguity in the

observer position relative to the Earth resulting from SCIATRAN's coordinate system do not allow the nxGeodetic class to select a sphere to represent the Earth. To eliminate the ambiguity SASKTRAN's user interface class forces the user to explicitly specify the observer's position in space, the direction of the sun, and the observer's line of sight.

The comparisons with SCIATRAN were performed with a fixed radius as described in Section 4.1.1 by overriding this osculating sphere system. So for the purposes of these comparisons the coordinates used by SCIATRAN still define a unique viewing geometry. Functionality was added to the vector SASKTRAN that converts the coordinates used by SCIATRAN into those normally accepted by SASKTRAN.

To convert SCIATRAN coordinates to SASKTRAN coordinates, first the sun is assumed to be directly above the equator at the the prime meridian. The observer location is defined to be at 0 ° latitude, ς longitude, and at 100 km altitude. A plane containing the observer position vector and the solar direction is then rotated by an angle ϖ about the observer position to create the OLOS plane. Finally tangent point heights are used to calculate the OLOS direction lying in that plane. This sequence is shown schematically in Figure 4.5.

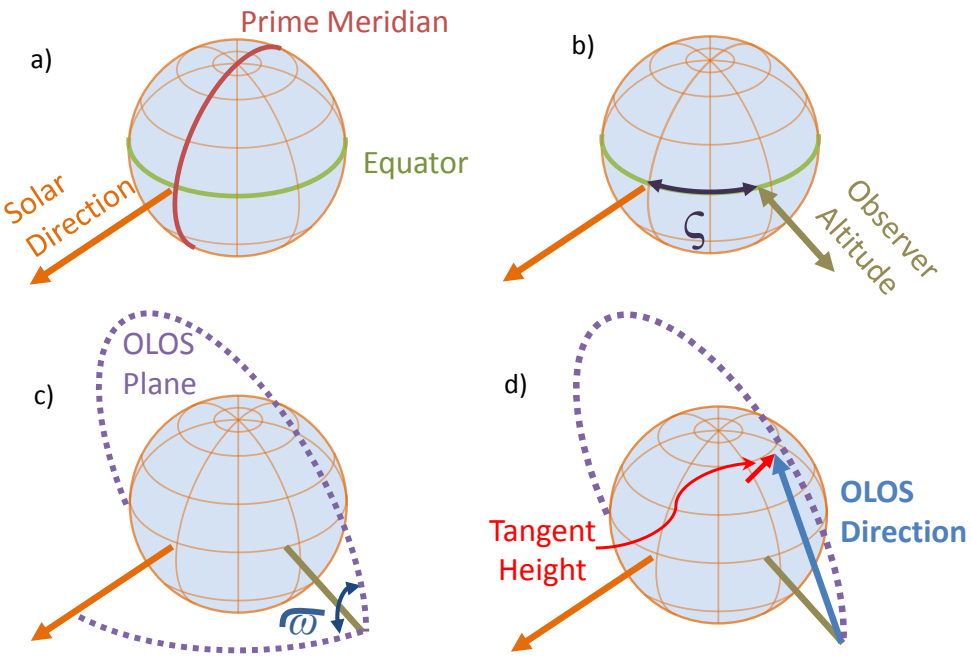

Figure 4.5: The process followed to calculate the SASKTRAN viewing geometry coordinates from a SCIATRAN viewing geometry specification.

4.1.3 The Atmospheric State

The SASKTRAN optical properties classes store and provide coefficients and extinction values to other components of the model based on location and directional information. These coefficients and extinctions are obtained from the class AtmosphericState. This class allows users to select climatologies of atmospheric conditions, which are then used to calculate the optical properties. These could be user generated climatologies written into a text file or standard published climatologies like the Mass Spectrometer Incoherent Scatter 90 atmospheric model (MSIS 90) or the European Centre for Medium-Range Weather Forecasts database (ECMWF) for example.

Liebing has provided information about the atmospheric makeup used while generating the polarized SCIATRAN results. From this it is possible to use the AtmosphericState class to calculate the optical properties. There are several ways to perform these calculations and apply different correction factors. These differences could propagate through the vector SASKTRAN introducing differences in the results that are not relevant to the polarized adaptations that are the subject of this work. To eliminate the possibility of these discrepancies Liebing also provided the scattering coefficients that were used in SCIATRAN. The scalar SASKTRAN model did not have the ability to use these coefficients directly and so modifications were required to use these coefficients.

The C++ programming language feature of inheritance was used to develop a class that could be used to replace AtmosphericState for comparison with SCIATRAN. An abstract parent class for AtmosphericState was written, called AtmosphericStateBase, such that any of its children classes are required to have the same interface as AtmosphericState. This means that any child of AtmosphericStateBase could replace AtmosphericState in SASKTRAN without affecting the functionality of the rest of the model.

Another class, AtmosphericState_scatterCoeffFromFiles, was written that inherits from AtmosphericStateBase. It serves to provide the same information to the rest of the model that AtmosphericState does but retrieves the information from data files instead of calculating them based on climatologies.

4.1.4 Vector SASKTRAN Configuration Limitations

The design of SASKTRAN leaves many options up to the user that may be specified prior to runtime. Some of these options include the number of outbound rays calculated

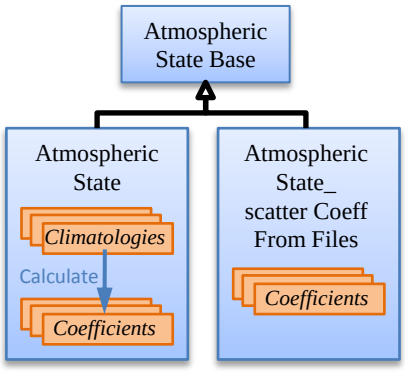

Figure 4.6: A parent class, AtmosphericStateBase, was created for AtmosphericState. The class AtmosphericState_scatterCoeffFromFiles inherits from the base class such that it can take the place of AtmosphericState without interfering with the rest of SASKTRAN.

by a DSP as described in Section 3.2, the number of inbound LOSs at DSPs, the number of Diffuse Profiles for varying SZAs as depicted in Figure 2.6, and various other resolutions used for numerical integrations.

For the comparisons that follow source functions were found for 196 outbound directions over a minimum energy sphere and inbound rays were constructed on a 96x60 zenith-azimuth grid that was distributed over a unit sphere. Lower resolutions produced a banded pattern that was visible when examining the interpolation tests shown in Section 3.2 that were eliminated at an inbound resolution of 96x60. Inbound resolutions higher than that produced no discernable improvement.

The scalar SASKTRAN has a small enough impact on system memory that it easily runs on modern desktop computers. The vector SASKTRAN calculates far more information and therefore is significantly more taxing on computer resources. Polarized calculations require a 4x4 phase matrix to replace each scalar phase function which are precalculated for each inbound and outbound direction pair and a 4 element vector to replace each scalar source functions at DSPs. Therefore the polarized calculations require 4 times the amount of memory for radiance and source function information and 16 times the amount of memory for phase scattering information when compared to non-polarized calculations. To provide a point of reference: a vector simulation required approximately 7.5 GB and would take more than a day, whereas an equivalent scalar simulation required approximately 2 GB and take around 10 minutes.

Because of this massive increase in memory demands and the limitations of the available hardware it was necessary to use a single Diffuse Profile for the comparisons

used below. This means that instead of interpolating between independent Diffuse Profiles along lines of sight a single Diffuse Profile is effectively translated around the surface of the Earth as depicted in Figure 4.7. The source functions are then interpolated to the LOS from different outbound terms of the same profile.

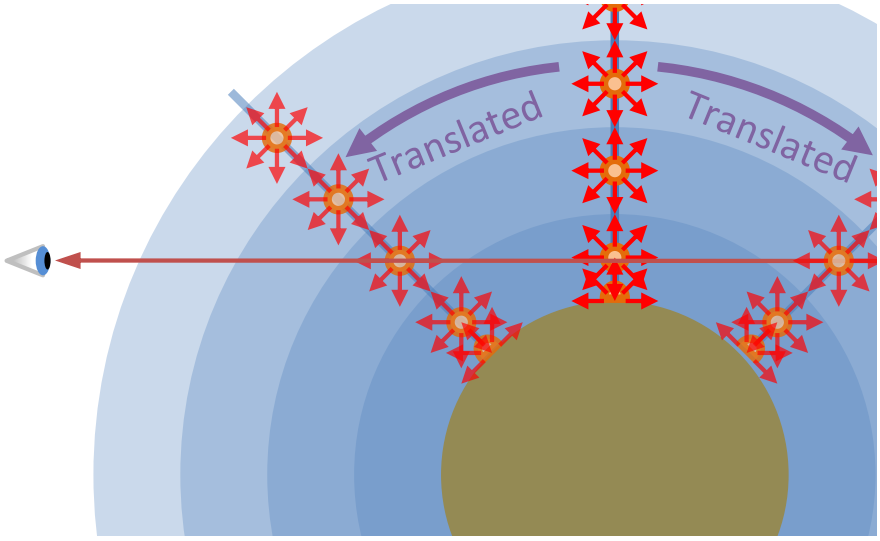

Figure 4.7: One Diffuse Profile is calculated at the tangent point. It is then translated around the surface of the Earth to provide source terms at different positions in the atmosphere.

This translation around the surface ensures that the local zenith points away from the surface of the Earth. This is important to accurately account for radiance that has been scattered from the Earth's surface to the diffuse points. A single Diffuse Profile was also successfully used by *Bourassa* (2007) which produced results in close agreement with other RTMs and OSIRIS measurements.

The demand on computer resources for polarized calculations in SASKTRAN also influenced the choice of the source term interpolation scheme used in the comparisons with SCIATRAN. Although the Shepard method described in Section 3.2 produced the best results it would nearly double the computer memory and time required to calculate the interpolation when compared to the triangular linear interpolation. This linear interpolation method, with the reference rotations described in Section 3.3, was used.

4.2 SCIATRAN Single Scatter

The single scatter contribution to the observed signal is usually very large compared to higher orders and RTMs are often designed to handle the first order of scattering differently than the higher orders. This is done so models can be more accurate for the first order and use optimizations and approximations for higher orders to improve speed.

For example SASKTRAN computes the first order source function contributions directly, second and higher orders are calculated differently using different components of SASKTRAN. This was described in Section 2.2.1 where in Figure 2.8 the OLOS is depicted calculating the first order radiance terms from the solar information and higher orders rely on information from the DSPs as well. SCIATRAN uses a truly spherical Earth geometry for the first order, and uses approximations from plane parallel solutions for higher orders. Because of the significance of the first order it is common to compare its contribution to the final signal when comparing RTMs prior to comparing all orders of scattering.

The models were set to compute the observed radiance for the configurations described above, using a normalized solar irradiance, $F_o = 1$. The results from the polarized RTMs were recorded as the parameters

$$\begin{aligned} & I && [1/\text{str}] \\ q &= Q/I \\ u &= U/I \\ v &= V/I \\ p &= \sqrt{q^2 + u^2 + v^2}, \end{aligned} \tag{4.1}$$

where p is a normalized and unitless measure of the degree of polarization. The normalized irradiance from the sun leaves I with simply units of 1/str and because q, u, and v are all normalized to the value of I they are unitless. Also it should be noted that Rayleigh scattering can never produce circularly polarized light so v is uniformly zero and is not shown in the figures below. Each column of plots in Figure 4.8 represents I, q, u, or p respectively. Each row represents the results for a wavelength of light.

Figure 4.8 shows that there is very good agreement between the two models for single scatter results. On these scales there is no visible difference between the results from SCIATRAN and SASKTRAN.

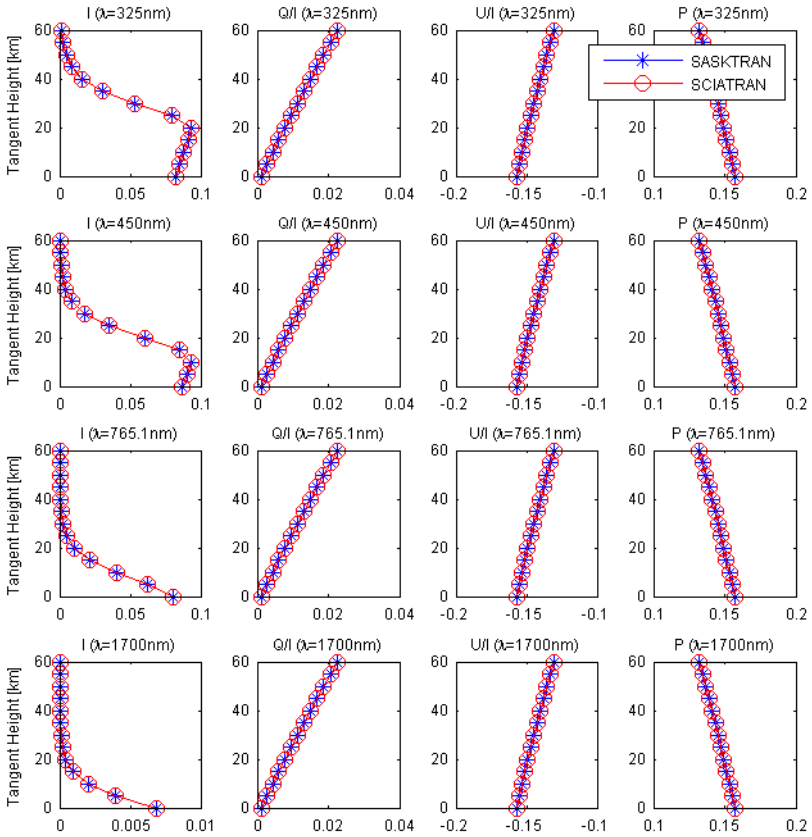

Figure 4.8: The polarized single scatter radiative transfer results for $\varsigma = 22.23°$ and $\varpi = 77.77°$ at varying wavelengths

To examine the differences between the two models we calculate the parameters

$$\begin{aligned} \delta I/I_{\text{SCIA}} &= (I_{\text{SASK}} - I_{\text{SCIA}})/I_{\text{SCIA}} \\ \delta q/q_{\text{SCIA}} &= (q_{\text{SASK}} - q_{\text{SCIA}})/q_{\text{SCIA}} \\ \delta u/u_{\text{SCIA}} &= (u_{\text{SASK}} - u_{\text{SCIA}})/u_{\text{SCIA}} \\ \delta p/p_{\text{SCIA}} &= (p_{\text{SASK}} - p_{\text{SCIA}})/p_{\text{SCIA}}. \end{aligned} \tag{4.2}$$

In Figure 4.9 it is possible to see that there is a detectable difference between the two signals but it is very small and these results are very acceptable. A systematic difference in the I values is clearly visible. The $\delta I/I_{\text{SCIA}}$ increases with decreasing altitude until it reaches a peak. Below the peak it rapidly decreases again. This peak becomes lower in altitude with increasing wavelength and roughly corresponds to the peak of the I signal itself. For the longer two wavelengths used in this study the peak would occur below the surface of the Earth. The reason for the peak in the I signal is

related to the Rayleigh optical depth of the atmosphere.

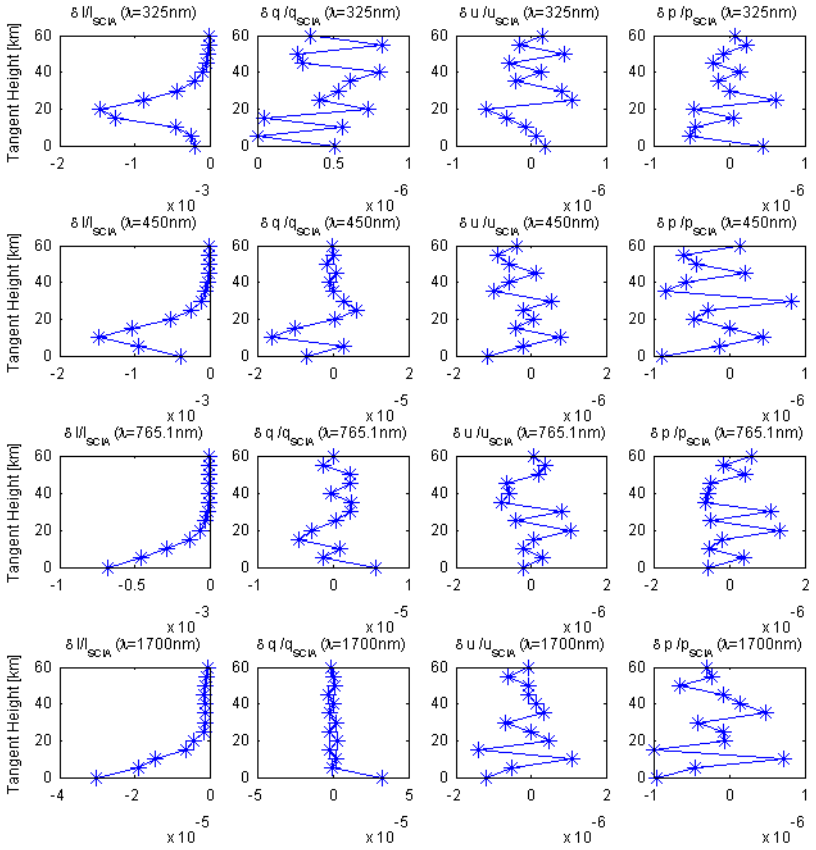

Figure 4.9: The normalized difference in polarized single scatter radiative transfer results for $\varpi = 22.23°$ and $\varsigma = 77.77°$ at varying wavelengths

When the line of sight has a very high tangent altitude it passes through a small portion of the atmosphere. Therefore it only intersects a small number of scatterers to contribute source functions to the the observed radiance. As the tangent height becomes lower the path length increases and so does the density of the scatterers. So I initially increases drastically with a decreasing tangent altitude. However as light from the sun travels down through the atmosphere more and more of it has been scattered away and eventually the signal becomes zero. Even though the line of sight path length is longer and there are more scatterers, when the tangent altitude goes low enough there is no more light to be scattered towards the observer. This effect creates the peak seen in the I signal for 325 nm and 450 nm in Figure 4.8.

The reason the peak shifts downwards in altitude for longer wavelengths is due to the Rayleigh scattering cross section of Equation 2.55. This equation shows that the probability of Rayleigh scattering is dependant on a factor of $1/\lambda^4$. So longer wavelengths are scattered much less than shorter wavelengths and therefore they can penetrate the atmosphere all the way to the Earth's surface.

The rate that the radiance signal changes with altitude peaks as well. This is shown in the right column of plots in Figure 4.10 as calculated by a simple forward difference numerical derivative. This means that minute differences in calculating path lengths between models will lead to larger differences in radiance signals at those peaks. Looking at the left column of plots in Figure 4.10 it is clear that the peak in $\delta I/I_{\text{SCIA}}$ roughly corresponds to this $\mathrm{d}I/\mathrm{d}z$.

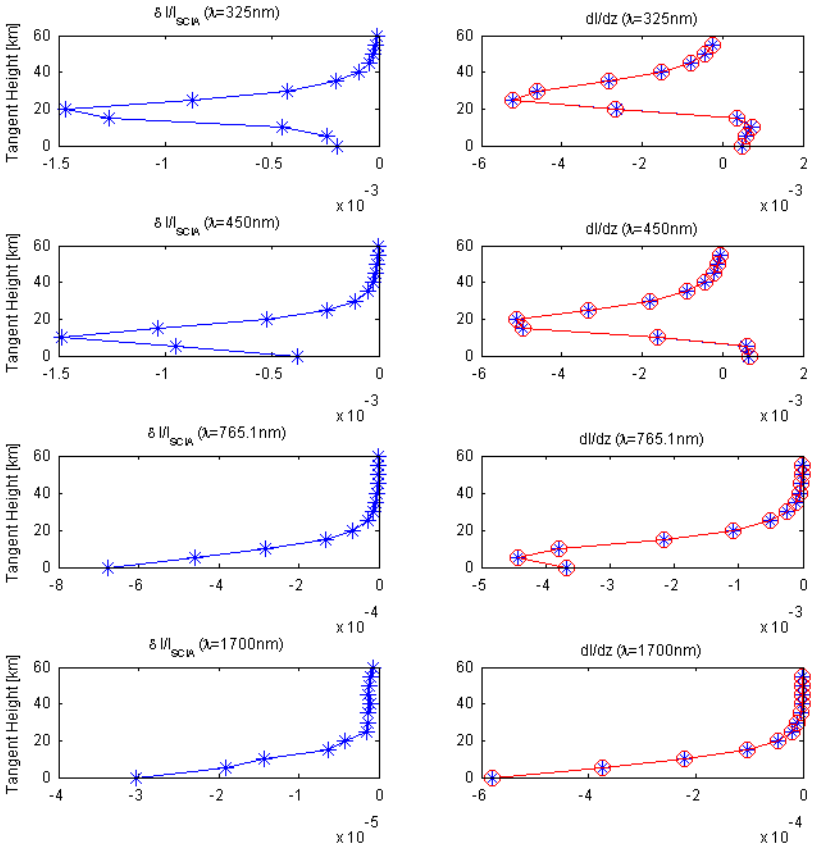

Figure 4.10: The normalized difference in radiance for $\varpi = 22.23°$ and $\varsigma = 77.77°$ at varying wavelengths, compared to the change in radiance with respect to altitude.

The other values plotted in Figure 4.9 (q, u, and v) do not exhibit this peaked structure because they have been previously normalized to the I. The plots of $\delta q/q_{\text{SCIA}}$, $\delta u/u_{\text{SCIA}}$, and $\delta p/p_{\text{SCIA}}$ show that any further disagreement is very small and appears to be random. This level of disagreement is likely due to small rounding differences. Further figures, all showing similarly good agreement between SASKTRAN and SCIATRAN single scatter results, may be found in Appendix A.

4.3 SCIATRAN Multiple Scatter

Each order of scattering contributes significantly less to the final observation than the order of scattering that preceded it. *Bourassa* (2007) states that using the scalar SASKTRAN ten orders of multiple scattering account for more than 99% of the total radiance over OSIRIS's wavelength range. For these comparisons twenty orders of scattering were used in the vector SASKTRAN.

It should be expected that contributions to the final observation scattered more than once will depolarize the signal and at the same time increase I. The first order source terms have all been scattered at the same scattering angle, between the solar vector and the line of sight. This means that all the J_Q and J_U components along the line of sight will add constructively and leave a relatively high degree of polarization. Higher order source terms are composed of light from all directions in the atmosphere that have been scattered into the line of sight, interfering destructively. This will introduce randomness to the polarization state. Therefore as higher orders of scattering are added to the final observation the parameters q, u, and p are expected to decrease and I is expected to increase.

Shown in Figure 4.11 are plots of vector SASKTRAN and SCIATRAN multiple scatter results. Each column of plots shows I with units of 1/str as well as the dimensionless factors q, u, and p. Each row represents the results for a different wavelength of light.

The multiple scatter results for I continue to agree very well as shown in the first column of Figure 4.11. While the plots from the other columns do show disagreement between the q, u, and p parameters for shorter wavelengths, results from both models exhibit the same trends.

These plots illustrate a small increase in the I parameter with the addition of multiple scattering when compared to Figure 4.8 as is expected. Also the parameter p

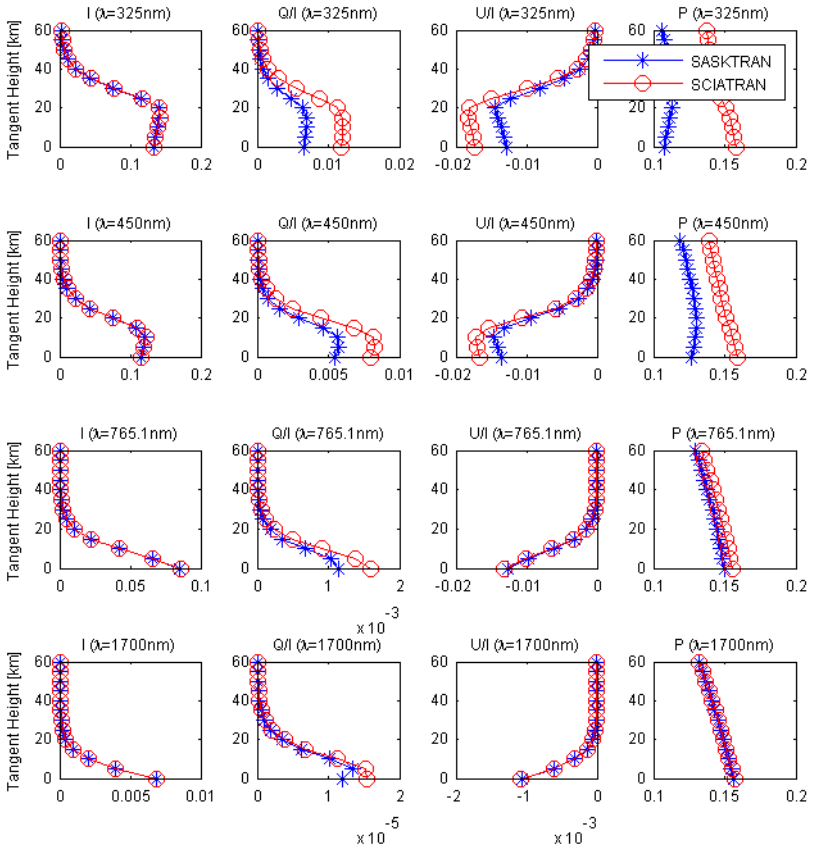

Figure 4.11: The polarized multiple scatter radiative transfer results for $\varsigma = 22.23°$ and $\varpi = 77.77°$ at varying wavelengths

shows a visible decrease for low wavelengths compared to single scatter as predicted.

The differences between SCIATRAN's and SASKTRAN's multiple scatter results are illustrated more clearly by the plots of $\delta I/I_{\text{SCIA}}$, $\delta q/q_{\text{SCIA}}$, $\delta u/u_{\text{SCIA}}$, and $\delta p/p_{\text{SCIA}}$ in Figure 4.12. This figure shows that the difference between the two models becomes smaller as the wavelength increases. Like the altitude of the radiance peak as described in Section 4.2 this effect is also because the Rayleigh cross section decreases as wavelength increases and therefore the probability of scattering drops significantly. The final observed radiance at long wavelengths depends mostly on the first order of scattering and as was shown in the previous section the single scatter results from the polarized SCIATRAN and SASKTRAN show very good agreement.

The plots for the shorter two wavelengths clearly show systematic differences between SASKTRAN and SCIATRAN's q, u, and p parameters. Employing accurate

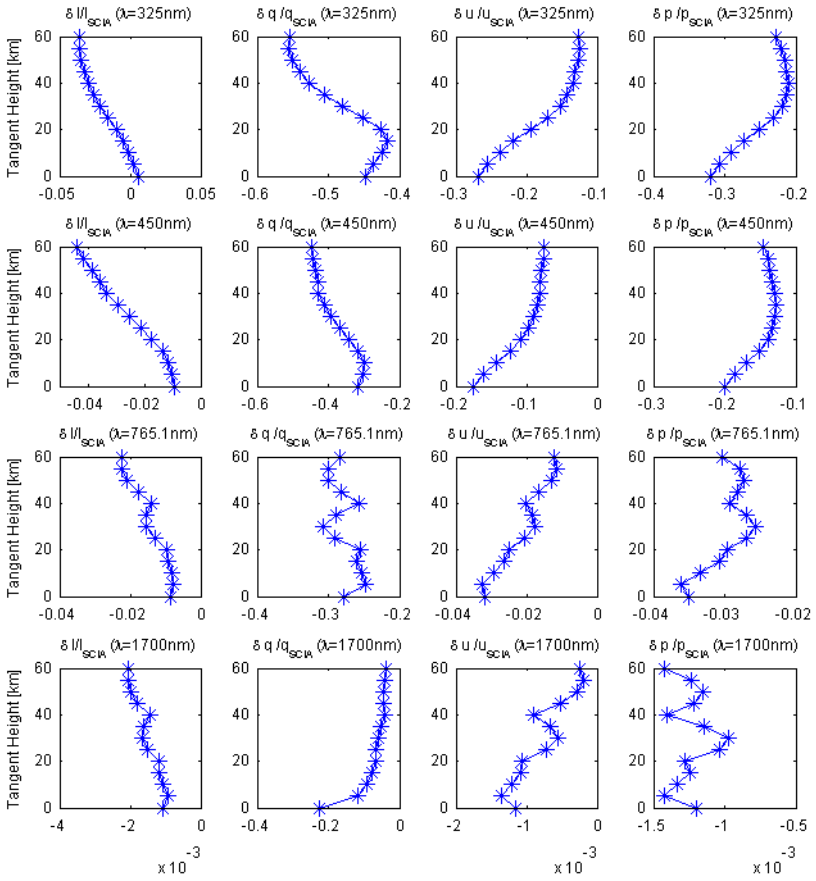

Figure 4.12: The normalized difference in polarized multiple scatter radiative transfer results for $\varpi = 22.23°$ and $\varsigma = 77.77°$ at varying wavelengths

geometries while calculating scattering functions and interpolating source terms and radiance is always important in radiative transfer. Its significance is even greater for polarized calculations. Minute differences in the polarization reference plane, described in Section 2.4, lead to drastically different Stokes Vectors. This is illustrated by examining the the rotation matrix from Section 2.3.4,

$$\underline{\mathbf{R}}(\eta) = \begin{bmatrix} 1 & 0 & 0 & 0 \\ 0 & \cos 2\eta & \sin 2\eta & 0 \\ 0 & -\sin 2\eta & \cos 2\eta & 0 \\ 0 & 0 & 0 & 1 \end{bmatrix}, \tag{4.3}$$

which shows that differences in directional information, and therefore in the rotation angle η, introduce nonlinear differences in the Stokes Vectors. These differences would

be propagated during the interpolation between different Stokes Vectors or during their integration. These effects are likely compounded in each order while using the method of successive orders of scattering. SCIATRAN and SASKTRAN rely on different approximations for higher order scattering which will produce different geometry based errors.

SCIATRAN uses multiple plane parallel atmospheres with different SZAs to approximate different SZAs around a spherical Earth. So if multiple scatter rays for SASKTRAN and SCIATRAN were compared directly it would be clear that they are traced through the atmospheric layers differently. A simple example of the differences introduced through this scheme is the paths taken by solar rays with large SZAs as depicted in Figure 4.13.

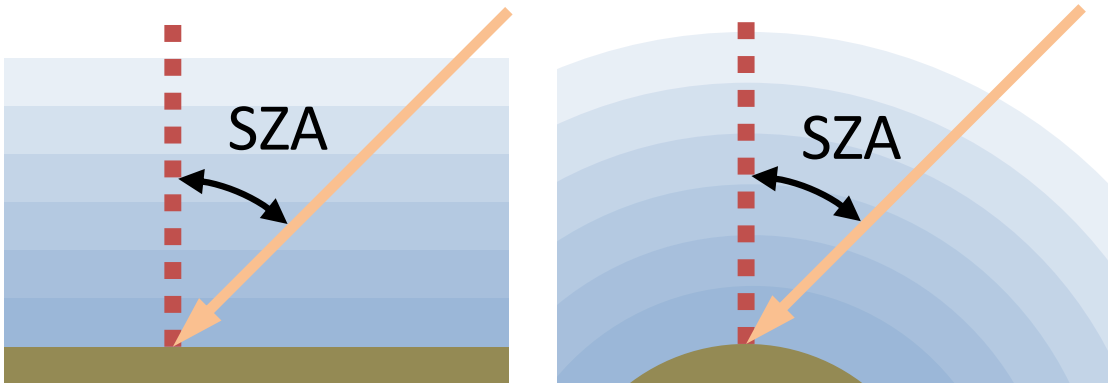

Figure 4.13: In SCIATRAN the plane parallel approximation for multiple scattering will trace rays through the atmosphere differently, for example solar rays at large SZA travel through more atmosphere than on a sphere.

Conversely the vector SASKTRAN uses spherical geometry for all orders of scattering but uses only a single Diffuse Profile. This will produce more accurate path lengths rays but introduces an additional problem. As the Diffuse Profile is translated around the surface of the Earth to supply the outbound source terms each DSP is rotated. Each outbound source vector, $\underline{J}$, is stored within its DSP with a reference direction that lies in the solar plane as described in Section 2.5.1. Due to the rotation of the DSP the Stokes reference direction has changed and will lead to inaccuracies while integrating along the line of sight.

The combination of the geometrical approximations within both models is likely

the source of the disagreement between the two. More figures comparing SCIATRAN and SASKTRAN multiple scatter results for different viewing geometries are included in Appendix B. The results are similar to those depicted above; the vector SASKTRAN and SCIATRAN models produce results that follow similar trends but display systematic differences for shorter wavelengths.

4.4 SASKTRAN Aerosol Comparisons

As explained in Section 1.1 aerosols, such as the suspended ice crystals that make up cirrus clouds and the SSA that make up the Junge layer, are of great interest to the atmospheric science community. Their abundance and composition are affected by human activity and they have wide reaching effects whose extent is currently unknown. Additional tools and methods are required to better understand the links between human activity, these aerosols, and their consequences. One such tool is a RTM that performs polarized calculations and this served as the primary motivation for the development of a vector SASKTRAN.

SASKTRAN is currently used as the forward model in the SaskMART retrieval algorithm at the University of Saskatchewan to produce SSA extinction values from OSIRIS measurements. The introduction of a vector SASKTRAN will make it possible for future work that falls outside the scope of this project to improve the already successful aerosol retrievals. With this expected use in mind it is worth performing a preliminary comparison of the scalar and vector SASKTRAN results for an atmosphere that includes sulphate aerosol to evaluate the possible improvements that may now be available.

4.4.1 Comparison Input Conditions

The following comparisons between the scalar and vector modes of the modified SASKTRAN were made for a simulated OSIRIS scan. Standard climatologies for the Rayleigh atmosphere and ozone were used. Three different sulphate aerosol distributions and an aerosol free condition were simulated. This section will describe these conditions and viewing geometries.

The number density of the background atmosphere was obtained through the SASKTRAN climatology interface for a version of the Mass Spectrometer Incoherent Scatter model (MSIS-90). MSIS-90 is an empirical model of the temperature and composi-

tion of the atmosphere. Although monthly variability is not captured by the model, temperature data fits to a standard deviation of 3 K and pressure agrees to 2 percent (*Hedin*, 1991).

The volume mixing ratio (vmr) profile for ozone was obtained from a climatology produced by *McPeters et al.* (2007). It is based on data obtained from SAGE II and supplemented by data from the Microwave Limb Sounder. Balloon sonde data are used in altitudes below 10 km where SAGE II data does not extend. It consists of monthly average ozone profiles for 10° latitude zones and 1 km altitude bins from 0 km to 60 km. SASKTRAN uses this data along with MSIS-90 to calculate ozone scale heights and extrapolate ozone vmr values above 60 km as well.

The aerosol distributions used in the following comparisons are based on the mean bimodal aerosol profiles presented by *Thomason* (2006), which were based on the repeated in situ measurements taken by *Deshler et al.* (2003). The measurements were split into two periods, 1992-1995 and 1995-2003, showing sulphate aerosol profiles under the influence of the Pinatubo eruption and then showing profiles after Pinatubo's influence declines. The measurements for the first time period show a small particle mode between about 0.03 μm and 0.1 μm with a number density profile that peaks above 10 cm^{-3}; a larger particle size mode with a radius of about 0.5 μm and a number density profile that peaks around 1 cm^{-3} is also present. As the effects of Pinatubo subside in the second time period the smaller particle mode's radius drops slightly to about 0.03 μm and 0.08 μm and the larger particle mode's radius drops to about 0.3 μm. The number density profile for the smaller mode appears to have changed very little; however the larger particle mode drops by a full order of magnitude.

The standard aerosol condition shown in Figure 4.14 is based on the small particle mode of the second time period as this profile would dominate during time periods devoid of volcanic activity. The number density profile shown peaks just above 10 cm^{-3} along with mode radius of 0.08 μm and mode width of 1.6 μm in a log-normal particle size distribution. The low aerosol condition uses the same size parameters but with a number density profile that is scaled to 1/20 of the the standard profile.

The volcanic condition is based on the large particle mode of the first time period presented by Thomason which would dominate for periods after volcanic activity. It uses a log normal particle size distribution of 0.5 μm with a mode width of 1.2 μm. The volcanic number density distribution is scaled to be 1/10 of the standard profile; which, as shown by Thomason, would be expected during volcanic periods. Eruptions

inject large radius aerosol into the atmosphere where its scattering effects overwhelm those of the smaller radius particles of the background distribution. These profiles are all shown in Figure 4.14.

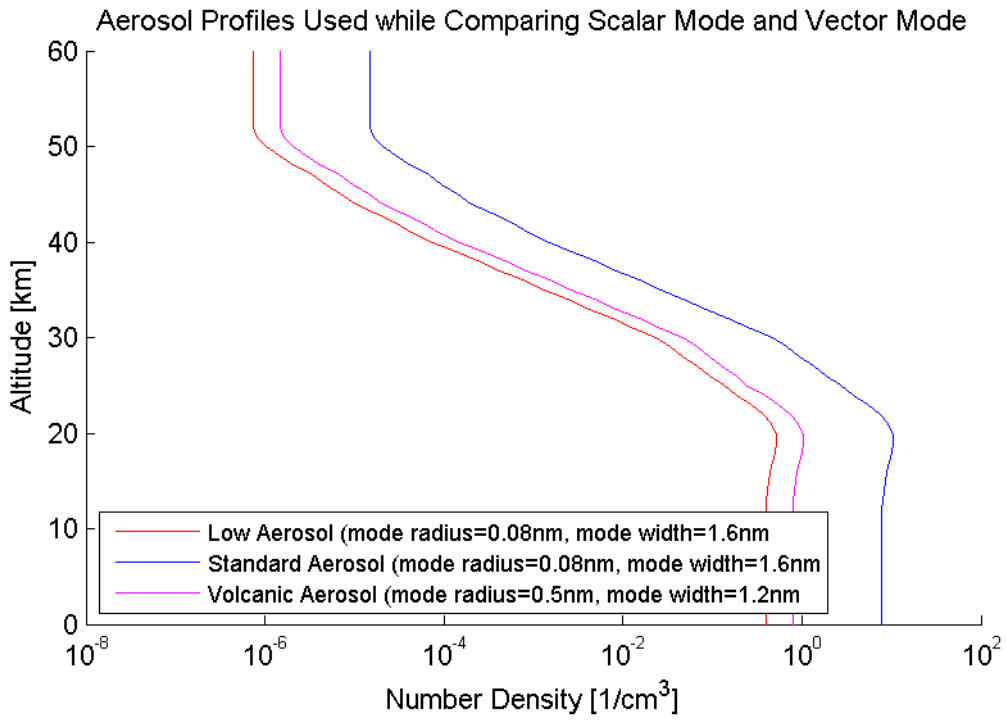

Figure 4.14: Sample aerosol profiles were generated based on aerosol distributions presented by *Thomason* (2006). The low aerosol peak number density peak is $1/20^{th}$ of the standard condition's peak and has identical mode radii and widths. The simulated volcanic condition has a number density peak $1/10^{th}$ of the standard condition's peak but uses a larger mode radii and smaller mode width.

The observer location, look direction, and solar position were all configured to match an OSIRIS limb scan. The Modified Julian Dates (MJDs) that would correspond to OSIRIS exposures throughout a scan are listed in the final column of Table 4.1. The observer position and look direction are listed in the first 6 columns of the table and are provided in Earth Centered Inertial (ECI) coordinates. The ECI system is a Cartesian coordinate system with the origin at the Earth's center, the z axis parallel to the north pole, and the x axis aligned with the prime meridian. The parameters from the climatologies described above, the line of sight trajectories, the local curvature of the Earth as described in Section 4.1.1, and the solar position were based on this information.

Observer Position [km]			Look Direction [unitless]			MJD
X	Y	Z	X	Y	Z	[days]
1741.1	-577.2	6720.8	0.4768	-0.6607	-0.5798	52393.385933
1769.9	-613.2	6710.1	0.4726	-0.6578	-0.5864	52393.386005
1787.9	-635.8	6703.2	0.4700	-0.6560	-0.5906	52393.386050
1802.0	-653.5	6697.7	0.4679	-0.6546	-0.5938	52393.386085
1815.6	-670.6	6692.4	0.4659	-0.6532	-0.5969	52393.386120
1829.7	-688.3	6686.8	0.4638	-0.6517	-0.6002	52393.386155
1843.8	-706.2	6681.0	0.4616	-0.6502	-0.6034	52393.386191
1859.8	-726.4	6674.4	0.4592	-0.6486	-0.6071	52393.386231
1872.1	-742.0	6669.2	0.4573	-0.6472	-0.6099	52393.386262
1887.0	-760.9	6662.9	0.4550	-0.6456	-0.6133	52393.386300
1901.4	-779.2	6656.7	0.4528	-0.6440	-0.6166	52393.386336
1915.5	-797.1	6650.6	0.4506	-0.6425	-0.6198	52393.386372
1929.3	-814.8	6644.4	0.4485	-0.6409	-0.6229	52393.386407
1942.8	-832.1	6638.4	0.4463	-0.6394	-0.6260	52393.386442
1957.1	-850.5	6631.8	0.4441	-0.6378	-0.6293	52393.386479
1970.9	-868.2	6625.5	0.4419	-0.6362	-0.6324	52393.386514
1984.1	-885.2	6619.3	0.4398	-0.6347	-0.6354	52393.386548
1997.3	-902.2	6613.0	0.4377	-0.6332	-0.6384	52393.386582
2010.2	-918.8	6606.8	0.4356	-0.6316	-0.6413	52393.386615
2023.3	-935.8	6600.4	0.4335	-0.6301	-0.6443	52393.386649
2036.7	-953.2	6593.8	0.4313	-0.6285	-0.6473	52393.386684
2050.6	-971.3	6586.9	0.4290	-0.6268	-0.6504	52393.386720
2064.2	-989.0	6580.0	0.4268	-0.6251	-0.6535	52393.386755
2077.3	-1006.0	6573.3	0.4247	-0.6235	-0.6564	52393.386789
2090.5	-1023.4	6566.5	0.4225	-0.6219	-0.6594	52393.386824
2103.5	-1040.4	6559.7	0.4204	-0.6203	-0.6622	52393.386858

Table 4.1: The parameters used to simulate an OSIRIS scan. The observer position and look direction are recorded in ECI coordinates.

4.4.2 Simulated OSIRIS Spectra

The input conditions described in the preceding section were used for both the scalar and vector modes of SASKTRAN to simulate limb scattered measurements at the wavelengths OSIRIS measures. Equation 1.6 and the factors shown in Figure 1.4, which provide corrections for the spectrograph's Woods anomalies, were applied to the vector output from the simulation to obtain the corrected normalized radiance. Figures 4.15 to 4.18 show the scalar mode and corrected vector results. Only every second OSIRIS exposure is shown between 6 km and 50 km to reduce the clutter in the figures.

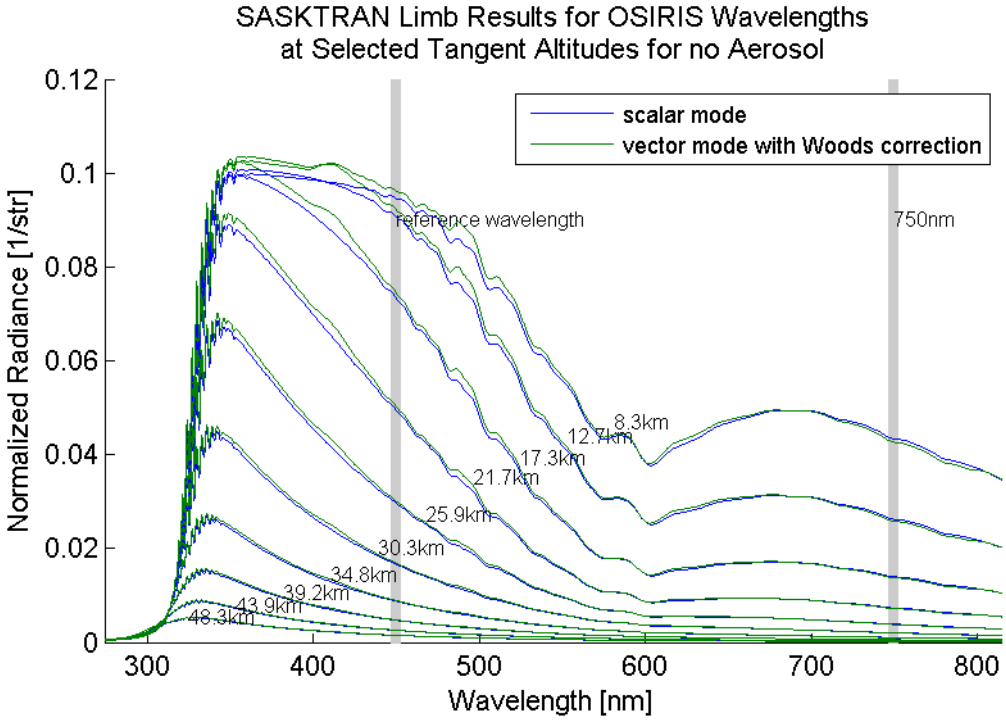

Figure 4.15: A comparison of the scalar and corrected vector SASKTRAN results for the aerosol free condition

Differences between scalar and corrected vector results are visible in all four cases depicted in these figures. All display greater values in the corrected vector results for wavelengths shorter than approximately 700 nm and a lower normalized radiance for longer wavelengths. Examining Figure 1.4 reveals that this roughly corresponds to the wavelength where the Q component of the Stokes Vector becomes more influential than the U component on the corrected radiance.

It is worth noting that from these plots alone it is difficult to distinguish the effects

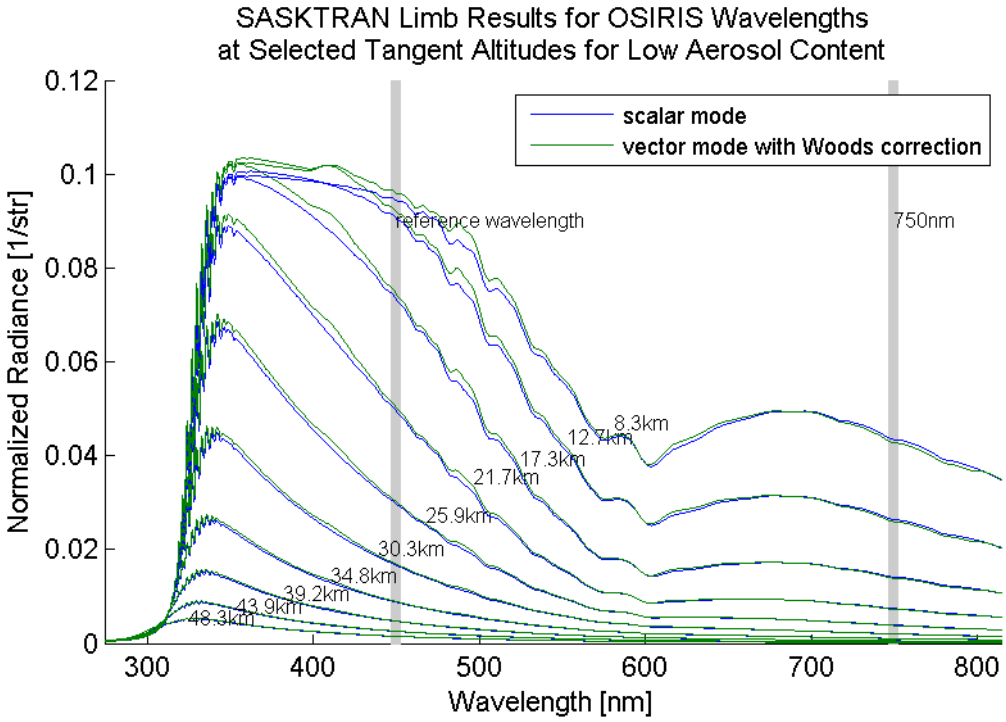

Figure 4.16: A comparison of the scalar and corrected vector SASKTRAN results for the low aerosol condition.

of changing the number density for the smaller sulphate aerosol mode width. The first three figures which represent the no aerosol, low aerosol, and standard aerosol number density profiles are nearly indistinguishable. However Figure 4.18 is visibly distinguishable from the others as the deviation between the scalar and corrected vector normalized radiance is smaller, especially at longer wavelengths. This figure stands out despite having a number density profile between two of the previous cases, indicates the mode radius of the particle size distribution has a strong influence over the polarization corrections.

4.4.3 Simulated SaskMART Aerosol Retrieval Vectors

Another way of estimating the effects the corrected vector SASKTRAN results will have on aerosol retrievals is to construct simulated retrieval vectors that would be used in the SaskMART retrieval algorithm. Equation 1.9 results in a parameter that compares the signal at an aerosol-sensitive wavelength to an aerosol-insensitive wavelength. These wavelengths are marked by vertical lines in grey on Figures 4.15 to 4.18. The equation is also normalized to a single altitude and uses the aerosol free calculation to screen

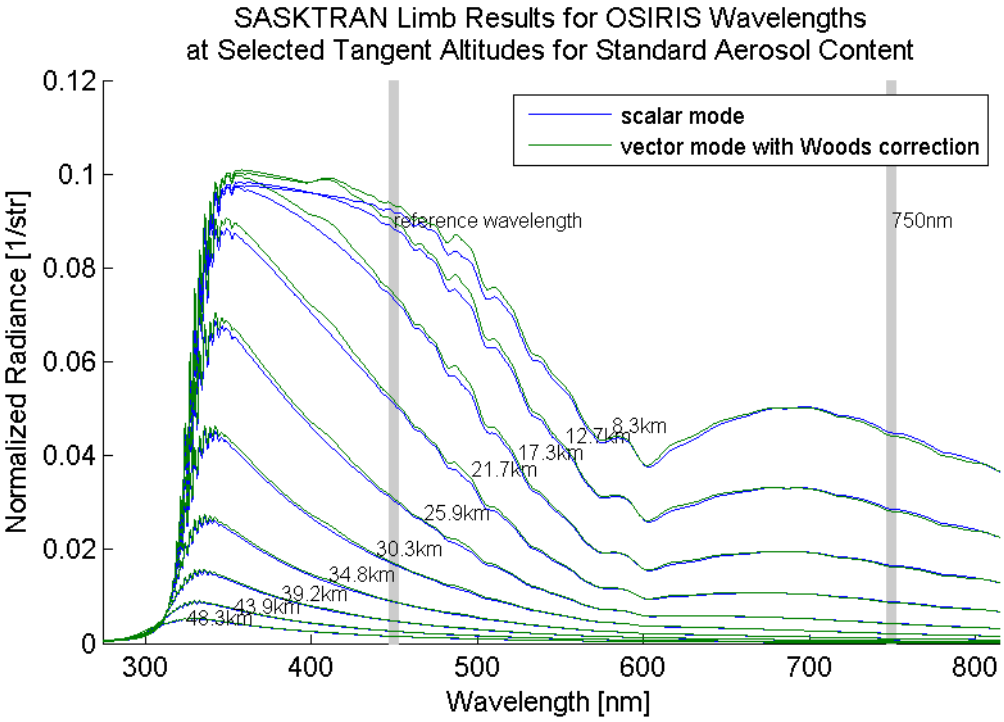

Figure 4.17: A comparison of the scalar and corrected vector SASKTRAN results for the standard aerosol condition

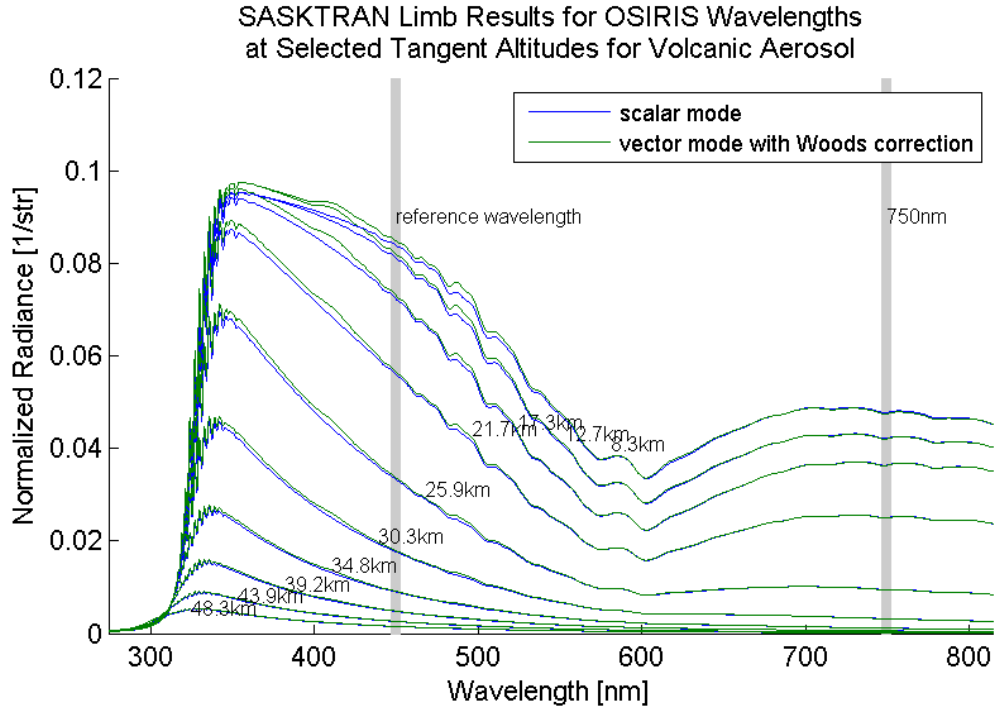

Figure 4.18: A comparison of the scalar and corrected vector SASKTRAN results for the volcanic condition.

the effects of other atmospheric variables. The scalar and vector results for all three aerosol cases described above were used to obtain the retrieval vectors shown in Figure 4.19. The simulated measurement with a tangent point nearest 35 km was used as the reference altitude and is indicated by a grey horizontal line on Figure 4.19.

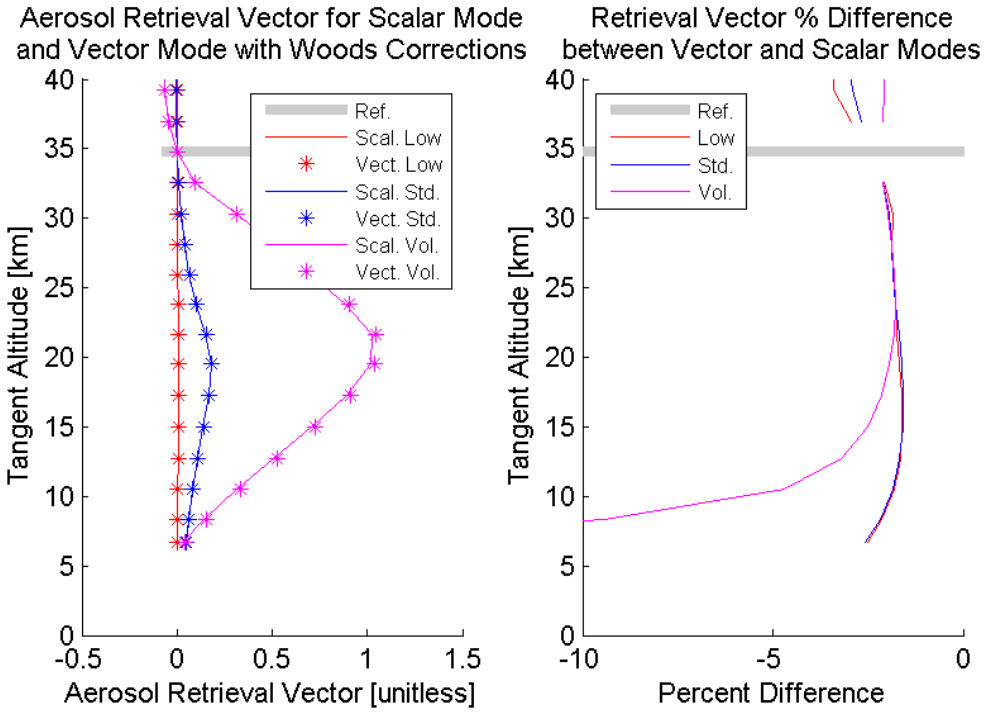

Figure 4.19: Simulated retrieval vectors for low aerosol, standard aerosol and volcanic aerosol conditions (left). The percent difference between scalar and corrected vector calculations are shown on right.

The percent difference between the polarized retrieval vector and the scalar retrieval vector is shown on the right for each of the aerosol cases. These differences reveal that for conditions with standard aerosol particle sizes, as is the case for the Low and Standard cases, the vector calculations with Wood's corrections only result in a small difference in the retrieval vector, of around 2 percent. For the volcanic case where the number density profile actually lies between the other two cases the percent difference is much larger at low altitudes, exceeding 10 percent. This larger deviation must be attributed to the much larger particle sizes used in the volcanic case.

These comparisons indicate that the current retrieval process for aerosol extinction employed at the University of Saskatchewan is not greatly hindered by its lack of polarized radiative transfer calculations with Wood's corrections. For standard aerosol conditions it seems that polarization only has a small affect on the retrieval vector and

likely would only provide small corrections to aerosol retrievals. However the larger percent difference for the volcanic case indicates that under those conditions ignoring polarization may significantly affect aerosol retrievals.

Chapter 5

Summary and Outlook

Remote sensing in the atmosphere is vitally important to understanding the details of atmospheric processes and anthropogenic sources of atmospheric change. RTMs serve as forward models in retrieval processes and therefore are critical for measuring processes and constituents of interest.

The SASKTRAN RTM has served as a highly successful forward model for the retrieval of ozone and aerosol data from limb scattered spectra measured by OSIRIS. Both of these atmospheric constituents are influenced by human activity and affect the future of the environment. Previous versions of SASKTRAN and the retrieval process have ignored polarization induced by scattering and the Wood's anomalies that exist in OSIRIS optics. Sulphate aerosol retrievals are likely affected by this limitation as the Wood's anomalies act on the wavelengths used for the retrieval vector. The retrievals are also affected the wavelengths used in its retrieval vector were selected partially to reduce polarization sensitivity rather than maximizing aerosol sensitivity and because cirrus clouds, which currently affect retrievals, may be identified in the future using polarization information. For these reasons there was a need for improvement.

This will improve the accuracy of current retrievals by taking advantage of scattering behaviors of different types and sizes of aerosols and by allowing for corrections of anomalies in optical devices. The goal of this thesis work was to develop a vector version of SASKTRAN that is capable of performing polarized radiative transfer calculations. Examining the results produced by the vector SASKTRAN indicate that this goal was achieved.

Stokes Vectors are mathematical constructs that describe the intensity and polarization state of light. As shown in Chapter 2 the Stokes Vectors, scattering phase

matrices, and rotation matrices can be derived from the basic principles of electromagnetism. In Section 2.4 these elements were all used to construct polarized radiative transfer equations which were suitable for implementation in SASKTRAN.

The vector version of SASKTRAN must be capable of performing non-polarized calculations as well to save computer resources and time for simulations that are not affected by polarization. The design of the vector SASKTRAN takes this requirement into account and minimizes the impact on non-polarized calculations wherever possible. In order to achieve these goals inheritance relationships were constructed between pre-existing classes and new polarized classes that provided identical interfaces while performing their respective tasks differently. In addition to that a system for storage, linkage, and communication of polarization information within the model was implemented that maintained the pre-existing interactions between classes. This was done without significantly increasing the overhead of SASKTRAN while in non-polarized operation.

Several different source term interpolation schemes were implemented and evaluated in this work as described in Section 3.2. Shepard's interpolation method, another modified version of that method, and a linear interpolation method were all compared. They all performed well and the Shepard method produced slightly better results than the others; however to obtain these improvements this interpolation scheme requires more initial information than linear interpolation. When the demand for this additional information is extended over the entire model the impact on memory and performance would be unacceptable for current desktop computers. Because of its superior efficiency the linear interpolation method was selected for the remainder of this work.

During the study of the interpolation methods it was noticed that all the interpolation methods performed poorly near the DSP's local z-axis. It was determined that this was because the position of each ray's reference plane varies rapidly with ray propagation directions in that region. A solution was implemented that rotated the Stokes Vectors prior to interpolation, which eliminated the issue as illustrated by Figure 3.13.

Once the initial conditions for results produced by the vector SCIATRAN were duplicated in the vector SASKTRAN their results for polarized calculations were compared. The single scatter results showed extremely good agreement. The normalized radiance showed less than half a percent difference and the normalized polarized parameters Q/I, U/I, and P differed by less than 0.0001%. The systematic differences displayed in the normalized radiance were likely due to rounding differences between

the models as they calculated line of sight intercepts with spherical atmospheric shells.

The multiple scatter results show a greater degree of systematic deviation between the vector SCIATRAN and vector SASKTRAN results. Shorter wavelengths display noticeably more deviation than the single scatter comparison but the longest wavelengths tested show less than 0.5% difference for normalized radiance. For multiple scatter calculations SCIATRAN uses a composite plane parallel atmosphere at varying SZAs while SASKTRAN uses a single Diffuse Profile that is translated around the globe. The combination of these geometrical approximations used within the two models is likely the source of this disagreement.

Despite these differences displayed by these comparisons the profiles generated by each model do follow similar trends and because aerosol retrievals are performed using longer wavelengths where they are in greater agreement the deviation between models would likely have a minimal impact on current retrievals. In the future it will be possible to improve upon the geometrical approximations applied in SASKTRAN by altering the system that was described in Section 4.3 which translates the Diffuse Profiles.

The vector and scalar mode of SASKTRAN were compared for three different aerosol conditions based on results presented by *Thomason* (2006). A concentration profile was generated for standard atmospheric conditions when there is no volcanic activity with a common particle mode radius and width and another was generated with the same mode radius and width for low concentrations. A third condition was simulated with significantly larger particle mode radius and width with a concentration 1/10 of the standard profile. This third condition matches the larger aerosol particle mode that dominates during periods of volcanic activity.

Because the vector calculations and scalar calculations produced very similar retrieval vectors for standard aerosol sizes simply applying the Wood's anomaly corrections with the vector SASKTRAN may only provide small improvements to the current retrieval accuracy. For the volcanic aerosol condition much larger differences were observed between the scalar and vector calculations.

Although alterations to SaskMART fall outside the scope of this work these comparisons point to some of the ways the vector SASKTRAN could be used to improve aerosol retrievals. Now it is possible to construct a retrieval vector using the 810 nm, wavelength light which is in a region of the OS spectra that was previously avoided because of the strong Wood's anomalies. This would immediately increase the retrieval's sensitivity to aerosol. The deviation in the volcanic condition's retrieval vectors indi-

cates that the vector model is required to accurately retrieve aerosol information for periods of strong volcanic activity. Based on this observation it may be possible to use the vector model to obtain information about the distribution as well, rather than retrieving aerosol extinction values alone, by creating a retrieval vector that includes both strong and weak polarization sensitive wavelengths. These observable differences based on changes in particle size distribution also imply that other aerosol types, like the non-spherical suspended ice particles that make up cirrus clouds, would also have a different signature in the polarized signal that may be used to differentiate aerosol types.

The vector SASKTRAN created through the thesis work presented here will serve as a valuable tool in the retrieval of atmospheric information from spectrographic data and contribute to a better understanding of the atmosphere.

Appendix A

Single Scatter Comparison Figures

The following figures compare single scatter results from the vector SCIATRAN and vector SASKTRAN RTMs and are discussed in Section 4.2. The figures are presented in pairs; each pair representing a different viewing geometry defined by the solar zenith angle (ς) and solar azimuth angle (ϖ) which are provided in the captions below each figure. These angles are explained in greater detail in Section 4.1.2.

The first figure in each pair shows normalized polarization parameters; one is shown in each column. They have been calculated for a normalized solar intensity and then Q and U were re-normalized to the radiance value at the same tangent altitude. These parameters are described in detail in Section 2.3.1. P is the degree of polarization and is defined by Equation 4.1. The second figure in each pair shows the normalized difference between the vector SCIATRAN and vector SASKTRAN results for the same viewing geometry. Like the previous figure each row will represent a wavelength but each column will represent the normalized difference between the parameters plotted in the previous figure.

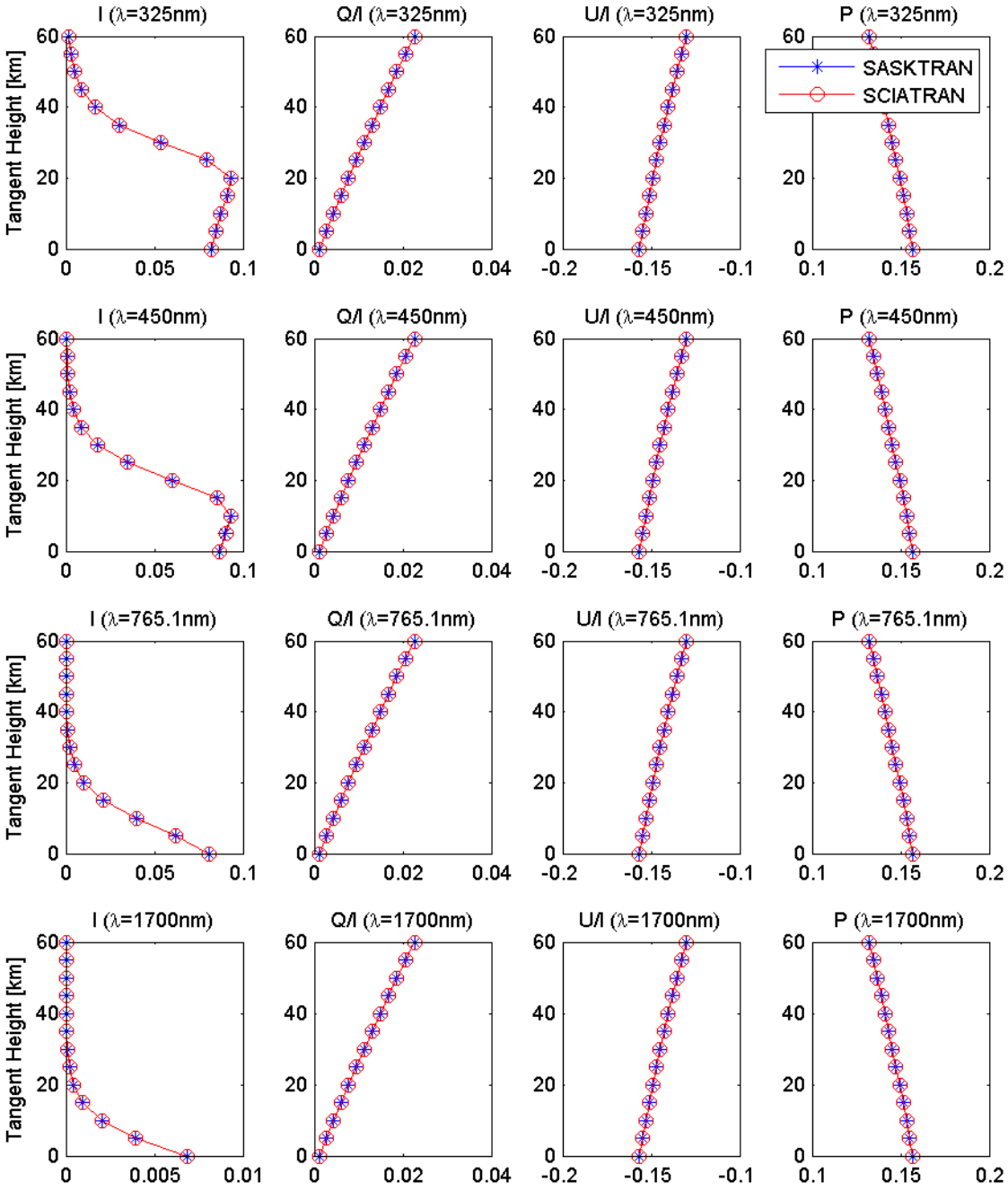

Figure A.1: The polarized single scatter radiative transfer results for $\varpi = 22.23°$ and $\varsigma = 77.77°$ at varying wavelengths

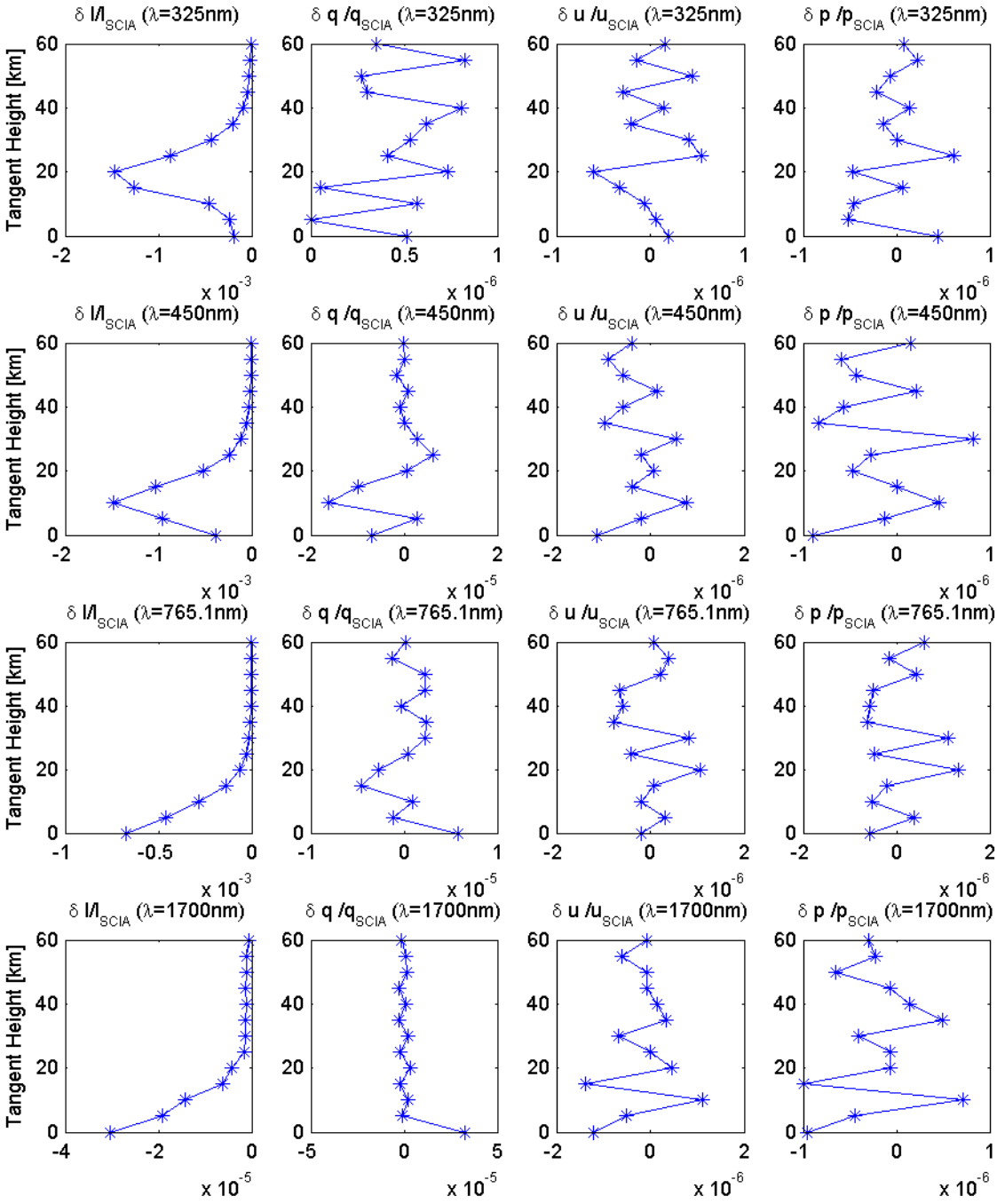

Figure A.2: The normalized difference in polarized single scatter radiative transfer results for $\varpi = 22.23°$ and $\varsigma = 77.77°$ at varying wavelengths

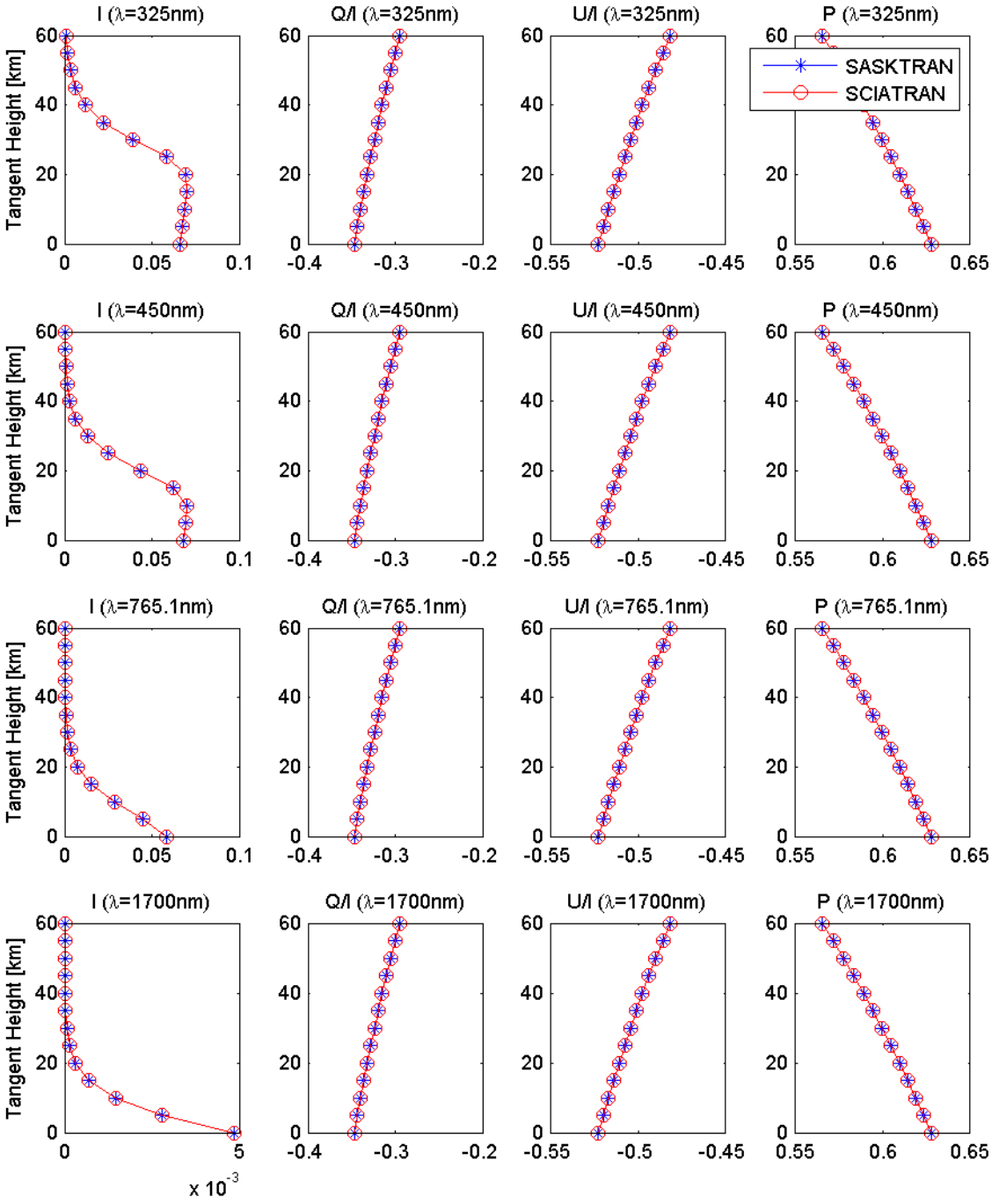

Figure A.3: The polarized single scatter radiative transfer results for $\varpi = 34.41°$ and $\varsigma = 47.30°$ at varying wavelengths

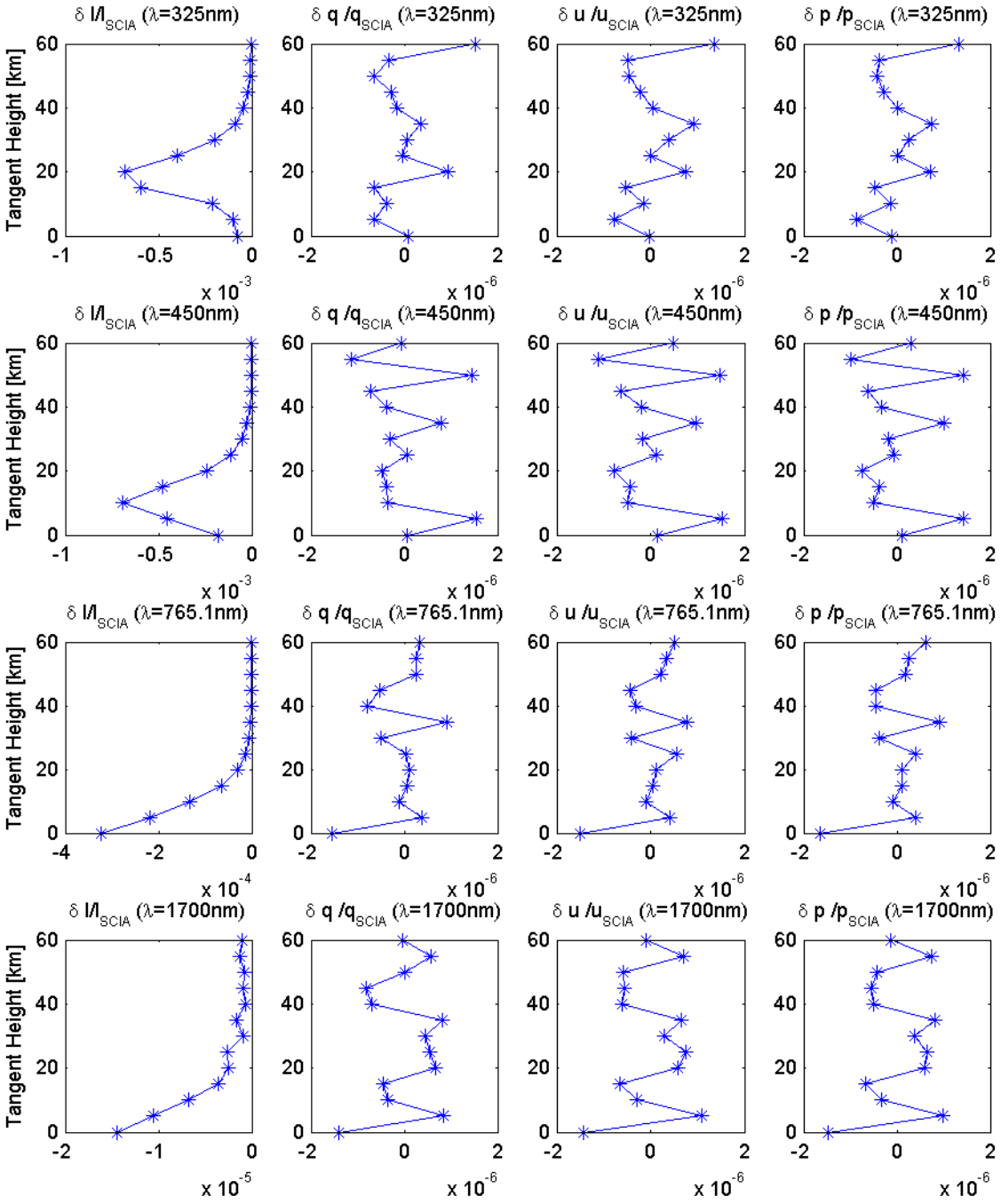

Figure A.4: The normalized difference in polarized single scatter radiative transfer results for $\varpi = 34.41°$ and $\varsigma = 47.30°$ at varying wavelengths

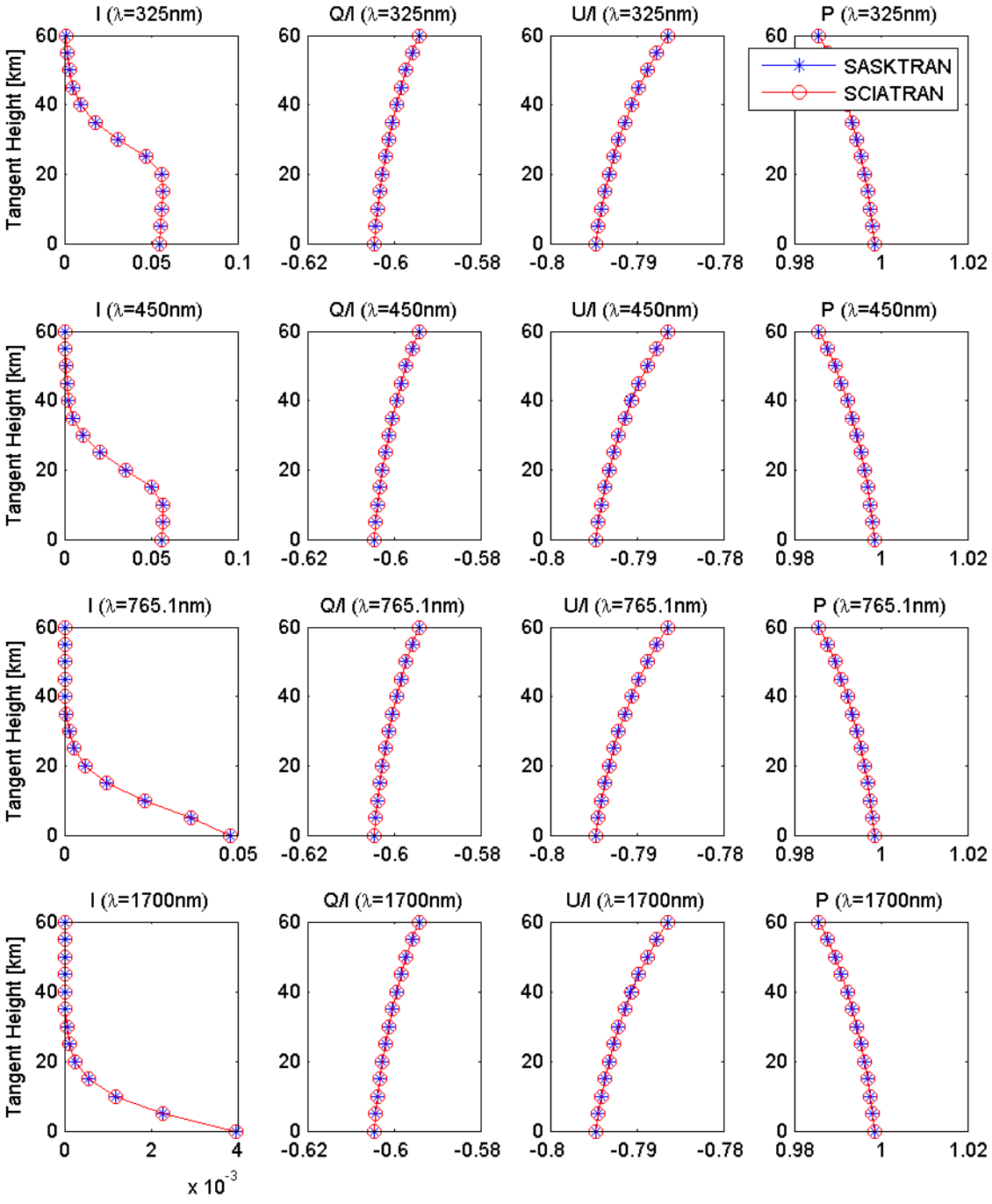

Figure A.5: The polarized single scatter radiative transfer results for $\varpi = 67.56°$ and $\varsigma = 28.71°$ at varying wavelengths

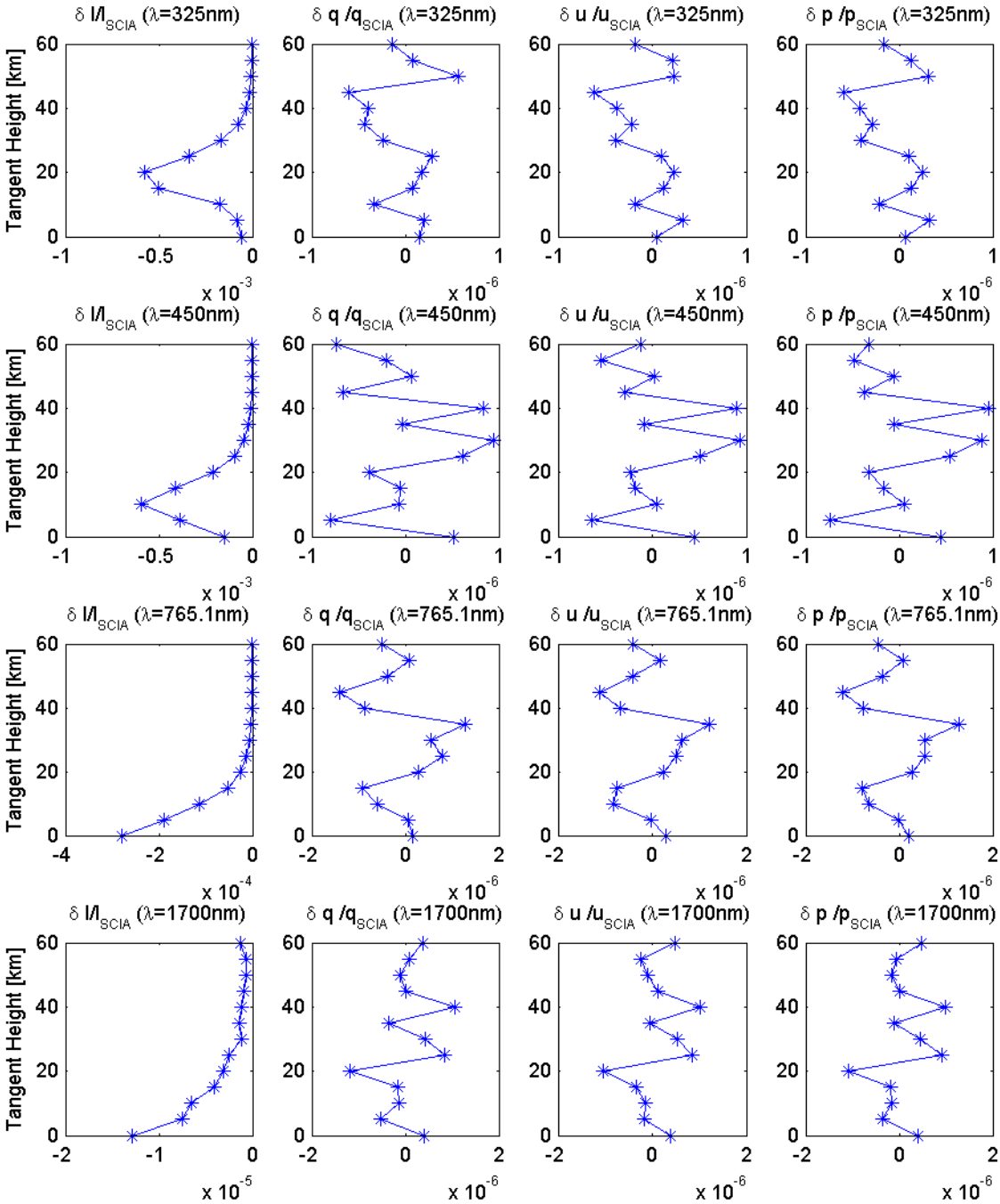

Figure A.6: The normalized difference in polarized single scatter radiative transfer results for $\varpi = 67.56°$ and $\varsigma = 28.71°$ at varying wavelengths

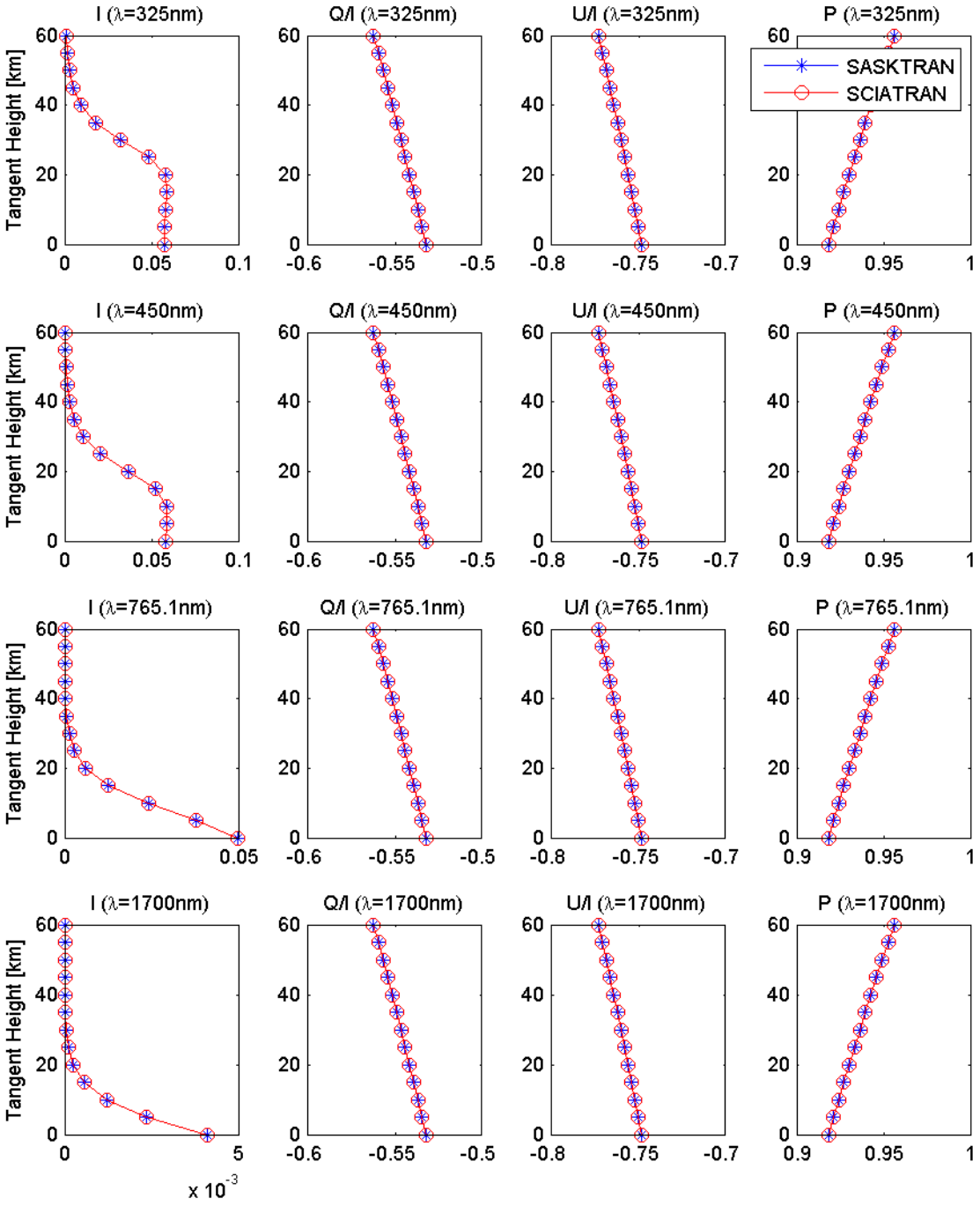

Figure A.7: The polarized single scatter radiative transfer results for $\varpi = 96.47°$ and $\varsigma = 26.84°$ at varying wavelengths

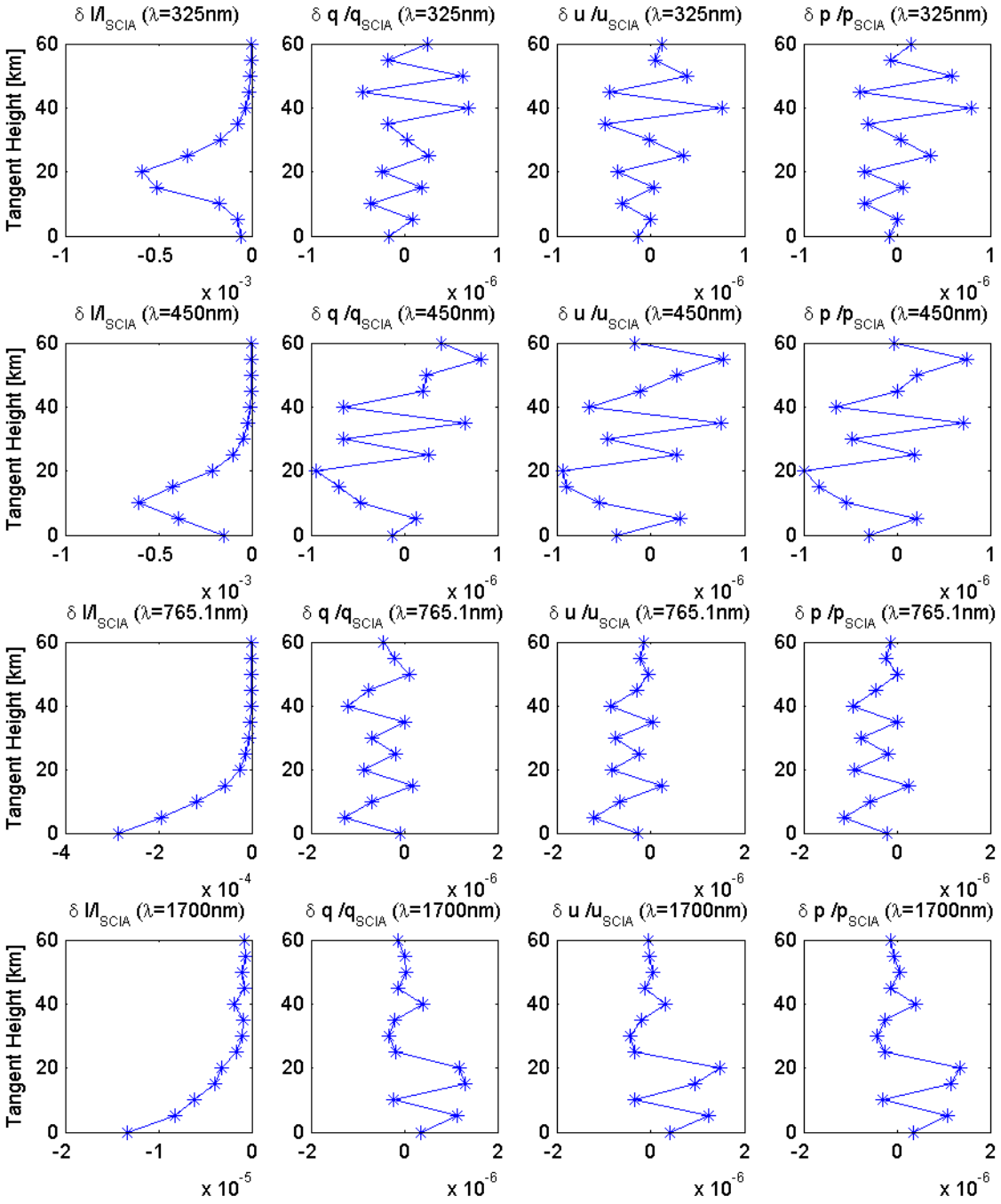

Figure A.8: The normalized difference in polarized single scatter radiative transfer results for $\varpi = 96.47°$ and $\varsigma = 26.84°$ at varying wavelengths

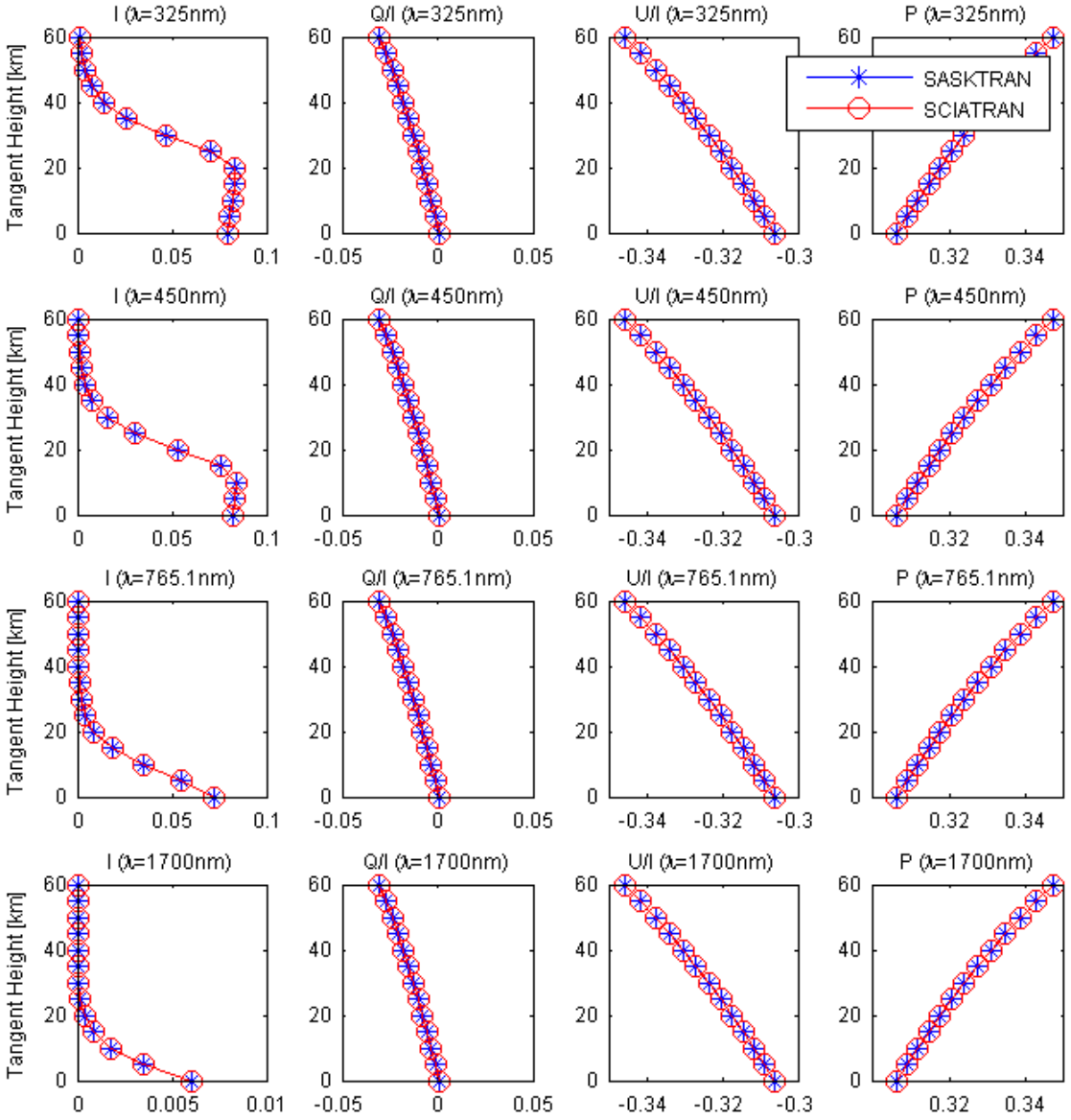

Figure A.9: The polarized single scatter radiative transfer results for $\varpi = 142.55°$ and $\varsigma = 52.88°$ at varying wavelengths

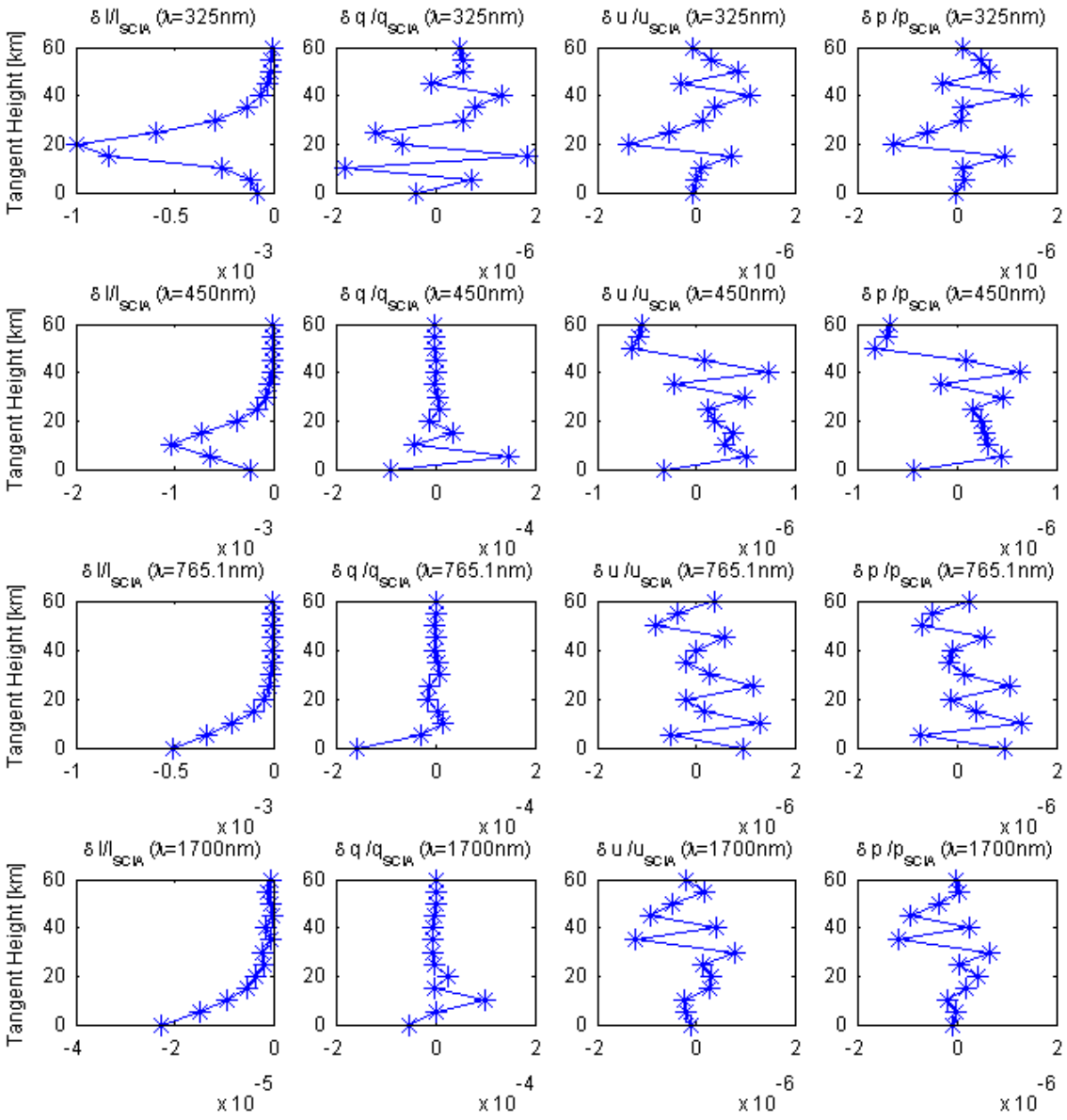

Figure A.10: The normalized difference in polarized single scatter radiative transfer results for $\varpi = 142.55°$ and $\varsigma = 52.88°$ at varying wavelengths

Appendix B

Multiple Scatter Comparison Figures

The following figures compare multiple scatter results from the vector SCIATRAN and vector SASKTRAN RTMs and are discussed in Section 4.3. The figures are presented in pairs; each pair representing a different viewing geometry defined by the solar zenith angle (ς) and solar azimuth angle (ϖ) which are provided in the captions below each figure. These angles are explained in greater detail in Section 4.1.2.

The first figure in each pair shows normalized polarization parameters; one is shown in each column. They have been calculated for a normalized solar intensity and then Q and U were re-normalized to the radiance value at the same tangent altitude. These parameters are described in detail in Section 2.3.1. P is the degree of polarization and is defined by Equation 4.1. The second figure in each pair shows the normalized difference between the vector SCIATRAN and vector SASKTRAN results for the same viewing geometry. Like the previous figure each row will represent a wavelength but each column will represent the normalized difference between the parameters plotted in the previous figure.

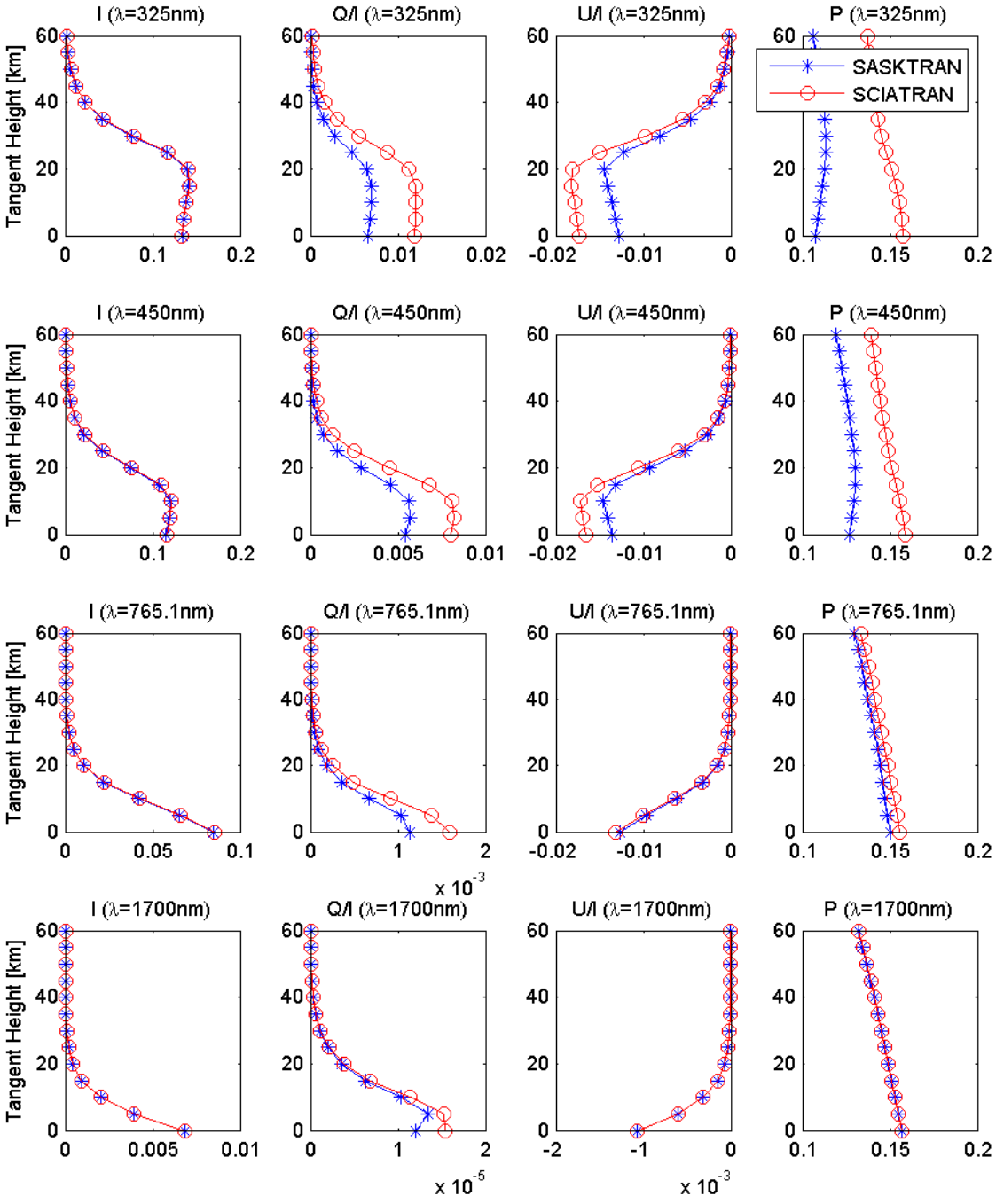

Figure B.1: The polarized multiple scatter radiative transfer results for $\varpi = 22.23°$ and $\varsigma = 77.77°$ at varying wavelengths

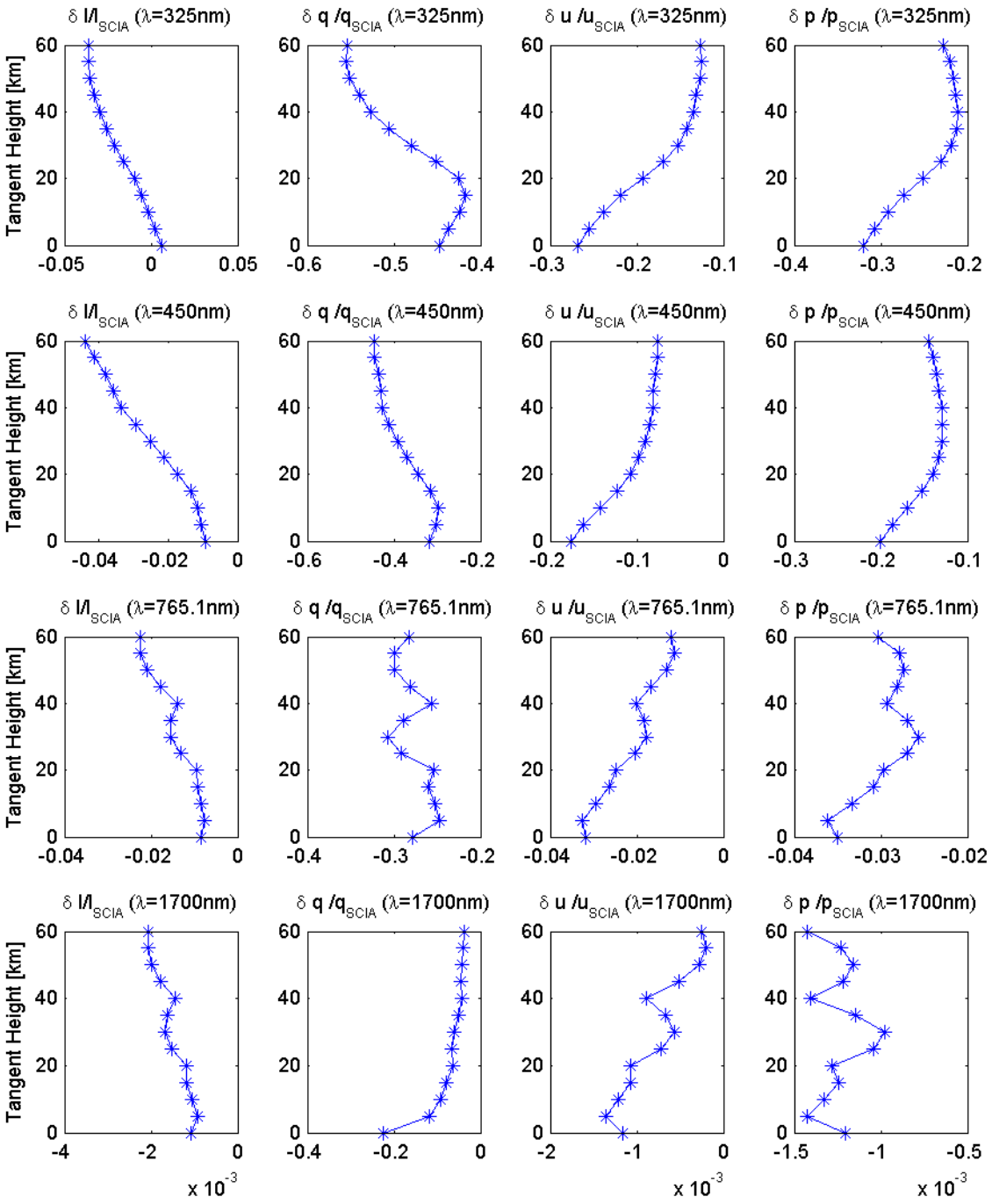

Figure B.2: The normalized difference in polarized multiple scatter radiative transfer results for $\varpi = 22.23°$ and $\varsigma = 77.77°$ at varying wavelengths

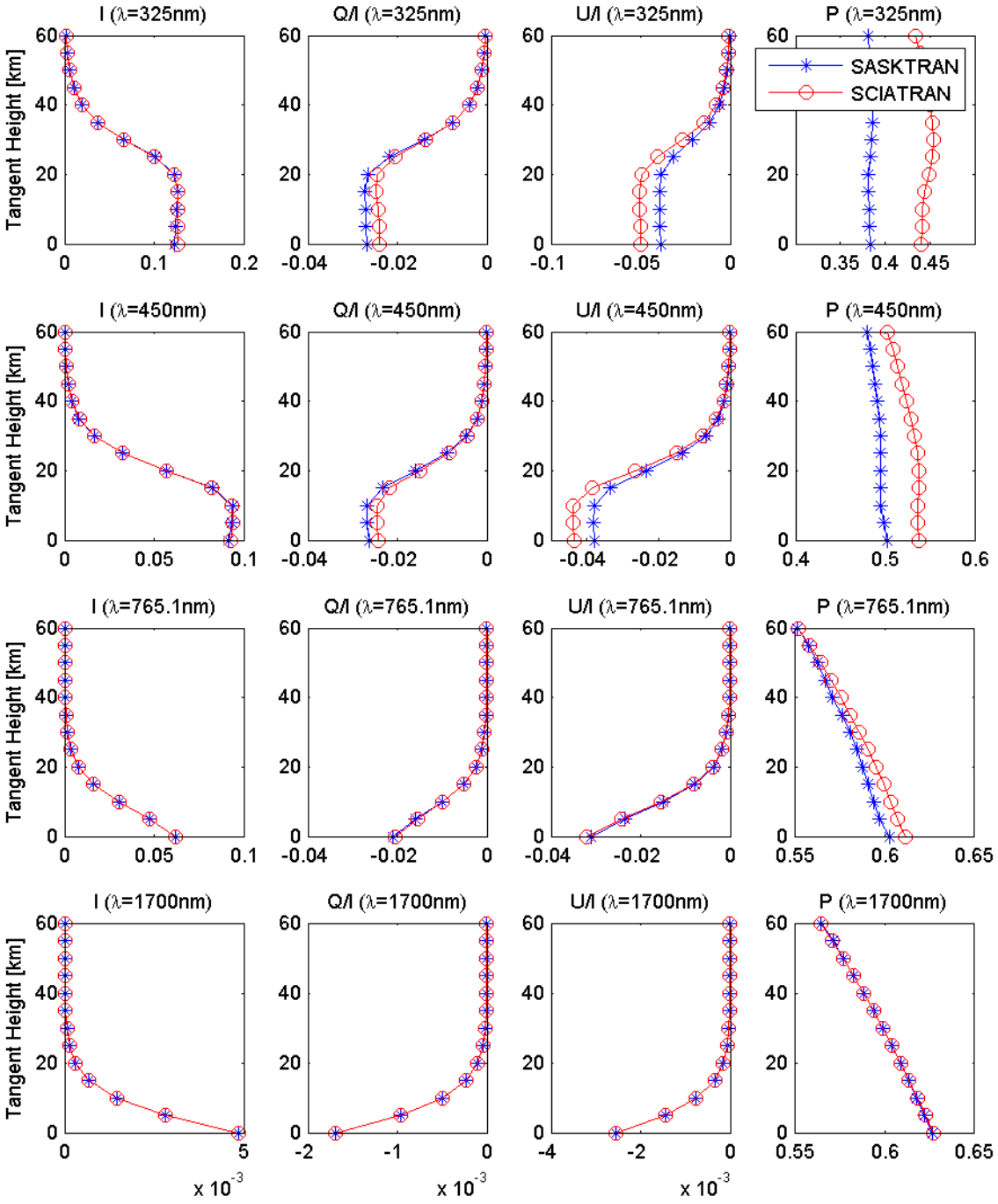

Figure B.3: The polarized multiple scatter radiative transfer results for $\varpi = 34.41°$ and $\varsigma = 47.30°$ at varying wavelengths

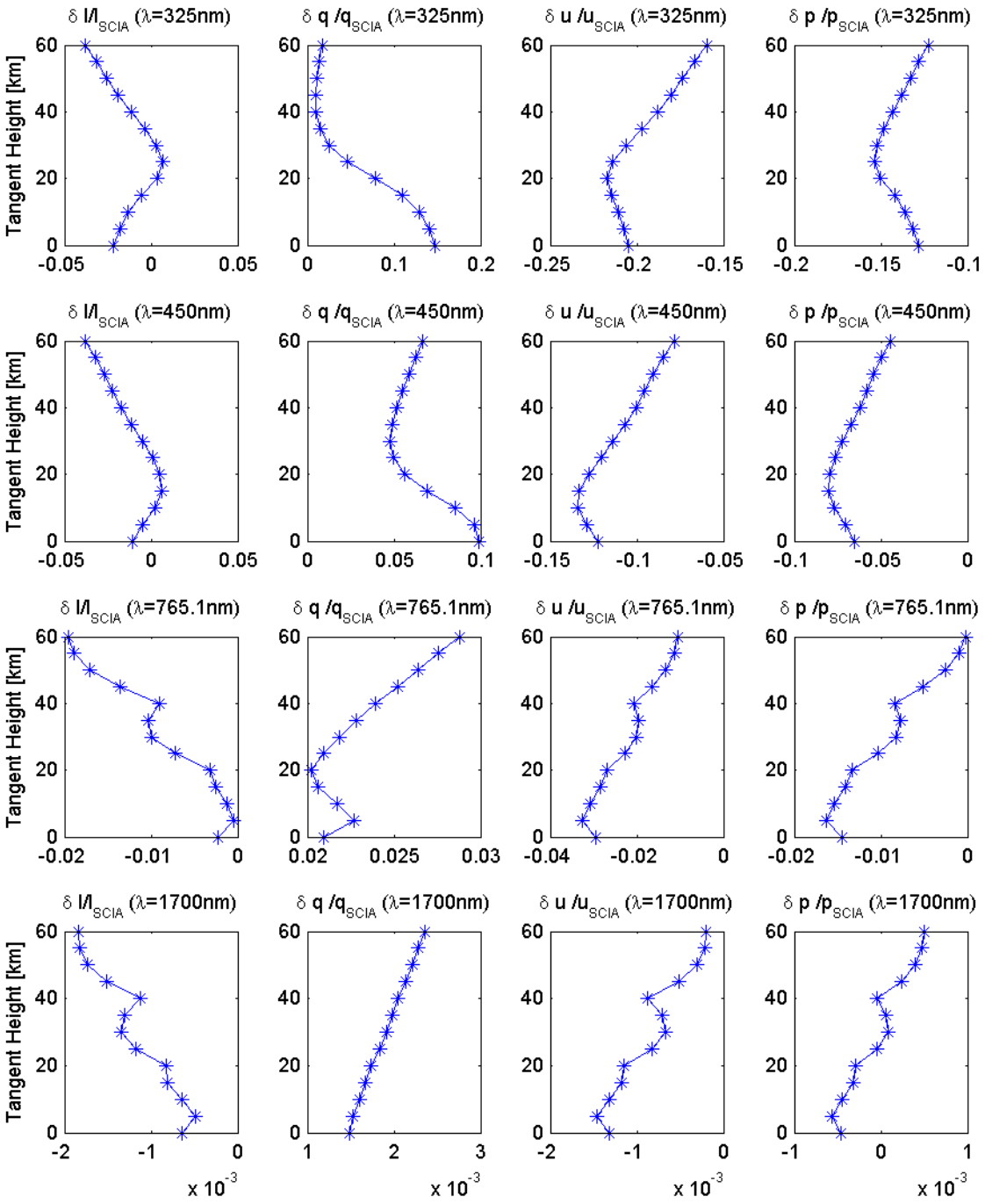

Figure B.4: The normalized difference in polarized multiple scatter radiative transfer results for $\varpi = 34.41°$ and $\varsigma = 47.30°$ at varying wavelengths

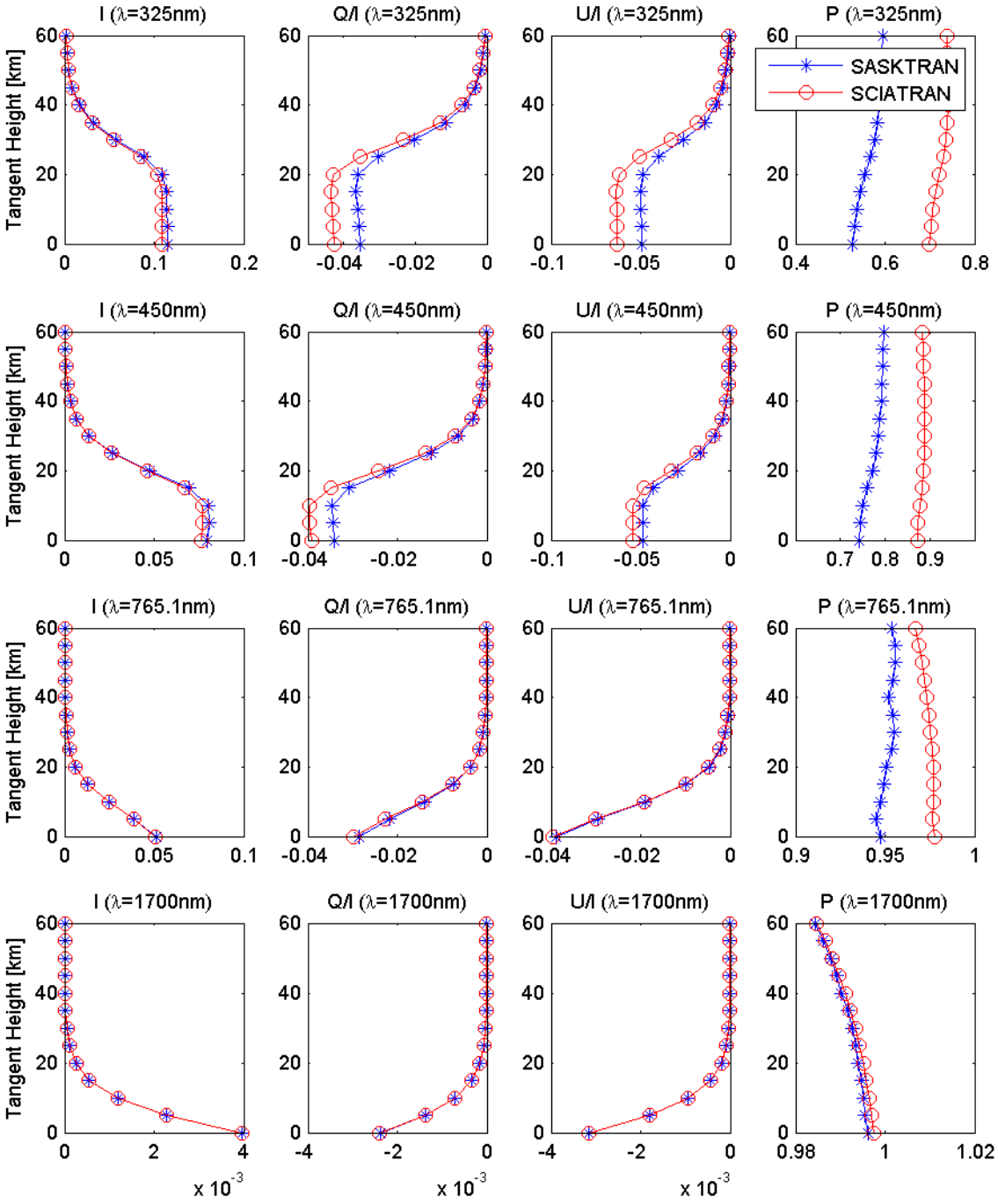

Figure B.5: The polarized multiple scatter radiative transfer results for $\varpi = 67.56°$ and $\varsigma = 28.71°$ at varying wavelengths

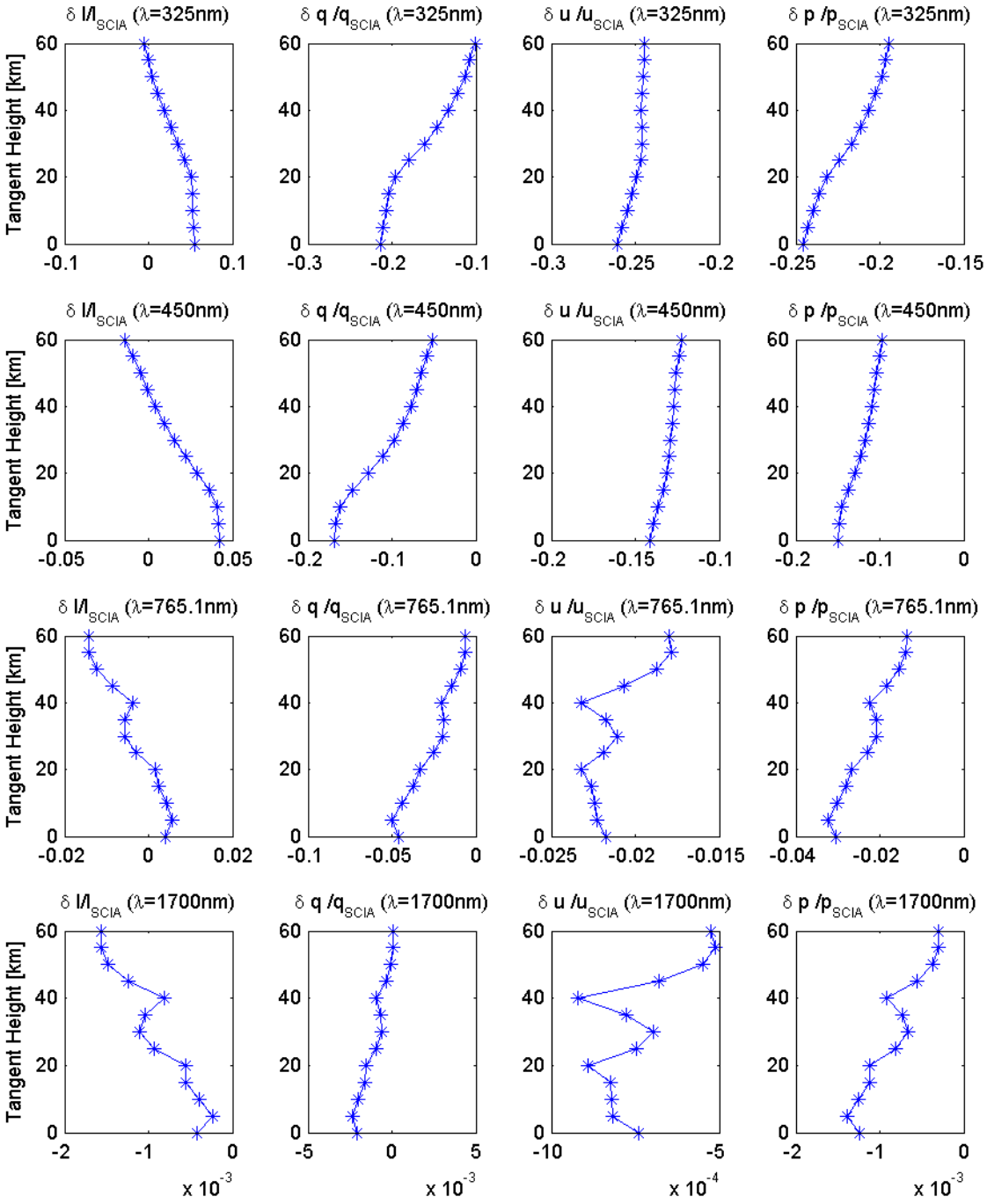

Figure B.6: The normalized difference in polarized multiple scatter radiative transfer results for $\varpi = 67.56°$ and $\varsigma = 28.71°$ at varying wavelengths

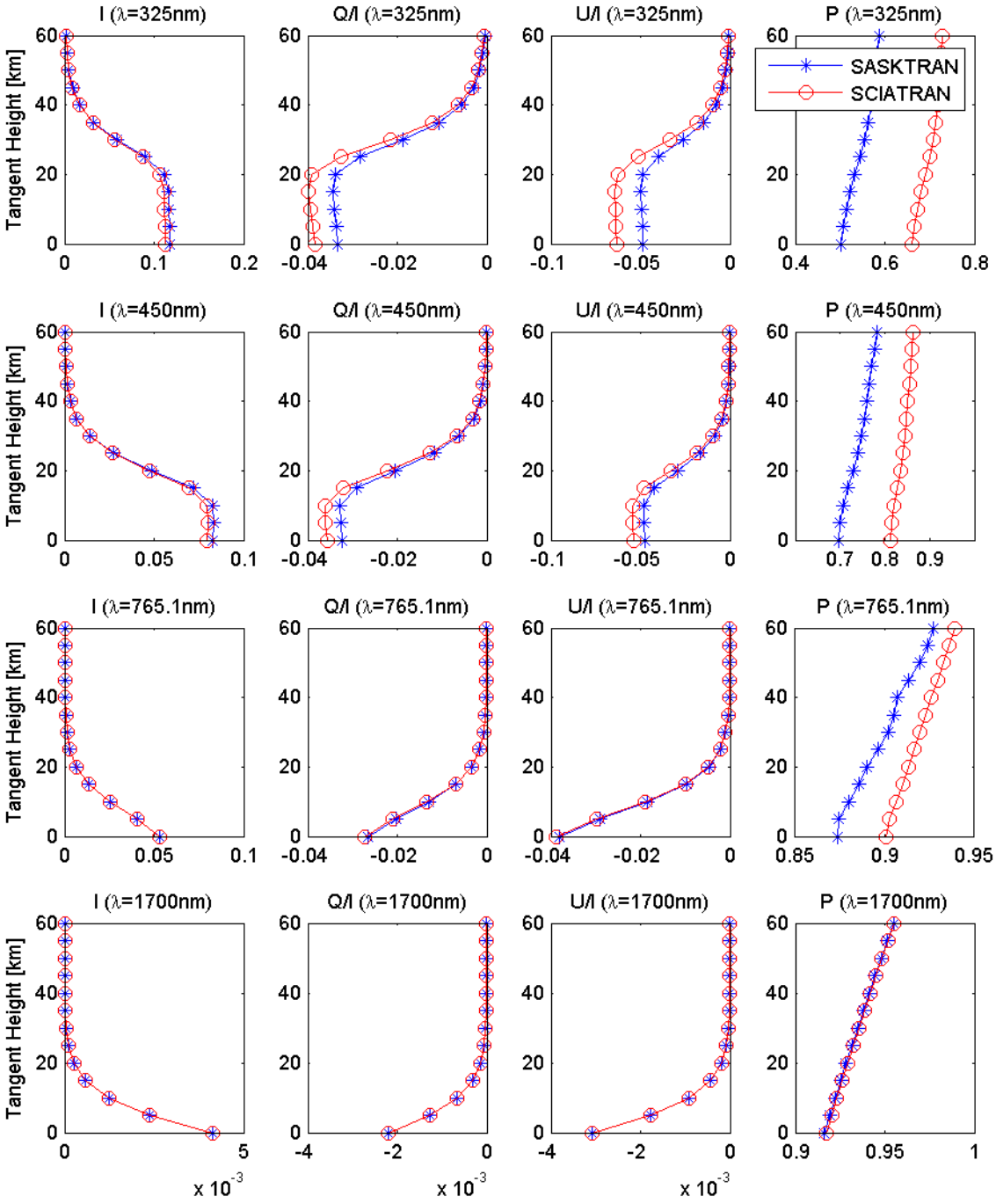

Figure B.7: The polarized multiple scatter radiative transfer results for $\varpi = 96.47°$ and $\varsigma = 26.84°$ at varying wavelengths

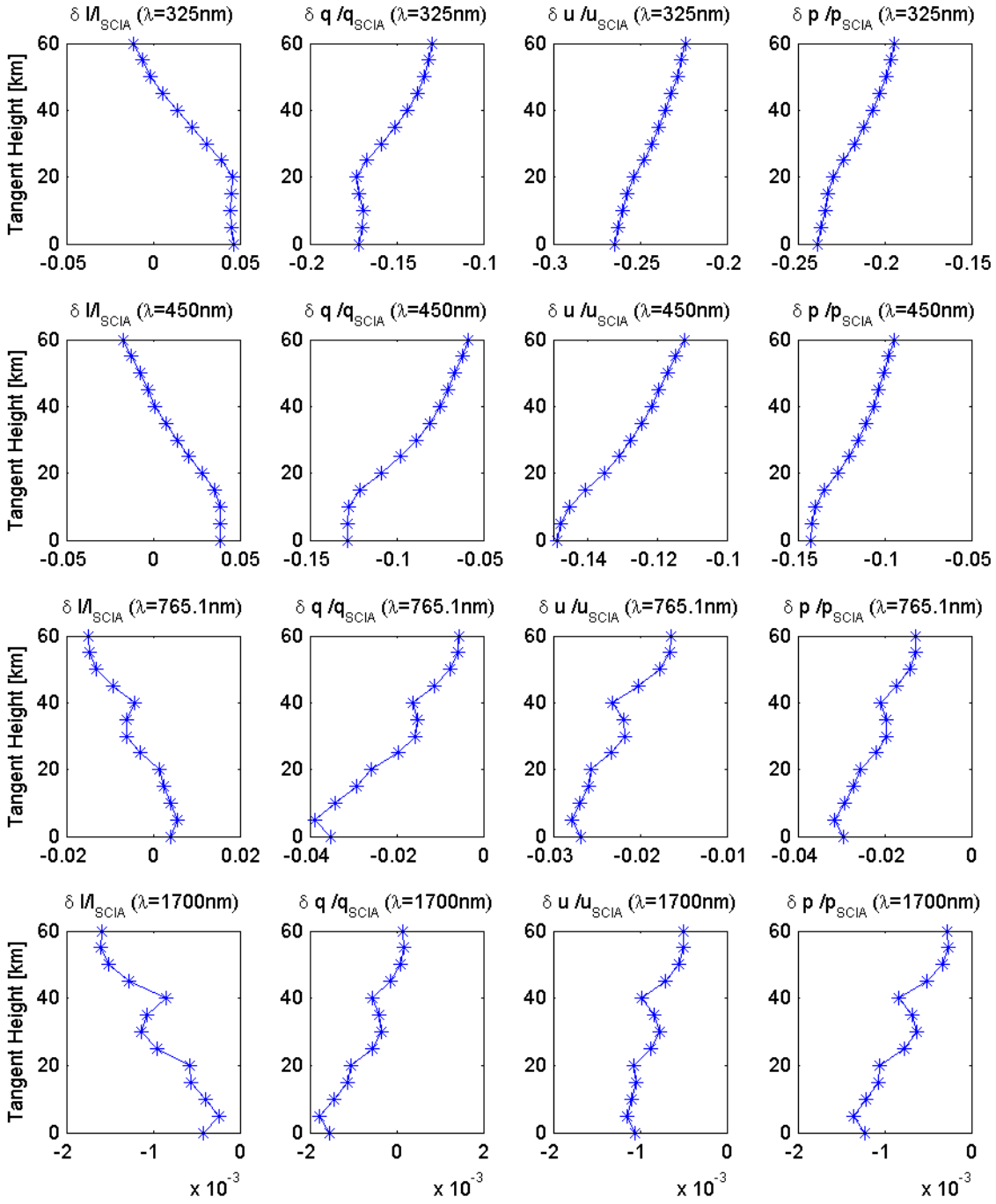

Figure B.8: The normalized difference in polarized multiple scatter radiative transfer results for $\varpi = 96.47°$ and $\varsigma = 26.84°$ at varying wavelengths

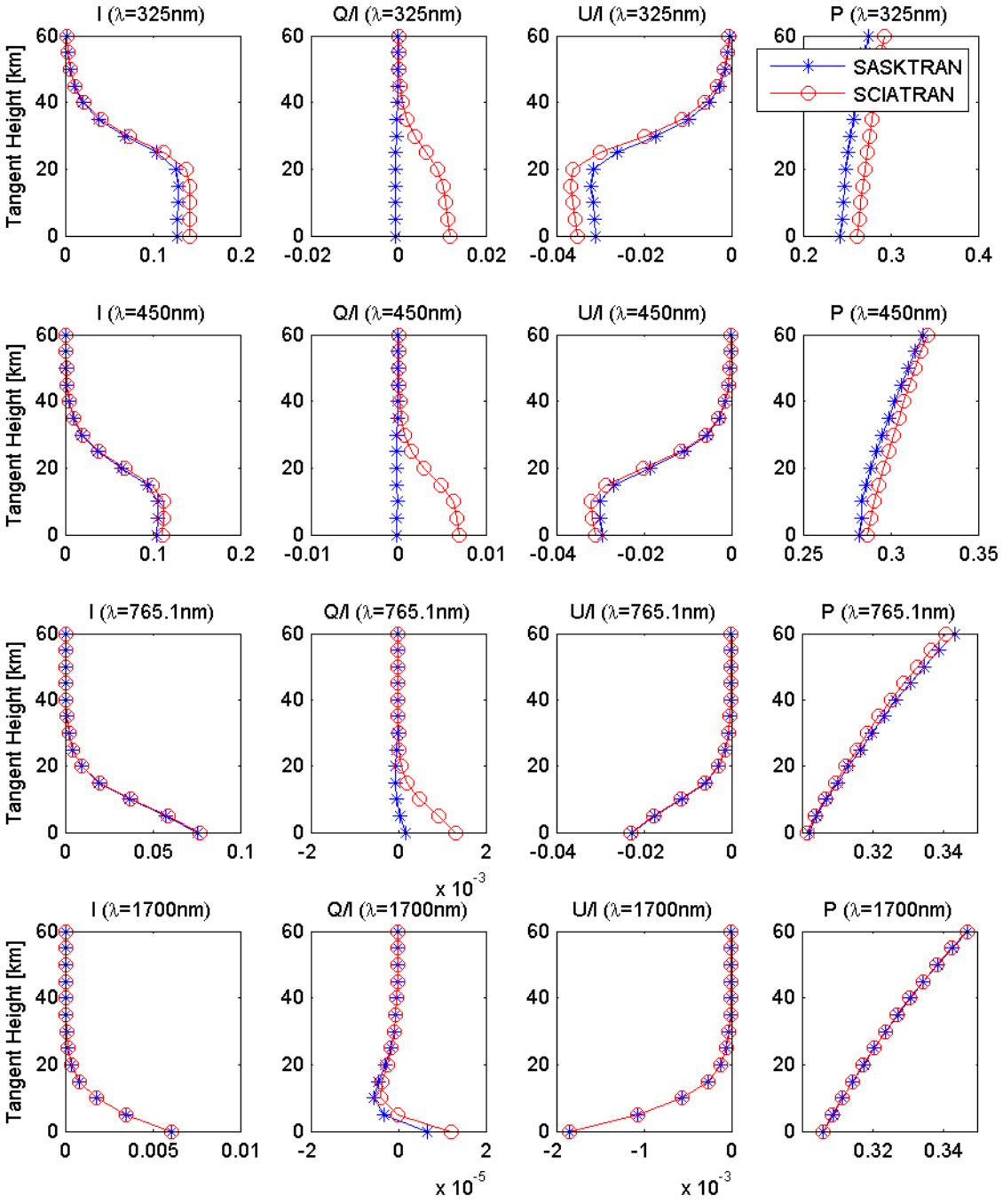

Figure B.9: The polarized multiple scatter radiative transfer results for $\varpi = 142.55°$ and $\varsigma = 52.88°$ at varying wavelengths

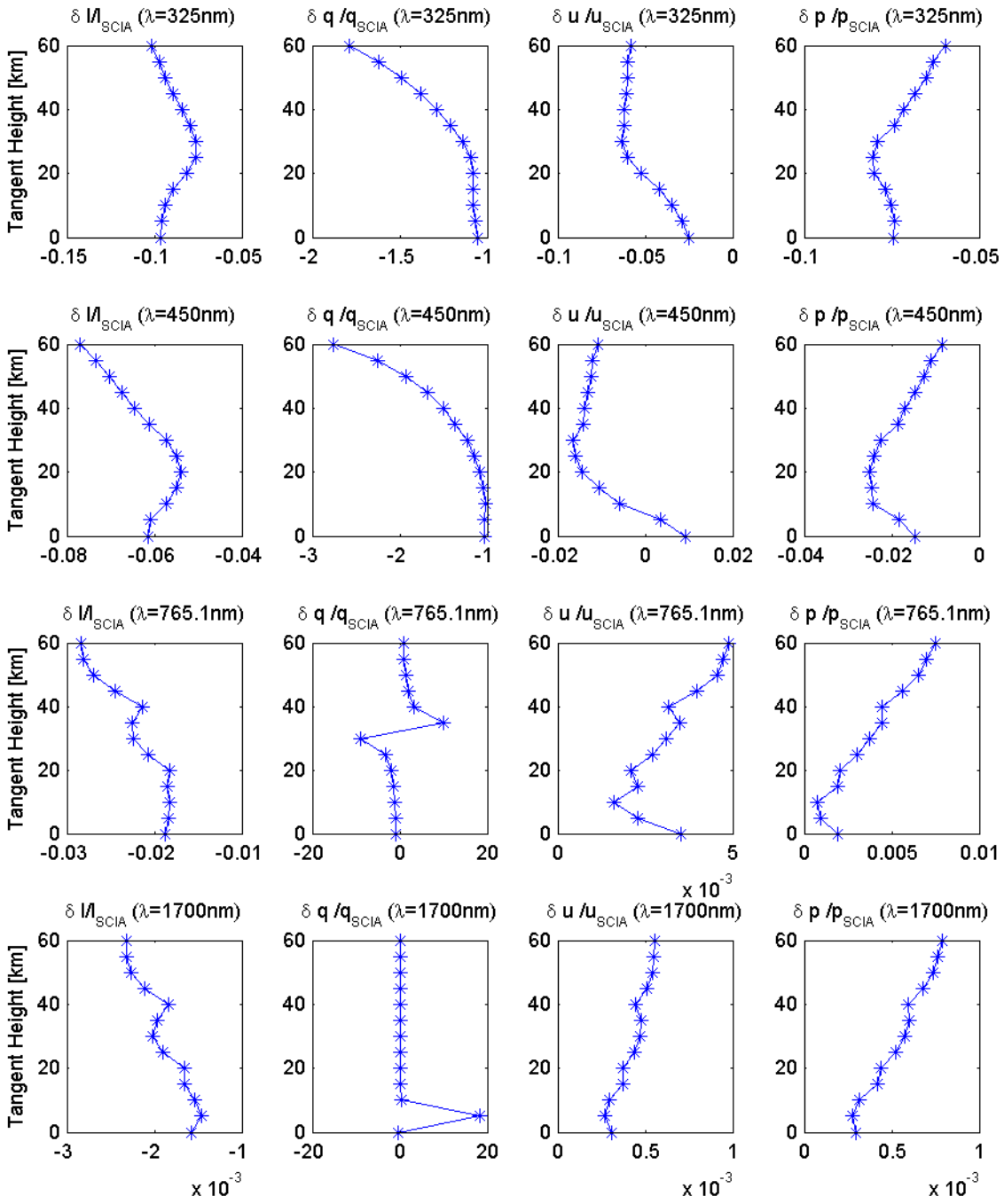

Figure B.10: The normalized difference in polarized multiple scatter radiative transfer results for $\varpi = 142.55°$ and $\varsigma = 52.88°$ at varying wavelengths

Appendix C

Atmospheric Parameters

The following atmospheric parameters were provided by by P. Leibing of the Institute of Environmental Physics, Institute of Remote Sensing at the University of Bremen - Department of Physics and Engineering. They define the composition of the atmosphere used in the comparisons between vector SCIATRAN and vector SASKTRAN that are discussed in Sections 4.2 and 4.3. The values were not used in SASKTRAN directly, but were used by Leibing to derive the scattering extinction values that are listed in Appendix D.

z	p	T	O_2	H_2O	CO_2	N_2O	CO	CH_4
km	mb	K	ppm	ppm	ppm	ppm	ppm	ppm
120.0	$2.538 \cdot 10^{-5}$	360.0	$7.250 \cdot 10^{4}$	0.2000	35.00	$1.851 \cdot 10^{-4}$	50.00	0.03000
115.0	$4.010 \cdot 10^{-5}$	300.0	$9.400 \cdot 10^{4}$	0.2400	40.00	$2.120 \cdot 10^{-4}$	41.48	0.06000
110.0	$7.104 \cdot 10^{-5}$	240.0	$1.200 \cdot 10^{5}$	0.2800	60.00	$2.443 \cdot 10^{-4}$	33.56	0.09500
105.0	$1.448 \cdot 10^{-4}$	208.8	$1.400 \cdot 10^{5}$	0.3400	110.0	$2.837 \cdot 10^{-4}$	24.67	0.1100
100.0	$3.201 \cdot 10^{-4}$	195.1	$1.600 \cdot 10^{5}$	0.4000	195.0	$3.323 \cdot 10^{-4}$	16.92	0.1200
95.0	$7.597 \cdot 10^{-4}$	188.4	$1.800 \cdot 10^{5}$	0.5400	270.0	$3.932 \cdot 10^{-4}$	10.13	0.1300
90.0	$1.836 \cdot 10^{-3}$	186.9	$1.900 \cdot 10^{5}$	0.8500	310.0	$4.708 \cdot 10^{-4}$	5.843	0.1400
85.0	$4.457 \cdot 10^{-3}$	188.9	$2.000 \cdot 10^{5}$	1.330	320.0	$5.716 \cdot 10^{-4}$	3.239	0.1500
80.0	$1.052 \cdot 10^{-2}$	198.6	$2.090 \cdot 10^{5}$	2.050	328.0	$7.056 \cdot 10^{-4}$	1.497	0.1500
75.0	$2.388 \cdot 10^{-2}$	208.4	$2.090 \cdot 10^{5}$	2.825	330.0	$8.890 \cdot 10^{-4}$	0.6375	0.1500
70.0	$5.221 \cdot 10^{-2}$	219.6	$2.090 \cdot 10^{5}$	3.500	330.0	$1.149 \cdot 10^{-3}$	0.3059	0.1500
65.0	$1.093 \cdot 10^{-1}$	233.3	$2.090 \cdot 10^{5}$	4.200	330.0	$1.507 \cdot 10^{-3}$	0.1862	0.1500
60.0	$2.196 \cdot 10^{-1}$	247.0	$2.090 \cdot 10^{5}$	4.750	330.0	$2.065 \cdot 10^{-3}$	0.1073	0.1500
55.0	$4.252 \cdot 10^{-1}$	260.8	$2.090 \cdot 10^{5}$	5.100	330.0	$3.000 \cdot 10^{-3}$	0.06639	0.1650
50.0	$7.978 \cdot 10^{-1}$	270.6	$2.090 \cdot 10^{5}$	5.225	330.0	$4.752 \cdot 10^{-3}$	0.04597	0.2100

Table continued on next page

Table continued from previous page

z	p	T	O_2	H_2O	CO_2	N_2O	CO	CH_4
km	mb	K	ppm	ppm	ppm	ppm	ppm	ppm
47.5	1.089	270.6	$2.090 \cdot 10^5$	5.250	330.0	$9.378 \cdot 10^{-3}$	0.03717	0.2773
45.0	1.491	264.2	$2.090 \cdot 10^5$	5.225	330.0	$1.591 \cdot 10^{-2}$	0.03241	0.3631
42.5	2.060	257.3	$2.090 \cdot 10^5$	5.150	330.0	$2.751 \cdot 10^{-2}$	0.02824	0.4614
40.0	2.871	250.4	$2.090 \cdot 10^5$	5.025	330.0	$4.513 \cdot 10^{-2}$	0.02497	0.5638
37.5	4.041	243.4	$2.090 \cdot 10^5$	4.950	330.0	$6.693 \cdot 10^{-2}$	0.02220	0.6618
35.0	5.746	236.5	$2.090 \cdot 10^5$	4.900	330.0	$9.275 \cdot 10^{-2}$	0.02009	0.7460
32.5	8.258	229.6	$2.090 \cdot 10^5$	4.825	330.0	$1.165 \cdot 10^{-1}$	0.01850	0.8300
30.0	$1.197 \cdot 10^1$	226.5	$2.090 \cdot 10^5$	4.725	330.0	$1.416 \cdot 10^{-1}$	0.01710	0.9136
27.5	$1.743 \cdot 10^1$	224.0	$2.090 \cdot 10^5$	4.575	330.0	$1.588 \cdot 10^{-1}$	0.01598	0.9870
25.0	$2.549 \cdot 10^1$	221.6	$2.090 \cdot 10^5$	4.425	330.0	$1.756 \cdot 10^{-1}$	0.01498	1.055
24.0	$2.972 \cdot 10^1$	220.6	$2.090 \cdot 10^5$	4.300	330.0	$1.875 \cdot 10^{-1}$	0.01400	1.118
23.0	$3.467 \cdot 10^1$	219.6	$2.090 \cdot 10^5$	4.200	330.0	$1.967 \cdot 10^{-1}$	0.01307	1.191
22.0	$4.047 \cdot 10^1$	218.6	$2.090 \cdot 10^5$	4.065	330.0	$2.051 \cdot 10^{-1}$	0.01232	1.272
21.0	$4.729 \cdot 10^1$	217.6	$2.090 \cdot 10^5$	3.975	330.0	$2.194 \cdot 10^{-1}$	0.01232	1.355
20.0	$5.529 \cdot 10^1$	216.6	$2.090 \cdot 10^5$	3.900	330.0	$2.365 \cdot 10^{-1}$	0.01331	1.424
19.0	$6.467 \cdot 10^1$	216.6	$2.090 \cdot 10^5$	3.850	330.0	$2.527 \cdot 10^{-1}$	0.01549	1.480
18.0	$7.565 \cdot 10^1$	216.6	$2.090 \cdot 10^5$	3.825	330.0	$2.671 \cdot 10^{-1}$	0.01966	1.521
17.0	$8.850 \cdot 10^1$	216.6	$2.090 \cdot 10^5$	3.850	330.0	$2.783 \cdot 10^{-1}$	0.02489	1.553
16.0	$1.035 \cdot 10^2$	216.6	$2.090 \cdot 10^5$	3.950	330.0	$2.877 \cdot 10^{-1}$	0.03069	1.582
15.0	$1.211 \cdot 10^2$	216.6	$2.090 \cdot 10^5$	5.000	330.0	$2.944 \cdot 10^{-1}$	0.03941	1.605
14.0	$1.417 \cdot 10^2$	216.6	$2.090 \cdot 10^5$	5.927	330.0	$2.999 \cdot 10^{-1}$	0.05025	1.626
13.0	$1.658 \cdot 10^2$	216.6	$2.090 \cdot 10^5$	10.85	330.0	$3.048 \cdot 10^{-1}$	0.06374	1.645
12.0	$1.940 \cdot 10^2$	216.6	$2.090 \cdot 10^5$	19.06	330.0	$3.095 \cdot 10^{-1}$	0.07814	1.662
11.0	$2.270 \cdot 10^2$	216.8	$2.090 \cdot 10^5$	36.13	330.0	$3.140 \cdot 10^{-1}$	0.08964	1.675
10.0	$2.650 \cdot 10^2$	223.3	$2.090 \cdot 10^5$	69.96	330.0	$3.179 \cdot 10^{-1}$	0.09962	1.685
9.0	$3.080 \cdot 10^2$	229.7	$2.090 \cdot 10^5$	158.3	330.0	$3.195 \cdot 10^{-1}$	0.1094	1.693
8.0	$3.565 \cdot 10^2$	236.2	$2.090 \cdot 10^5$	366.7	330.0	$3.200 \cdot 10^{-1}$	0.1185	1.697
7.0	$4.110 \cdot 10^2$	242.7	$2.090 \cdot 10^5$	572.0	330.0	$3.200 \cdot 10^{-1}$	0.1247	1.699
6.0	$4.722 \cdot 10^2$	249.2	$2.090 \cdot 10^5$	925.4	330.0	$3.200 \cdot 10^{-1}$	0.1288	1.700
5.0	$5.405 \cdot 10^2$	255.7	$2.090 \cdot 10^5$	1397	330.0	$3.200 \cdot 10^{-1}$	0.1303	1.700
4.0	$6.166 \cdot 10^2$	262.2	$2.090 \cdot 10^5$	2158	330.0	$3.200 \cdot 10^{-1}$	0.1312	1.700
3.0	$7.012 \cdot 10^2$	268.7	$2.090 \cdot 10^5$	3182	330.0	$3.200 \cdot 10^{-1}$	0.1349	1.700
2.0	$7.950 \cdot 10^2$	275.2	$2.090 \cdot 10^5$	4631	330.0	$3.200 \cdot 10^{-1}$	0.1399	1.700
1.0	$8.988 \cdot 10^2$	281.7	$2.090 \cdot 10^5$	6071	330.0	$3.200 \cdot 10^{-1}$	0.1450	1.700
0.0	$1.013 \cdot 10^3$	288.1	$2.090 \cdot 10^5$	7745	330.0	$3.200 \cdot 10^{-1}$	0.1500	1.700

Appendix D

Precalculated Scattering Extinctions

The following scattering extinction values were calculated by P. Leibing of the Institute of Environmental Physics, Institute of Remote Sensing at the University of Bremen - Department of Physics and Engineering. They were used to compare the vector SCIATRAN and vector SASKTRAN in Sections 4.2 and 4.3. These extinction values are based on the atmospheric parameters provided in Appendix C that define the composition of the atmosphere for the comparisons.

Altitude km	Scattering Extinction χ_{scatt} (km^{-1})			
	$\lambda = 325$nm	$\lambda = 450$nm	$\lambda = 765.1$nm	$\lambda = 1700$nm
100.00000	$4.520 \cdot 10^{-8}$	$1.163 \cdot 10^{-8}$	$1.340 \cdot 10^{-9}$	$5.412 \cdot 10^{-11}$
99.00000	$5.410 \cdot 10^{-8}$	$1.392 \cdot 10^{-8}$	$1.604 \cdot 10^{-9}$	$6.478 \cdot 10^{-11}$
98.00000	$6.475 \cdot 10^{-8}$	$1.666 \cdot 10^{-8}$	$1.919 \cdot 10^{-9}$	$7.754 \cdot 10^{-11}$
97.00000	$7.751 \cdot 10^{-8}$	$1.994 \cdot 10^{-8}$	$2.298 \cdot 10^{-9}$	$9.281 \cdot 10^{-11}$
96.00000	$9.279 \cdot 10^{-8}$	$2.387 \cdot 10^{-8}$	$2.750 \cdot 10^{-9}$	$1.111 \cdot 10^{-10}$
95.00000	$1.111 \cdot 10^{-7}$	$2.858 \cdot 10^{-8}$	$3.293 \cdot 10^{-9}$	$1.330 \cdot 10^{-10}$
94.00000	$1.327 \cdot 10^{-7}$	$3.415 \cdot 10^{-8}$	$3.935 \cdot 10^{-9}$	$1.589 \cdot 10^{-10}$
93.00000	$1.586 \cdot 10^{-7}$	$4.080 \cdot 10^{-8}$	$4.701 \cdot 10^{-9}$	$1.899 \cdot 10^{-10}$
92.00000	$1.895 \cdot 10^{-7}$	$4.876 \cdot 10^{-8}$	$5.618 \cdot 10^{-9}$	$2.269 \cdot 10^{-10}$
91.00000	$2.265 \cdot 10^{-7}$	$5.826 \cdot 10^{-8}$	$6.713 \cdot 10^{-9}$	$2.712 \cdot 10^{-10}$
90.00000	$2.706 \cdot 10^{-7}$	$6.962 \cdot 10^{-8}$	$8.022 \cdot 10^{-9}$	$3.240 \cdot 10^{-10}$
89.00000	$3.224 \cdot 10^{-7}$	$8.295 \cdot 10^{-8}$	$9.558 \cdot 10^{-9}$	$3.861 \cdot 10^{-10}$
88.00000	$3.842 \cdot 10^{-7}$	$9.884 \cdot 10^{-8}$	$1.139 \cdot 10^{-8}$	$4.600 \cdot 10^{-10}$
87.00000	$4.578 \cdot 10^{-7}$	$1.178 \cdot 10^{-7}$	$1.357 \cdot 10^{-8}$	$5.482 \cdot 10^{-10}$

Table continued on next page

Table continued from previous page

Altitude km	Scattering Extinction $\chi_{\text{scatt}}\ km^{-1}$			
	$\lambda = 325$nm	$\lambda = 450$nm	$\lambda = 765.1$nm	$\lambda = 1700$nm
86.00000	$5.455 \cdot 10^{-7}$	$1.403 \cdot 10^{-7}$	$1.617 \cdot 10^{-8}$	$6.532 \cdot 10^{-10}$
85.00000	$6.500 \cdot 10^{-7}$	$1.672 \cdot 10^{-7}$	$1.927 \cdot 10^{-8}$	$7.783 \cdot 10^{-10}$
84.00000	$7.639 \cdot 10^{-7}$	$1.965 \cdot 10^{-7}$	$2.264 \cdot 10^{-8}$	$9.147 \cdot 10^{-10}$
83.00000	$8.979 \cdot 10^{-7}$	$2.310 \cdot 10^{-7}$	$2.662 \cdot 10^{-8}$	$1.075 \cdot 10^{-9}$
82.00000	$1.056 \cdot 10^{-6}$	$2.716 \cdot 10^{-7}$	$3.129 \cdot 10^{-8}$	$1.264 \cdot 10^{-9}$
81.00000	$1.241 \cdot 10^{-6}$	$3.193 \cdot 10^{-7}$	$3.679 \cdot 10^{-8}$	$1.486 \cdot 10^{-9}$
80.00000	$1.459 \cdot 10^{-6}$	$3.754 \cdot 10^{-7}$	$4.325 \cdot 10^{-8}$	$1.747 \cdot 10^{-9}$
79.00000	$1.702 \cdot 10^{-6}$	$4.380 \cdot 10^{-7}$	$5.046 \cdot 10^{-8}$	$2.038 \cdot 10^{-9}$
78.00000	$1.986 \cdot 10^{-6}$	$5.110 \cdot 10^{-7}$	$5.888 \cdot 10^{-8}$	$2.378 \cdot 10^{-9}$
77.00000	$2.318 \cdot 10^{-6}$	$5.963 \cdot 10^{-7}$	$6.870 \cdot 10^{-8}$	$2.775 \cdot 10^{-9}$
76.00000	$2.705 \cdot 10^{-6}$	$6.958 \cdot 10^{-7}$	$8.017 \cdot 10^{-8}$	$3.239 \cdot 10^{-9}$
75.00000	$3.157 \cdot 10^{-6}$	$8.121 \cdot 10^{-7}$	$9.357 \cdot 10^{-8}$	$3.780 \cdot 10^{-9}$
74.00000	$3.652 \cdot 10^{-6}$	$9.395 \cdot 10^{-7}$	$1.083 \cdot 10^{-7}$	$4.373 \cdot 10^{-9}$
73.00000	$4.225 \cdot 10^{-6}$	$1.087 \cdot 10^{-6}$	$1.253 \cdot 10^{-7}$	$5.060 \cdot 10^{-9}$
72.00000	$4.889 \cdot 10^{-6}$	$1.258 \cdot 10^{-6}$	$1.449 \cdot 10^{-7}$	$5.855 \cdot 10^{-9}$
71.00000	$5.658 \cdot 10^{-6}$	$1.456 \cdot 10^{-6}$	$1.677 \cdot 10^{-7}$	$6.776 \cdot 10^{-9}$
70.00000	$6.549 \cdot 10^{-6}$	$1.685 \cdot 10^{-6}$	$1.941 \cdot 10^{-7}$	$7.842 \cdot 10^{-9}$
69.00000	$7.499 \cdot 10^{-6}$	$1.929 \cdot 10^{-6}$	$2.223 \cdot 10^{-7}$	$8.979 \cdot 10^{-9}$
68.00000	$8.587 \cdot 10^{-6}$	$2.209 \cdot 10^{-6}$	$2.545 \cdot 10^{-7}$	$1.028 \cdot 10^{-8}$
67.00000	$9.835 \cdot 10^{-6}$	$2.530 \cdot 10^{-6}$	$2.915 \cdot 10^{-7}$	$1.178 \cdot 10^{-8}$
66.00000	$1.127 \cdot 10^{-5}$	$2.898 \cdot 10^{-6}$	$3.339 \cdot 10^{-7}$	$1.349 \cdot 10^{-8}$
65.00000	$1.291 \cdot 10^{-5}$	$3.320 \cdot 10^{-6}$	$3.826 \cdot 10^{-7}$	$1.545 \cdot 10^{-8}$
64.00000	$1.467 \cdot 10^{-5}$	$3.773 \cdot 10^{-6}$	$4.347 \cdot 10^{-7}$	$1.756 \cdot 10^{-8}$
63.00000	$1.667 \cdot 10^{-5}$	$4.288 \cdot 10^{-6}$	$4.941 \cdot 10^{-7}$	$1.996 \cdot 10^{-8}$
62.00000	$1.895 \cdot 10^{-5}$	$4.875 \cdot 10^{-6}$	$5.617 \cdot 10^{-7}$	$2.269 \cdot 10^{-8}$
61.00000	$2.154 \cdot 10^{-5}$	$5.542 \cdot 10^{-6}$	$6.385 \cdot 10^{-7}$	$2.579 \cdot 10^{-8}$
60.00000	$2.449 \cdot 10^{-5}$	$6.301 \cdot 10^{-6}$	$7.260 \cdot 10^{-7}$	$2.933 \cdot 10^{-8}$
59.00000	$2.764 \cdot 10^{-5}$	$7.112 \cdot 10^{-6}$	$8.194 \cdot 10^{-7}$	$3.310 \cdot 10^{-8}$
58.00000	$3.120 \cdot 10^{-5}$	$8.028 \cdot 10^{-6}$	$9.249 \cdot 10^{-7}$	$3.736 \cdot 10^{-8}$
57.00000	$3.523 \cdot 10^{-5}$	$9.063 \cdot 10^{-6}$	$1.044 \cdot 10^{-6}$	$4.218 \cdot 10^{-8}$
56.00000	$3.977 \cdot 10^{-5}$	$1.023 \cdot 10^{-5}$	$1.179 \cdot 10^{-6}$	$4.763 \cdot 10^{-8}$
55.00000	$4.491 \cdot 10^{-5}$	$1.155 \cdot 10^{-5}$	$1.331 \cdot 10^{-6}$	$5.378 \cdot 10^{-8}$
54.00000	$5.056 \cdot 10^{-5}$	$1.301 \cdot 10^{-5}$	$1.499 \cdot 10^{-6}$	$6.054 \cdot 10^{-8}$
53.00000	$5.691 \cdot 10^{-5}$	$1.464 \cdot 10^{-5}$	$1.687 \cdot 10^{-6}$	$6.815 \cdot 10^{-8}$
52.00000	$6.407 \cdot 10^{-5}$	$1.648 \cdot 10^{-5}$	$1.899 \cdot 10^{-6}$	$7.672 \cdot 10^{-8}$
51.00000	$7.213 \cdot 10^{-5}$	$1.856 \cdot 10^{-5}$	$2.138 \cdot 10^{-6}$	$8.638 \cdot 10^{-8}$
50.00000	$8.122 \cdot 10^{-5}$	$2.089 \cdot 10^{-5}$	$2.407 \cdot 10^{-6}$	$9.725 \cdot 10^{-8}$
49.00000	$9.198 \cdot 10^{-5}$	$2.366 \cdot 10^{-5}$	$2.727 \cdot 10^{-6}$	$1.101 \cdot 10^{-7}$
48.00000	$1.042 \cdot 10^{-4}$	$2.680 \cdot 10^{-5}$	$3.088 \cdot 10^{-6}$	$1.247 \cdot 10^{-7}$
47.00000	$1.186 \cdot 10^{-4}$	$3.052 \cdot 10^{-5}$	$3.516 \cdot 10^{-6}$	$1.420 \cdot 10^{-7}$
46.00000	$1.358 \cdot 10^{-4}$	$3.493 \cdot 10^{-5}$	$4.025 \cdot 10^{-6}$	$1.626 \cdot 10^{-7}$
45.00000	$1.555 \cdot 10^{-4}$	$4.000 \cdot 10^{-5}$	$4.608 \cdot 10^{-6}$	$1.862 \cdot 10^{-7}$
44.00000	$1.788 \cdot 10^{-4}$	$4.600 \cdot 10^{-5}$	$5.300 \cdot 10^{-6}$	$2.141 \cdot 10^{-7}$

Table continued on next page

Table continued from previous page

Altitude km	Scattering Extinction $\chi_{\text{scatt}}\ km^{-1}$			
	$\lambda = 325$nm	$\lambda = 450$nm	$\lambda = 765.1$nm	$\lambda = 1700$nm
43.00000	$2.056 \cdot 10^{-4}$	$5.290 \cdot 10^{-5}$	$6.096 \cdot 10^{-6}$	$2.462 \cdot 10^{-7}$
42.00000	$2.370 \cdot 10^{-4}$	$6.096 \cdot 10^{-5}$	$7.024 \cdot 10^{-6}$	$2.837 \cdot 10^{-7}$
41.00000	$2.736 \cdot 10^{-4}$	$7.038 \cdot 10^{-5}$	$8.109 \cdot 10^{-6}$	$3.276 \cdot 10^{-7}$
40.00000	$3.158 \cdot 10^{-4}$	$8.126 \cdot 10^{-5}$	$9.363 \cdot 10^{-6}$	$3.782 \cdot 10^{-7}$
39.00000	$3.662 \cdot 10^{-4}$	$9.422 \cdot 10^{-5}$	$1.086 \cdot 10^{-5}$	$4.385 \cdot 10^{-7}$
38.00000	$4.247 \cdot 10^{-4}$	$1.093 \cdot 10^{-4}$	$1.259 \cdot 10^{-5}$	$5.085 \cdot 10^{-7}$
37.00000	$4.935 \cdot 10^{-4}$	$1.270 \cdot 10^{-4}$	$1.463 \cdot 10^{-5}$	$5.909 \cdot 10^{-7}$
36.00000	$5.747 \cdot 10^{-4}$	$1.478 \cdot 10^{-4}$	$1.703 \cdot 10^{-5}$	$6.881 \cdot 10^{-7}$
35.00000	$6.693 \cdot 10^{-4}$	$1.722 \cdot 10^{-4}$	$1.984 \cdot 10^{-5}$	$8.014 \cdot 10^{-7}$
34.00000	$7.829 \cdot 10^{-4}$	$2.014 \cdot 10^{-4}$	$2.321 \cdot 10^{-5}$	$9.375 \cdot 10^{-7}$
33.00000	$9.159 \cdot 10^{-4}$	$2.357 \cdot 10^{-4}$	$2.715 \cdot 10^{-5}$	$1.097 \cdot 10^{-6}$
32.00000	$1.070 \cdot 10^{-3}$	$2.753 \cdot 10^{-4}$	$3.172 \cdot 10^{-5}$	$1.281 \cdot 10^{-6}$
31.00000	$1.248 \cdot 10^{-3}$	$3.211 \cdot 10^{-4}$	$3.700 \cdot 10^{-5}$	$1.494 \cdot 10^{-6}$
30.00000	$1.456 \cdot 10^{-3}$	$3.745 \cdot 10^{-4}$	$4.315 \cdot 10^{-5}$	$1.743 \cdot 10^{-6}$
29.00000	$1.699 \cdot 10^{-3}$	$4.372 \cdot 10^{-4}$	$5.038 \cdot 10^{-5}$	$2.035 \cdot 10^{-6}$
28.00000	$1.984 \cdot 10^{-3}$	$5.104 \cdot 10^{-4}$	$5.881 \cdot 10^{-5}$	$2.376 \cdot 10^{-6}$
27.00000	$2.318 \cdot 10^{-3}$	$5.963 \cdot 10^{-4}$	$6.871 \cdot 10^{-5}$	$2.775 \cdot 10^{-6}$
26.00000	$2.710 \cdot 10^{-3}$	$6.972 \cdot 10^{-4}$	$8.033 \cdot 10^{-5}$	$3.245 \cdot 10^{-6}$
25.00000	$3.169 \cdot 10^{-3}$	$8.152 \cdot 10^{-4}$	$9.393 \cdot 10^{-5}$	$3.794 \cdot 10^{-6}$
24.00000	$3.711 \cdot 10^{-3}$	$9.548 \cdot 10^{-4}$	$1.100 \cdot 10^{-4}$	$4.444 \cdot 10^{-6}$
23.00000	$4.349 \cdot 10^{-3}$	$1.119 \cdot 10^{-3}$	$1.289 \cdot 10^{-4}$	$5.208 \cdot 10^{-6}$
22.00000	$5.100 \cdot 10^{-3}$	$1.312 \cdot 10^{-3}$	$1.512 \cdot 10^{-4}$	$6.107 \cdot 10^{-6}$
21.00000	$5.987 \cdot 10^{-3}$	$1.540 \cdot 10^{-3}$	$1.775 \cdot 10^{-4}$	$7.169 \cdot 10^{-6}$
20.00000	$7.032 \cdot 10^{-3}$	$1.809 \cdot 10^{-3}$	$2.084 \cdot 10^{-4}$	$8.420 \cdot 10^{-6}$
19.00000	$8.225 \cdot 10^{-3}$	$2.116 \cdot 10^{-3}$	$2.438 \cdot 10^{-4}$	$9.849 \cdot 10^{-6}$
18.00000	$9.621 \cdot 10^{-3}$	$2.475 \cdot 10^{-3}$	$2.852 \cdot 10^{-4}$	$1.152 \cdot 10^{-5}$
17.00000	$1.126 \cdot 10^{-2}$	$2.896 \cdot 10^{-3}$	$3.336 \cdot 10^{-4}$	$1.348 \cdot 10^{-5}$
16.00000	$1.316 \cdot 10^{-2}$	$3.387 \cdot 10^{-3}$	$3.902 \cdot 10^{-4}$	$1.576 \cdot 10^{-5}$
15.00000	$1.540 \cdot 10^{-2}$	$3.962 \cdot 10^{-3}$	$4.565 \cdot 10^{-4}$	$1.844 \cdot 10^{-5}$
14.00000	$1.802 \cdot 10^{-2}$	$4.636 \cdot 10^{-3}$	$5.342 \cdot 10^{-4}$	$2.158 \cdot 10^{-5}$
13.00000	$2.109 \cdot 10^{-2}$	$5.425 \cdot 10^{-3}$	$6.251 \cdot 10^{-4}$	$2.525 \cdot 10^{-5}$
12.00000	$2.467 \cdot 10^{-2}$	$6.348 \cdot 10^{-3}$	$7.314 \cdot 10^{-4}$	$2.954 \cdot 10^{-5}$
11.00000	$2.884 \cdot 10^{-2}$	$7.421 \cdot 10^{-3}$	$8.550 \cdot 10^{-4}$	$3.454 \cdot 10^{-5}$
10.000000	$3.269 \cdot 10^{-2}$	$8.411 \cdot 10^{-3}$	$9.691 \cdot 10^{-4}$	$3.915 \cdot 10^{-5}$
9.000000	$3.694 \cdot 10^{-2}$	$9.503 \cdot 10^{-3}$	$1.095 \cdot 10^{-3}$	$4.423 \cdot 10^{-5}$
8.000000	$4.158 \cdot 10^{-2}$	$1.070 \cdot 10^{-2}$	$1.232 \cdot 10^{-3}$	$4.979 \cdot 10^{-5}$
7.000000	$4.665 \cdot 10^{-2}$	$1.200 \cdot 10^{-2}$	$1.383 \cdot 10^{-3}$	$5.586 \cdot 10^{-5}$
6.000000	$5.220 \cdot 10^{-2}$	$1.343 \cdot 10^{-2}$	$1.547 \cdot 10^{-3}$	$6.250 \cdot 10^{-5}$
5.000000	$5.823 \cdot 10^{-2}$	$1.498 \cdot 10^{-2}$	$1.726 \cdot 10^{-3}$	$6.973 \cdot 10^{-5}$
4.000000	$6.478 \cdot 10^{-2}$	$1.667 \cdot 10^{-2}$	$1.920 \cdot 10^{-3}$	$7.757 \cdot 10^{-5}$
3.000000	$7.189 \cdot 10^{-2}$	$1.849 \cdot 10^{-2}$	$2.131 \cdot 10^{-3}$	$8.608 \cdot 10^{-5}$
2.000000	$7.958 \cdot 10^{-2}$	$2.047 \cdot 10^{-2}$	$2.359 \cdot 10^{-3}$	$9.529 \cdot 10^{-5}$
1.000000	$8.789 \cdot 10^{-2}$	$2.261 \cdot 10^{-2}$	$2.605 \cdot 10^{-3}$	$1.052 \cdot 10^{-4}$
0.000000	$9.686 \cdot 10^{-2}$	$2.492 \cdot 10^{-2}$	$2.871 \cdot 10^{-3}$	$1.160 \cdot 10^{-4}$

Bibliography

Altschuler, E. L., T. J. Williams, E. R. Ratner, R. Tipton, R. Stong, F. Dowla, and F. Wooten (1997), Possible global minimum lattice configurations for thomson's problem of charges on a sphere, *Physical Review Letters*, *78*, 2681–2685, doi:10.1103/PhysRevLett.78.2681.

Bauman, J. J., P. B. Russell, M. A. Geller, and P. Hamill (2003), A stratospheric aerosol climatology from SAGE II and CLAES measurements: 1. Methodology, *J. Geophys. Res.*, *108*, 6–10, doi:10.1029/2002JD002992.

Bingen, C., D. Fussen, and F. Vanhellemont (2004), A global climatology of stratospheric aerosol size distribution parameters derived from SAGE II data over the period 1984-2000: 1. Methodology and climatological observations, *J. Geophys. Res.*, *109*, 1–10, doi:10.1029/2003JD003518.

Bodhaine, B. A., N. B. Wood, E. G. Dutton, and J. R. Slusser (1999), On Rayleigh Optical Depth Calculations, *Journal of Atmospheric and Oceanic Technology*, *16*, 1854–+, doi:10.1175/1520-0426(1999)016⟨1854:ORODC⟩2.0.CO;2.

Bourassa, A. (2007), Stratospheric aerosol retrieval with OSIRIS limb scatter measurements, Ph.D. thesis, University of Saskatchewan.

Bourassa, A. E., D. A. Degenstein, R. L. Gattinger, and E. J. Llewellyn (2007), Stratospheric aerosol retrieval with OSIRIS limb scatter measurements, *J. Geophys. Res.*, *112*, 10,217–+, doi:10.1029/2006JD008079.

Bourassa, A. E., D. A. Degenstein, and E. J. Llewellyn (2008), SASKTRAN: A spherical geometry radiative transfer code for efficient estimation of limb scattered sunlight, *Journal of Quantitative Spectroscopy and Radiative Transfer*, *109*, 52–73, doi:10.1016/j.jqsrt.2007.07.007.

Chahine, M. T. (1970), Inverse problems in radiative transfer: Determination of atmospheric parameters, *J. Atmos. Sci.*, *27*, 960–967.

Chandrasekhar, S. (1960), *Radiative Transfer*, Dover, New York.

Collins, D. G., W. G. Blattner, M. B. Wells, and H. G. Horak (1972), Backward Monte Carlo calculations of the polarization characteristics of the radiation emerging from spherical-shell atmospheres, *Appl. Opt.*, *11*, 2684–2696.

Degenstein, D. A., E. J. Llewellyn, and N. D. Lloyd (2003), Volume emission rate tomography from a satellite platform, *Appl. Opt.*, *42*, 1441–1450.

Deshler, T., M. E. Hervig, D. J. Hofmann, J. M. Rosen, and J. B. Liley (2003), Thirty years of in-situ stratospheric aerosol size distribution measurements from Laramie, Wyoming (41 N), using balloon-borne instruments, *J. Geophys. Res.*, *108*, 1–13, doi:10.1029/2002JD002514.

Edlen, B. (1953), The dispersion of standard air, *Journal of the Optical Society of America (1917-1983)*, *43*, 339–+.

Fleagle, R. G., and J. A. Businger (1980), *An introduction to atmospheric physics.*, 2 ed., Academic Press, Inc.

Glaccum, W., R. L. Lucke, R. M. Bevilacqua, E. P. Shettle, J. S. Hornstein, D. T. Chen, J. D. Lumpe, S. S. Krigman, D. J. Debrestian, M. D. Fromm, F. Dalaudier, E. Chassefière, C. Deniel, C. E. Randall, D. W. Rusch, J. J. Olivero, C. Brogniez, J. Lenoble, and R. Kremer (1996), The Polar Ozone and Aerosol Measurement instrument, *J. Geophys. Res.*, *101*, 14,479–14,488, doi:10.1029/96JD00576.

Goody, R. M., and Y. L. Yung (1989), *Atmospheric radiation : theoretical basis*, 2 ed.

Granat, L., H. Rodhe, and R. Hallberg (1976), The global sulphur cycle, *Ecological Bulletins*, *22*, 89–134.

Griffiths, D. J. (1999), *Introduction to Electrodynamics*, 3 ed., Prentice Hall.

Gruner, P., and H. Kleinert (1927), Die dammerungerscheinen, *In iProblemeder Kosmischen Physik*, *10*, 1–113.

Hansen, J. E., and L. D. Travis (1974), Light scattering in planetary atmospheres, *Space Sci. Rev.*, *16*, 527–610.

Hedin, A. E. (1991), Extension of the MSIS thermosphere model into the middle and lower atmosphere, *Journal of Geophysical Research*, *96*, 1159–1172, doi:10.1029/90JA02125.

Hofmann, D., J. Barnes, M. O'Neill, M. Trudeau, and R. Neely (2009), Increase in background stratospheric aerosol observed with lidar at Mauna Loa Observatory and Boulder, Colorado, *Geophysical Research Letters*, *36*, 15,808–+, doi:10.1029/2009GL039008.

Jensen, E. J., O. B. Toon, D. L. Westphal, S. Kinne, and A. J. Heymsfield (1994), Microphysical modeling of cirrus 1. Comparison with 1986 FIRE IFO measurements, *Journal of Geophysical Research*, *99*, 10,421–10,442, doi:10.1029/93JD02334.

Junge, C. E., C. W. Chagnon, and J. E. Manson (1961), Stratospheric aerosols, *J. Atmos. Sci.*, *18*, 81–108.

Kuo, K., R. C. Weger, and R. M. Welch (1995), The picard iterative approximation to the solution of the integral equation of radiative transfer–Part 1. The plane–parallel case, *Journal of Quantitative Spectroscopy and Radiative Transfer*, *53*, 425–444, doi: 10.1016/0022-4073(95)90017-9.

Kuo, K., R. C. Weger, R. M. Welch, and S. K. Cox (1996), The Picard iterative approximation to the solution of the integral equation of radiative transfer. II. Three-dimensional geometry., *Journal of Quantitative Spectroscopy and Radiative Transfer*, *55*, 195–213, doi:10.1016/0022-4073(95)00152-2.

Lacis, A., J. Hansen, and M. Sato (1992), Climate forcing by stratospheric aerosols, *Geophys. Res. Lett.*, *19*, 1607–1610.

Lenoble, J. (1993), *Atmospheric radiative transfer*.

Lenoble, J., and Z. Sekera (1961), Equation of radiative transfer in a planetary spherical atmosphere, *Proc. Nat. Ac. Sci.*, *47*, 372–378.

Llewellyn, E. J., N. D. Lloyd, D. A. Degenstein, R. L. Gattinger, S. V. Petelina, A. E. Bourassa, J. T. Wiensz, E. V. Ivanov, I. C. McDade, B. H. Solheim, J. C. McConnell, C. S. Haley, C. von Savigny, C. E. Sioris, C. A. McLinden, E. Griffioen, J. Kaminski, W. F. Evans, E. Puckrin, K. Strong, V. Wehrle, R. H. Hum, D. J. W. Kendall, J. Matsushita, D. P. Murtagh, S. Brohede, J. Stegman, G. Witt, G. Barnes, W. F. Payne, L. Piché, K. Smith, G. Warshaw, D.-L. Deslauniers, P. Marchand, E. H. Richardson, R. A. King, I. Wevers, W. McCreath, E. Kyrölä, L. Oikarinen, G. W. Leppelmeier, H. Auvinen, G. Mégie, A. Hauchecorne, F. Lefèvre, J. de La Nöe, P. Ricaud, U. Frisk, F. Sjoberg, F. von Schéele, and L. Nordh (2004), The OSIRIS instrument on the Odin spacecraft, *Can. J. Phys.*, *82*(6), 411–422.

Lloyd, N. D., and E. J. Llewellyn (1989), Deconvolution of blurred images using photon counting statistics and maximum probability, *Can. J. Phys.*, *67*, 89+.

Lohmann, U., and J. Feichter (2005), Global indirect aerosol effects: a review, *Atmospheric Chemistry & Physics*, *5*, 715–737.

Lucke, R. L., D. R. Korwan, R. M. Bevilacqua, J. S. Hornstein, E. P. Shettle, D. T. Chen, M. Daehler, J. D. Lumpe, M. D. Fromm, D. Debrestian, B. Neff, M. Squire, G. König-Langlo, and J. Davies (1999), The Polar Ozone and Aerosol Measurement (POAM) III instrument and early validation results, *J. Geophys. Res.*, *104*, 18,785–18,800, doi:10.1029/1999JD900235.

McCormick, M. P., P. Hamill, T. J. Pepin, W. P. Chu, T. J. Swissler, and L. R. McMaster (1979), Satellite studies of the stratospheric aerosol., *Bull. Am. Meteorol. Soc.*, *60*, 1038–1047.

McLinden, C. A., J. C. McConnell, K. Strong, I. C. McDade, R. L. Gattinger, R. King, B. Solheim, E. J. Llewellyn, and W. J. F. Evans (2002), The impact of the OSIRIS grating efficiency on radiance and trace-gas retrievals, *Canadian Journal of Physics*, *80*, 469–+, doi:10.1139/p01-151.

McPeters, R. D., G. J. Labow, and J. A. Logan (2007), Ozone climatological profiles for satellite retrieval algorithms, *Journal of Geophysical Research (Atmospheres)*, *112*, 5308–+, doi:10.1029/2005JD006823.

Mishchenko, M. I., L. D. Travis, and A. A. Lacis (2002), *Scattering, Absorption, and Emission of Light by Small Particles*, Cambridge University Press.

Rosen, J. M. (1971), The boiling point of stratospheric aerosols, *J. Appl. Met.*, *10*, 1044–1045.

Rozanov, A., V. Rozanov, and J. P. Burrows (2001), A numerical radiative transfer model for a spherical planetary atmosphere: Combined differential-integral approach involving the Picard iterative approximation, *J. Quant. Spectrosc. Radiat. Trans.*, *69*, 491–512.

Rozanov, V. V., M. Buchwitz, K. Eichmann, R. de Beek, and J. P. Burrows (2002), Sciatran - a new radiative transfer model for geophysical applications in the 240-2400 NM spectral region: the pseudo-spherical version, *Advances in Space Research*, *29*, 1831–1835, doi:10.1016/S0273-1177(02)00095-9.

Russell, J. M., L. L. Gordley, J. H. Park, S. R. Drayson, W. D. Hesketh, R. J. Cicerone, A. F. Tuck, J. E. Frederick, J. E. Harries, and P. J. Crutzen (1993), The Halogen Occultation Experiment, *J. Geophys. Res.*, *98*, 10,777–10,797.

Russell, P. B., and M. P. McCormick (1989), SAGE II aerosol data validation and initial data use: An introduction and overview, *J. Geophys. Res.*, *94*, 8335–8338.

Sassen, K. (1997), Contrail-Cirrus and Their Potential for Regional Climate Change., *Bulletin of the American Meteorological Society*, *78*, 1885–1903, doi:10.1175/1520-0477(1997)078.

Shepard, D. (1968), A two-dimensional interpolation function for irregularly-spaced data, *Proceedings of the 1968 23rd ACM national conference*, pp. 517–524.

Sioris, C. E., C. D. Boone, P. F. Bernath, J. Zou, C. T. McElroy, and C. A. McLinden (2010), Atmospheric chemistry experiment (ace) observations of aerosol in the upper troposphere and lower stratosphere from the kasatochi volcanic eruption, *J. Geophys. Res.*, *115*, doi:10.1029/2009JD013469.

Solomon, S. (1999), Stratospheric ozone depletion: A review of concepts and history, *Rev. Geophys.*, *37*, 275–316, doi:10.1029/1999RG900008.

Starr, D. O. C., and S. K. Cox (1985), Cirrus clouds. i - a cirrus cloud model. ii - numerical experiments on the formation and maintenance of cirrus, *Journal of the Atmospheric Sciences*, pp. 2663–2694.

Symons, G. (Ed.) (1888), *The Eruption of Krakatoa and Subsequent Phenomena*, Harrison and Sons.

Thomason, L. W. (2006), Assessment of Stratospheric Aerosol Processes, *World Climate Research Program*, pp. 1–322.

Thomason, L. W., and G. Taha (2003), SAGE III aerosol extinction measurements: Initial results, *Geophys. Res. Lett.*, *30*, 33.

Twomey, S. (1975), Comparison of constrained linear inversion and an iterative nonlinear algorithm applied to the indirect estimate of particle size distributions, *J. Comput. Phys.*, *18*, 188–200.

Twomey, S. (1977), *Atmospheric Aerosols*, Elsevier Scientific Publishing Company.

van de Hulst, H. C. (1962), *Light scattering by small particles*, New York: John Wiley & Sons, Inc.

Vanhellemont, F., C. Tetard, A. Bourassa, M. Fromm, J. Dodion, D. Fussen, C. Brogniez, D. Degenstein, K. L. Gilbert, D. N. Turnbull, P. Bernath, C. Boone, and K. A. Walker (2008), Aerosol extinction profiles at 525 nm and 1020 nm derived from ACE imager data: comparisons with GOMOS, SAGE II, SAGE III, POAM III, and OSIRIS, *Atmos. Chem. Phys.*, *8*, 2027–2037.

Vestreng, V., G. Myhre, H. Fagerli, S. Reis, and L. Tarrasón (2007), Twenty-five years of continuous sulphur dioxide emission reduction in Europe, *Atmospheric Chemistry & Physics Discussions*, *7*, 5099–5143.

Wiscombe, W. J. (1980), Improved Mie scattering algorithms, *Appl. Opt.*, *19*, 1505–1509.

Wood, R. W. (1902), On a Remarkable Case of Uneven Distribution of Light in a Diffraction Grating Spectrum, *Proceedings of the Physical Society of London*, *18*, 269–275, doi:10.1088/1478-7814/18/1/325.